Vibration Reduction in Passively-Isolated Ultra-Precision Manufacturing Machines using Mode Coupling

by

Jihyun Lee

A dissertation submitted in partial fulfillment
of the requirements for the degree of
Doctor of Philosophy
(Mechanical Engineering)
in the University of Michigan
2016

Doctoral committee:

Assistant Professor Chinedum E. Okwudire, Chair
Professor Bogdan I. Epureanu
Associate Professor Jeffrey T. Scruggs
Professor A. Galip Ulsoy

To my parents and brother in South Korea who supported my Ph.D journey.

ACKNOWLEDGEMENTS

Completing my doctoral studies means the achievement of a significant goal of my life. This achievement was made possible through the support and encouragement of many wonderful individuals.

First and foremost, I would like to thank my advisor, Professor Chinedum Okwudire for his patience, instruction, and thoroughness in molding me into a researcher. His thorough guidance has kept me on track throughout the research since 2012. His intellectual support at various stages of this work has been valuable in enabling me to carry this work to completion. I also would like to thank my doctoral committee, Professors Galip Ulsoy, Bogdan Epureanu and Jeffrey Scruggs for their valuable feedback and guidance. I especially would like to thank Professor Ulsoy who, at the very early stages of this research, provided helpful insights about the concepts of curve veering and mode localization discussed in Chapters 2 and 3. Discussions with Professor Epureanu (and Professor Noel Perkins) about curve veering and mode localization, were also illuminating. Moreover, I would like to thank Professor Jeffrey Scruggs for his very valuable feedback and his assistance in performing the H_2/H_∞ optimization discussed in Chapter 4.

I would like to thank my colleagues at the Mechatronics and Sustainability Research Lab for their intellectual support and friendship. Particularly, I would like to thank Dr. Amirhossein Ghasemi for his assistance with some of the theoretical and experimental work reported in Chapters 3 and 4. He initiated the idea of using a linear time invariant (LTI) control structure for single-variable isolator placement, which I then generalized into a multivariable control theoretic framework in Chapter 4. I would like to thank Mr. Molong Duan for his very useful suggestions with regard to incorporating the effects of gravity into the control theoretic framework of Chapter 4. Thanks also to Mr. Deokkyun Yoon and Mr. Keval Ramani for their useful feedback on my research.

I would like to thank DTL Corporation (Mori Seiki) for providing their 5-axis ultra-precision milling machine (NN1000 DCG) for some of the simulations and experiments reported in this dissertation. Appreciation also goes to Jongsoo Kim and Chang-Ju Kim of DTL Corporation for their assistance with some of the early experiments on NN1000 DCG. I would also like to thank the National Science Foundation (NSF) for financially supporting this research.

Last but not least, I would like to thank my parents and brother for all their support throughout my Ph.D. journey. Their constant love, support and encouragement throughout my study helped me to stay on track. I would like to thank Ms. Juri Kim who has encouraged me to complete my Ph.D. Special thanks also go to Dr. Andy Madden, Mr. Jason Rodgers, Dr. Ayoung Kim and Dr. Hungjung Won and all my friends for their companionship and encouragement during my stay in Ann Arbor, and for making my Ph.D. more than just an academic experience.

PREFACE

This doctoral dissertation consists of five chapters. The first chapter introduces the reader to the background, motivation, objectives and contributions of this dissertation research that covers three key subjects. The following three chapters (i.e., Chapters 2, 3 and 4) are self-contained discussions of the three subjects, and can be read independently. Chapters 2 and 3 are based on articles [1] and [2], which have been published in the Precision Engineering journal in 2013 and 2016, respectively. Chapter 4 is based on a manuscript that has recently been submitted and is under review in the Journal of Vibration and Acoustics [3]. Chapter 5 summarizes the conclusions and future work emanating from this dissertation research.

TABLE OF CONTENTS

LIST OF FIGURES

LIST OF TABLES

ABSTRACT

Vibration Reduction in Passively-Isolated Ultra-Precision Manufacturing Machines using Mode Coupling

by

Jihyun Lee

Chair: Chinedum E. Okwudire

Ultra-precision manufacturing (UPM) machines are designed to fabricate and measure complex parts having micrometer-level features and nanometer-level tolerances/surface finishes. Therefore, they must be isolated from deleterious effects of vibration to enable them to meet stringent precision requirements. UPM machine builders often prefer passive isolators for reducing vibration because they are easy to use, cost effective, energy neutral and reliable. A long-standing rule-of-thumb in passive isolation system design, recommended in academic literature and industrial practice, is to decouple all the vibration modes of an isolated machine by aligning the isolator mounting locations with the center of gravity (CG) of the machine. However, there is anecdotal evidence scattered in the literature that suggests that locating isolators such that vibration modes are coupled could help reduce vibrations of passively-isolated machines. What is lacking, however, is a proper understanding of when and how to use mode coupling to achieve superior vibration reduction.

This doctoral dissertation research seeks to provide a theoretical foundation as well as analysis-based design guidelines and tools for reducing unwanted vibration in passively-isolated UPM machines using mode coupling. Its primary contributions are threefold. Firstly, it uses eigenvalue and perturbation analyses on a single-variable, proportionally (or modally) damped, planar isolation system to demonstrate that the drastic reduction of vibration caused by mode

coupling is primarily linked to so-called “critical configurations” induced by curve veering and mode localization. It therefore clears the misconception purported in academic literature and industrial practice that the vibration-reduction effects of mode coupling on UPM machines are simply linked to damping. Secondly, it proves analytically that mode coupling (with or without damping effects included, and provided that it is properly carried out) is almost always better than the recommended practice of modal decoupling with regard to vibration reduction in passively-isolated UPM machines. The dissertation therefore provides design guidelines for properly exploiting weak mode coupling for vibration reduction in UPM machines. Thirdly, it proposes a framework for reformulating the generalized (multivariable, 3-D) UPM isolator placement problem as a linear feedback controller design problem whose gains represent isolator locations. It thus provides a powerful engineering tool for using linear control theory, in all its wealth and elegance, for the optimization and analyses of passive isolator placement.

The theoretical work presented in this dissertation is backed up by simulations and experiments conducted on prototypes of UPM machines. The results demonstrate that, when properly exploited, mode coupling could bring about huge reductions in UPM machine vibration compared to modal decoupling; for example, up to 40% reduction in residual vibration and 50% reduction in transmissibility are demonstrated experimentally in Chapter 3. Even though this dissertation is presented in the context of UPM machines, the reader will discover that its methods and findings are applicable to the placement of passive isolators/suspensions/dampers in automotive, aerospace, civil, and other applications.

CHAPTER 1
INTRODUCTION

1.1. Overview

Vibration isolation from exogenous disturbances is critical in many different applications, e.g., automotive [4-6], aerospace [7-9], building construction [10-12] and precision manufacturing [13-15]. This doctoral dissertation focuses on reducing vibration in ultra-precision manufacturing (UPM) machines equipped with passive vibration isolators. Section 1.2 describes UPM machines, as used in the context of this dissertation, and provides a motivation for investigating mode coupling as a means for reducing vibration in passively-isolated UPM machines. Section 1.3 states the scientific and engineering objectives of this dissertation, followed by a summary of the contributions and an outline of the dissertation.

1.2. Background and Motivation

1.2.1. Ultra-Precision Manufacturing Machines

Ultra-precision manufacturing (UPM) machines are designed to fabricate and measure complex parts having micrometer-level features and nanometer-level tolerances/surface finishes [16-19]. They enable the production of micro devices that are largely responsible for the advances in the electronics, biomedical, communications and other high-tech industries [17,20,21]. As shown in Figure 1.1, examples of UPM machines include ultra-precision machine tools [22-25], wafer scanners [26] and micro coordinate measurement machines (CMMs) [27], to name a few. The accuracy, productivity and functionality demands on UPM machines are steadily growing due to the rapid increase of cutting-edge applications that require complex micro devices [16-18,28]. In addition, there is growing interest in low-cost and energy efficient machines that help make manufacturing more sustainable.

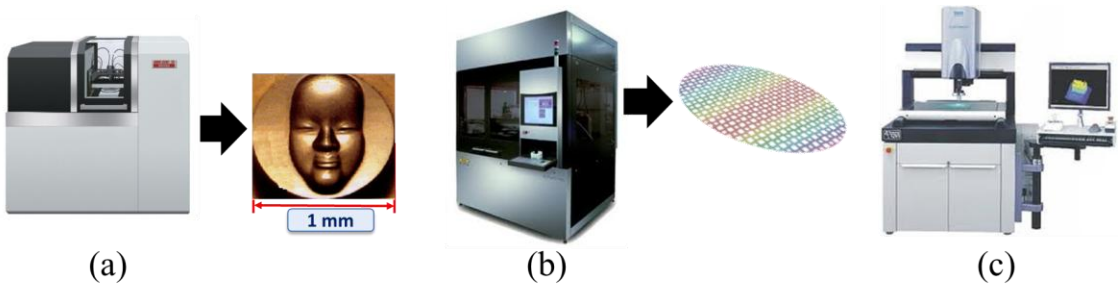

Figure 1.1: Examples of UPM Machines: (a) Ultra-Precision Machine Tools (b) Wafer Scanner and (c) Micro Coordinate Measurement Machines

UPM machines, irrespective of the specifics of their design and functions, all possess two important features that fall within the scope of this research: (i) Due to the very high accuracy requirements placed on UPM machines, they must be mounted on an isolated base (Figure 1.2) to minimize the detrimental effects of horizontal and vertical floor vibrations on their performance [13,14,26,29]; (ii) To deliver the relative motions between "tool" and "workpiece," needed for their respective manufacturing/measurement processes, UPM machines are equipped with at least one moving axis, which ideally should travel as fast as possible to ensure high productivity of the process [13,14,29].

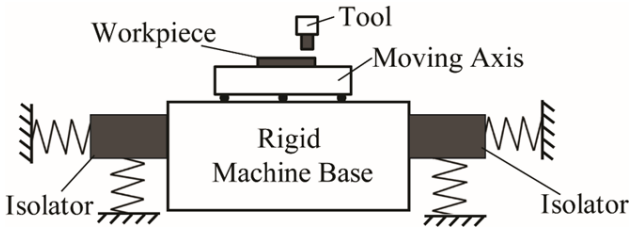

Figure 1.2: Essential Features of an Ultra-Precision Manufacturing Machine

1.2.2. Vibration Reduction (Isolation) in UPM machines

As shown in Figure 1.2, an isolated UPM machine can be represented by a rigid base (typically a granite slab [15,27,30]) supported by vibration isolators which are represented as springs. The primary purpose of the isolation system in UPM machines is to prevent ground vibrations from being transmitted to the machine (i.e. to minimize *transmissibility*) [13,14,29,31]. However, the isolation system must also ensure that the inertial reaction forces resulting from the rapid motion of the axes do not cause lingering low-frequency vibration of the base (i.e., *residual vibration*) [13,14,31-33].

Vibration isolation systems can either be passive, active or semi-active [15,34,35]. Passive isolators provide a simple, cost-effective, energy-neutral and reliable means of vibration isolation [13,14]. However, they suffer from two very significant drawbacks. First, to achieve good isolation, the stiffness of the isolator should be made as low as possible. Having low stiffness however leads to large static displacements of the isolated system due to onboard disturbances [36]; it also leads to increased residual vibration. Residual vibration is objectionable not only because it is detrimental to the accuracy of UPM machines but because it also significantly reduces the achievable speeds and accelerations of UPM machines thus impacting productivity. The second, but related, problem of passive isolators concerns damping. Adding damping to the isolators helps reduce the transmissibility at resonance as well as reduce residual vibration. However, it also increases the transmissibility at frequencies above resonance, particularly for viscously damped isolators [13,14,26,29,35].

The large static displacement problem caused by low isolator stiffness is usually solved in UPM machines by adding an automatic re-leveling system to the isolated machine [13,31,36,37]. Re-levelers are essentially low-bandwidth proportional-integral (PI) controllers which help eliminate the unwanted static displacements of the isolated base. To mitigate the transmissibility trade-off caused by damping, *pneumatic isolators* (air springs) are used to isolate most UPM machines [15,27,30,38-40]. Due to the orifice-type damping mechanism used in pneumatic isolators, damping can be added to high-amplitude residual vibration without significantly affecting transmissibility due to low-amplitude ground motion [31].

Active and semi-active isolation systems use sensors and actuators connected to a control system to mitigate vibration [34]. They are able to overcome some of the shortcomings of strictly passive systems. For instance, they are used to reduce transmissibility at very low frequencies (less than 1 Hz) for which passive means are impractical [31,38]. However, only a small subset of UPM machines, like atomic force and scanning tunneling microscopes (AFMs and STMs) need such low level of transmissibility [31]. When configured as so-called "skyhook dampers," active and semi-active isolation systems are able to overcome the tradeoff between reducing residual vibration and increasing transmissibility at high frequencies due to the addition of damping. However, a major drawback of using active isolation systems in practice is their hefty price tag [13,14,29,31,35]; they could sometimes cost up to 90% more than passive systems. Other problems associated with active and semi-active systems include increased energy

consumption, increased complexity and the associated loss of reliability, stability issues and the risk of catastrophic failure [13,14,29,31,35,41].

1.2.3. Motivation for Mode Coupling

Based on the discussion in Section 1.2.2 above, one observes that if superior vibration reduction can be achieved using passive isolators then significant reductions in costs, energy consumption and complexity can be gained by utilizing passive isolators instead of active or semi active isolators. For this reason, a lot of research effort has been poured into optimizing the properties (e.g., stiffness and damping) and/or placement of passive isolators to maximize their vibration reduction potential [26,42-53]. In the context of UPM machine design, optimization of isolation system stiffness and damping is somewhat impractical. This is because isolators are commercially available as discrete units with nominal stiffness and damping values; there is not much room to adjust the stiffness and damping of a given isolator to match their optimal values for a given UPM machine [31]. However, the designer has some degree of flexibility regarding the placement of each unit [13,14,31,54-56]. Therefore, from the standpoint of a machine designer, there is a lot of practical value in knowing how best to locate passive isolators to minimize unwanted vibration.

A long-standing rule of thumb in passive isolation system design, recommended in academic literature and industrial practice, is to align the isolator mounting locations with the center of gravity of the machine, such that the vibration modes of the isolated machine are decoupled [26,31,54-56]. There are two important reasons for this rule. First, decoupling ensures that vertical ground motions are not transmitted to the typically more-sensitive horizontal axes of the machine. This is because, generally, vertical ground motions are more severe than horizontal ground motions [14,29]. Secondly, decoupling ensures that two or more resonance peaks are not created in the transmissibility response of the machine, thereby reducing the rate of attenuation after the first resonance [57]. UPM machine designers therefore strive for this ideal, even though it is very challenging in practice to locate the isolators exactly at the CG [26]. Elastic decoupling by direct means (e.g., supporting the machine in a cradle structure) or indirect means (e.g., focalization), as shown in Figure 1.3, are popular approaches for (partially) achieving modal decoupling [26,31,55,57].

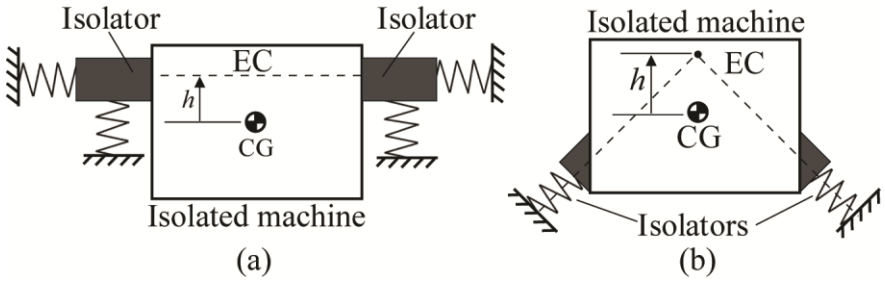

Figure 1.3: Modal Decoupling (i.e., $h = 0$) using (a) Direct Elastic Decoupling, and (b) Indirect Elastic Decoupling (or Focalization). Note that EC Represents the Elastic Center of the Machine

There is however anecdotal evidence scattered in the literature that suggests that coupling vibration modes could help improve the response of passively-isolated systems. For example, Rivin [14] points out that even though the proper selection of the position of isolators is important, especially for reducing residual vibration and increasing the effective rigidity of the machine structure, UPM designers rarely give it the attention it deserves. Debra [13] experimentally observed that, for pneumatic isolators, mode coupling could help to reduce rocking motion (residual vibration). He hypothesized that the reduction in vibration was because coupling transferred some damping from the more highly damped vertical, to the less damped horizontal directions [13,58]. Ryaboy [36] showed reductions in the transmissibility of an isolation system when its isolators were located away from the CG. However, a lot of questions are yet to be answered. For example: (i) What is the scientific basis for the observed favorable effects of mode coupling on vibration reduction in UPM machines, and what roles do the various system variables play? (ii) How can the system be designed to maximize the benefits of mode coupling while avoiding any shortcomings? Finding the answers to these questions is the primary motivation for this research.

1.3. Objectives, Contributions and Outline of Dissertation

This dissertation has two objectives. The scientific objective of the dissertation is to provide a fundamental understanding of the effect of mode coupling on the vibrations of passively isolated systems (in the context of UPM machines). The engineering objective of the dissertation is to provide design guidelines and tools for using mode coupling to reduce vibrations of UPM machines.

The dissertation has three primary contributions:

1) It uses eigenvalue and perturbation analyses on a single-variable, proportionally (or modally) damped, planar isolation system to demonstrate that the drastic reduction of vibration caused by mode coupling is primarily linked to so-called "critical configurations" induced by curve veering and mode localization. It therefore clears the misconception purported in academic literature [13] and industrial practice [31] that the vibration-reduction effects of mode coupling on UPM machines are simply linked to damping.

2) It proves analytically that mode coupling (with or without damping effects included) is almost always better than the recommended practice of modal decoupling with regard to vibration reduction in passively-isolated UPM machines, providing that mode coupling is properly carried out. It therefore provides design guidelines for exploiting weak mode coupling for vibration reduction in UPM machines.

3) It proposes a framework for reformulating the generalized (multivariable, 3-D) UPM isolator placement problem as a linear feedback controller whose gains represent isolator locations. It thus provides a powerful engineering tool for using linear control theory, in all its wealth and elegance, for the optimization and analyses of passive isolator locations.

The contributions described above are detailed in three self-contained chapters, representing three journal articles by the author. In the first manuscript [1] (i.e., Chapter 2), mode coupling is theoretically analyzed using a modally damped, planar system. It shows that weakly coupling the vibration modes of the isolated system by altering the location of the vibration isolators provides conditions which allow for the drastic reduction of residual vibrations due to mode localization. An objective function which minimizes residual vibration energy is defined. Perturbation analyses of the objective function reveal that the recommended practice of decoupling the vibration modes more often than not leads to sub-optimal results in terms of residual vibration reduction. The analyses also provide guidelines for correctly locating the isolators so as to reduce residual vibration for modally damped isolation systems. Simulations and experiments conducted on a passively-isolated ultra-precision machine tool are used to validate the findings of the chapter.

In the second manuscript [2] (i.e., Chapter 3), the work reported in Chapter 2 is broadened by investigating the effect of mode coupling on the residual vibration of UPM machines with non-proportional (NP) damping (still using a planar system). It also analyzes the effects of mode coupling on the reduction of ground vibration (i.e., transmissibility). The analyses reveal that, even though NP damping changes the vibration behavior of the machine compared to modal damping, mode coupling still provides ample opportunities to (simultaneously) reduce residual vibration and transmissibility. Guidelines for properly designing a UPM machine to best exploit weak mode coupling for vibration reduction in non-proportionally damped isolation systems are provided and validated through simulations and experiments. Large reductions in both residual vibrations and transmissibility are demonstrated.

In the third manuscript [3] (i.e., Chapter 4), the problem of optimally locating passive vibration isolators (i.e., exploiting mode coupling) to minimize unwanted vibration caused by exogenous disturbance forces is investigated for a generalized (multivariable, 3-D) isolation system. The stiffness and damping properties of the isolators are assumed to be known, leaving the isolator locations, which are nonlinearly related to system states, as unknown optimization variables. An approach for reformulating the nonlinear isolator placement problem as a linear time invariant (LTI) feedback control problem, by linking the control forces to measured outputs using a non-zero feedforward term, is proposed. Accordingly, the isolator locations show up within a static output feedback gain matrix which can be optimized, using methods from optimal control theory, to minimize the H_2 and/or H_∞ norms of transfer functions representing unwanted vibration. The proposed framework also allows well-established LTI control theories to be applied to the analyses of the optimal isolator placement problem and its results. The merits of the proposed approach are demonstrated using single- and multi-variable case studies related to isolator placement UPM machines.

Chapter 5 presents a summary of the conclusions and future work that emanate from this doctoral dissertation research.

CHAPTER 2
MINIMIZATION OF THE RESIDUAL VIBRATIONS OF ULTRA-PRECISION MANUFACTURING MACHINES VIA OPTIMAL PLACEMENT OF VIBRATION ISOLATORS

2.1. Introduction

This chapter uses the planar dynamics of a passively-isolated system to show that coupling the vibration modes of the isolated system by altering the location of the isolators provides conditions which allow for the drastic reduction of residual vibrations. It proffers analysis-based guidelines for selecting the location of the isolators such that residual vibration is reduced using mode coupling.

The outline of this chapter is as follows. In Section 2.2, the effects of isolator location on the planar (2-D) dynamics of a simple isolated system are studied using a mathematical model. An objective function which minimizes residual vibration energy is then defined in Section 2.3 and used, in conjunction with a perturbation method, to analytically demonstrate the sub-optimality of decoupling vibration modes, in most situations. Moreover, practical design guidelines for judiciously placing vibration isolators to achieve residual vibration reduction are deduced. Finally, in Section 2.4, simulations and experiments are conducted on an ultra-precision five-axis machine tool, followed by discussions and conclusions.

2.2. Modeling and Analysis

2.2.1. Modeling

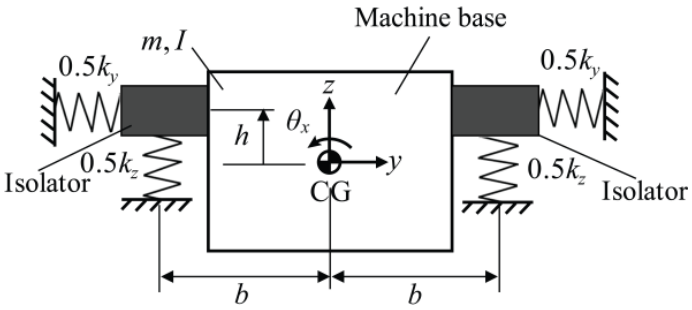

Figure 2.1: Planar Model of Isolated Machine

Figure 2.1 shows a 2-D model of an isolated machine; m and I are respectively the mass and centroidal moment of inertia of the machine base about the x-axis; k_y and k_z are the combined stiffness of the isolators in the y and z directions, respectively; b is the half-span of the isolators while h is the vertical height of the isolator mounting point, measured from the center of gravity (CG) of the base. The vibrations of the machine base are assumed to occur only in the y-z plane. Such planar analyses can be applied, for instance, when the machine's structure is symmetrical in the x-direction. In a general sense, the dynamics of passive (typically pneumatic) isolators is nonlinear [40,59]. However, for small vibratory motions, linear models are adequate [40].

Assuming, for theoretical convenience, that the system in Figure 2.1 is proportionally damped, its equation of motion is given by

$$\mathbf{M}\ddot{\mathbf{u}} + \mathbf{K}\mathbf{u} = \mathbf{0}, \tag{2.1}$$

where **M**, **K** and **u** are respectively the mass matrix, stiffness matrix and vector of displacements of the system. They are given by

$$\mathbf{M} = \begin{bmatrix} m & 0 & 0 \\ 0 & m & 0 \\ 0 & 0 & I \end{bmatrix}, \mathbf{K} = \begin{bmatrix} k_y & 0 & -k_y h \\ 0 & k_z & 0 \\ -k_y h & 0 & k_\theta + k_y h^2 \end{bmatrix}, \mathbf{u} = \begin{Bmatrix} y \\ z \\ \theta_x \end{Bmatrix}, \tag{2.2}$$

with $k_\theta = b^2 k_z$. Note that in Eq.(2.1), the damping of the system is not explicitly considered because a proportionally damped system can first be analyzed as an undamped system after which damping can be directly introduced into the modes (as modal damping) [60].

As can be inferred from Eq.(2.2), only the dynamics in the y and θ_x directions are coupled as a result of h. Since the main purpose of this chapter is to study the effects of h on the dynamics of the isolated system, we focus on the coupled subsystem,

$$\mathbf{M}=\begin{bmatrix} m & 0 \\ 0 & I \end{bmatrix}, \mathbf{K}=\begin{bmatrix} k_y & -k_y h \\ -k_y h & k_\theta + k_y h^2 \end{bmatrix}, \mathbf{u}=\begin{Bmatrix} y \\ \theta_x \end{Bmatrix}. \tag{2.3}$$

Eq.(2.3) gives rise to two vibration modes, described by the coordinates y and θ_x, whose behaviors as h is varied need to be analyzed.

2.2.2. Analysis of Eigen Solutions

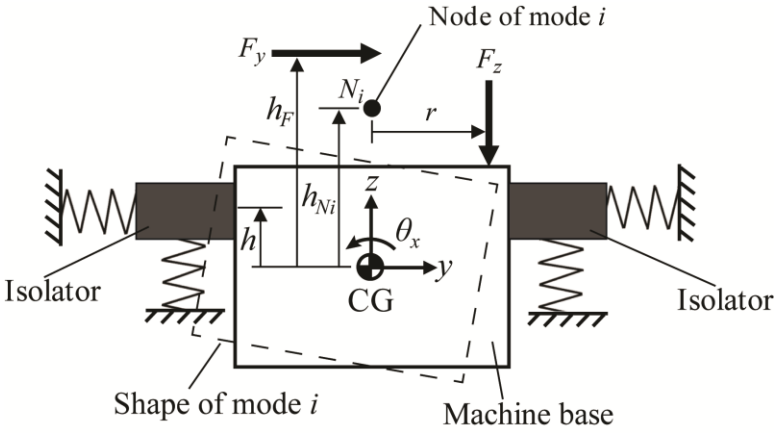

Figure 2.2: Mode Shape of Isolated Machine

Figure 2.2 shows the shape of a rocking vibration mode i (where i = 1, 2) of the isolated machine about its node N_i. The node represents the point about which the isolated system rotates when vibrating in a particular mode; F_y and F_z are the inertial forces due to masses moving on the isolated system in the y and z directions, respectively; h_F and r respectively indicate the perpendicular distances of F_y and F_z from the CG; h_{Ni} is the height of N_i relative to the CG. As observed from the figure, the residual (rocking) vibrations of the isolated machine can be caused by the moments created by F_y or F_z about any node N_i of the isolated system. The influence of F_y depends on its moment arm $h_F - h_{Ni}$ about N_i, and can be represented by the frequency response function (FRF) between F_y and the angular acceleration $\ddot{\theta}_x$ of the base; i.e.

$$H_y(\omega)=\frac{-\omega^2\theta_x}{F_y}=\sum_{i=1}^{2}\frac{h_F-h_{Ni}}{I_{qi}}\frac{\omega^2}{-\omega^2+2j\omega\zeta_i\omega_{ni}+\omega_{ni}^2}. \tag{2.4}$$

Similarly, the residual vibrations caused by F_z can be described by the FRF

$$H_z(\omega) = \frac{-\omega^2 \theta_x}{F_z} = \sum_{i=1}^{2} \frac{r}{I_{qi}} \frac{\omega^2}{-\omega^2 + 2j\omega\zeta_i\omega_{ni} + \omega_{ni}^2}. \tag{2.5}$$

In Eqs.(2.4) and (2.5), ω_{ni} and I_{qi} respectively denote the natural frequency and modal inertia of each vibration mode i, while ω represents excitation frequencies; ζ_i is the modal damping added to account for the proportional damping of the isolated system which was ignored in Eq.(2.1) and j is the unit imaginary number. To understand how H_y and H_z are affected by mode coupling, the variation of ω_{ni}, h_{Ni} and I_{qi} as functions of h is studied. Ideally, ζ_i would also change as a function of h but we assume that the modal damping ratios remain constant as h is varied.

To facilitate the analysis, a non-dimensional natural frequency for mode i (i.e., $\tilde{\omega}_{ni}$) is defined as

$$\tilde{\omega}_{ni} \triangleq \omega_{ni} \Big/ \sqrt{k_y / m} = \sqrt{\frac{1+\varepsilon^2+\tilde{h}^2 \mp \sqrt{\left(1+\varepsilon^2+\tilde{h}^2\right)^2 - 4\varepsilon^2}}{2}}, \tag{2.6}$$

where $\tilde{h}$ is the non-dimensional height corresponding to h and ε is a non-dimensional variable defined as

$$\tilde{h} \triangleq \frac{h}{\rho}, \quad \varepsilon \triangleq \sqrt{\frac{k_\theta m}{k_y I}}, \quad \rho \triangleq \sqrt{\frac{I}{m}}. \tag{2.7}$$

Similarly, $\tilde{h}_{Ni}$ and $\tilde{I}_{qi}$, the non-dimensional node height and modal inertia are defined as

$$\tilde{h}_{Ni} \triangleq \frac{h_{Ni}}{\rho} = \frac{1}{\tilde{h}}\left(\varepsilon^2 + \tilde{h}^2 - \tilde{\omega}_{ni}{}^2\right), \;\; \tilde{I}_{qi} \triangleq \frac{I_{qi}}{I} = \tilde{h}_{Ni}^2 + 1. \tag{2.8}$$

Using the non-dimensional parameters, the FRFs defined in Eqs.(2.4) and (2.5) are re-written as

$$H_y = \frac{1}{m\rho} \sum_{i=1}^{2} A_{yi} X_i, \qquad H_z = \frac{1}{m\rho} \sum_{i=1}^{2} A_{zi} X_i \;, \tag{2.9}$$

where A_{yi} and A_{zi} are the non-dimensional modal participation factors for H_y and H_z, respectively, while X_i is the non-dimensional modal FRF. They are given by

$$A_{yi} = \frac{\tilde{h}_F - \tilde{h}_{Ni}}{\tilde{I}_{qi}}, \qquad A_{zi} = \frac{\tilde{r}}{\tilde{I}_{qi}}, \qquad X_i = \frac{\tilde{\omega}^2}{-\tilde{\omega}^2 + 2j\tilde{\omega}\zeta_i\tilde{\omega}_{ni} + \tilde{\omega}_{ni}^2}, \tag{2.10}$$

where

$$\tilde{h}_F \triangleq \frac{h_F}{\rho}, \qquad \tilde{r} \triangleq \frac{r}{\rho}, \qquad \tilde{\omega} \triangleq \omega \Big/ \sqrt{k_y / m}. \tag{2.11}$$

Figures 2.3 to 2.5 show the behaviors of $\tilde{\omega}_{ni}$, $\tilde{h}_{Ni}$ and $\tilde{I}_{qi}$ as functions of $\tilde{h}$ for various combinations of m, I, k_y and k_θ (as embodied in ε). To simplify the discussion that follows, the distinction between the dimensionless and the actual variables (i.e., the "~" accent) is ignored in the rest of this chapter, except when needed to avoid ambiguity.

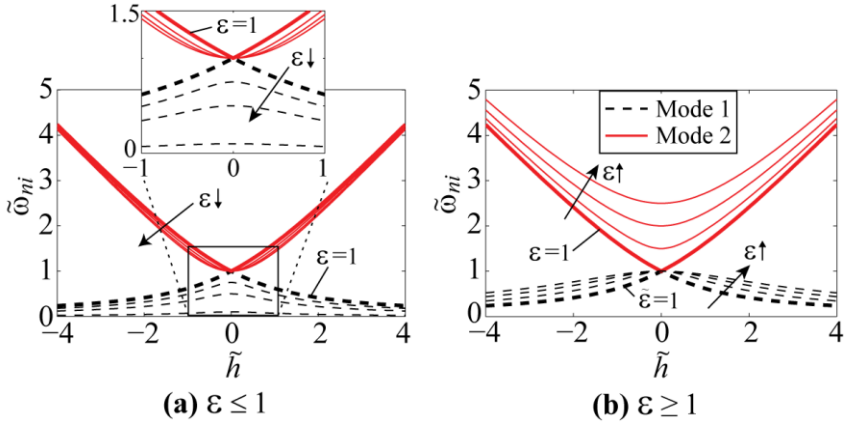

Figure 2.3: Variation of Dimensionless Natural Frequencies $\tilde{\omega}_{ni}$ as Functions of Dimensionless Isolator Height $\tilde{h}$ for Various Values of ε

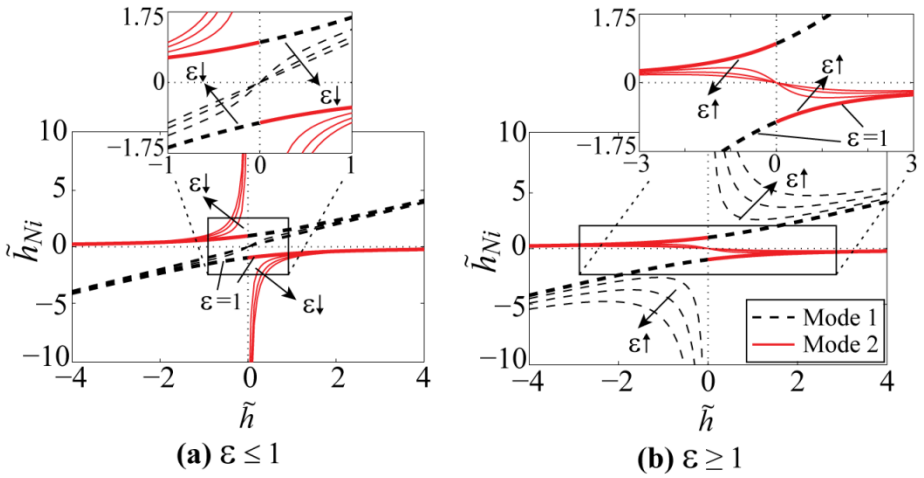

Figure 2.4: Variation of Dimensionless Node Heights $\tilde{h}_{Ni}$ as Functions of Dimensionless Isolator Height $\tilde{h}$ for Various Values of ε

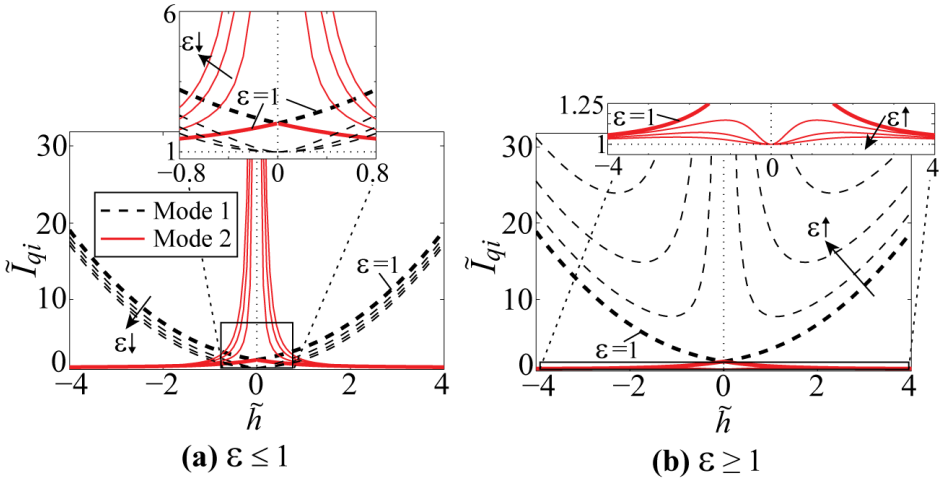

Figure 2.5: Variation of Dimensionless Modal Inertias $\tilde{I}_{qi}$ as Functions of Dimensionless Isolator Height $\tilde{h}$ for Various Values of ε

The behavior of each parameter can be grouped into two characteristic cases: $\varepsilon < 1$ (i.e., $k_\theta/I < k_y/m$) and $\varepsilon > 1$ (i.e., $k_\theta/I > k_y/m$); $\varepsilon = 1$ is a special (degenerate) case [61] that needs to be considered separately.

From Figure 2.3, we see that as h increases positively or negatively, ω_{n1} reduces while ω_{n2} increases monotonically. At $h = 0$, ω_{n1} and ω_{n2} come closest to each other and then suddenly veer off with large curvatures without crossing. Crossing occurs only in the special case when $\varepsilon = 1$

and $h = 0$. Notice that as ε deviates from unity, the distance between ω_{n1} and ω_{n2} at $h = 0$ increases.

According to Figure 2.4, when $\varepsilon < 1$, Mode 1 starts out at $h = 0$ as a purely rotational mode about the CG (i.e., $h_{N1} = 0$). As h increases positively, h_{N1} increases monotonically while for negative h, it decreases monotonically. Conversely, when $\varepsilon > 1$, Mode 1 is a purely translational mode (i.e., $h_{N1} = \infty$) at $h = 0$. As h increases positively, h_{N1} rapidly decreases from $+\infty$ until $h = \sqrt{\varepsilon^2 - 1}$ when it suddenly changes direction and starts to increase. For negative h, the same trend is seen in h_{N1} but its sign is reversed. It can also be seen from Figure 2.4 that h_{N2} has a behavior that is qualitatively opposite to that of h_{N1} for both $\varepsilon < 1$ and $\varepsilon > 1$. For instance, except at $h = 0$, h_{N1} always has the same sign as h while h_{N2} always has a sign opposite to that of h.

For the special case of $\varepsilon = 1$, the mode shapes exhibit a peculiar behavior at $h = 0$ known as mode-switching [62]. When the natural frequencies of the modes cross each other, the lower frequency mode assumes all the characteristics of the higher frequency mode (and vice versa). Notice that at $h = 0$, instead of having purely translational and rotational modes as observed for $\varepsilon \neq 1$, the two modes share their characteristics and so act like a coupled system [63, 64]. One can therefore say that the system is never truly decoupled for $\varepsilon = 1$.

Figure 2.5 shows that the modal inertias I_{qi} follow a similar trend as the node heights, except that their behavior is symmetrical about $h = 0$. Observe that the modal inertia is lowest when the mode is purely rotational (i.e., when $h_{Ni} = 0$) and maximum (infinite) when the mode is purely translational.

The just-described drastic behavior of ω_{ni}, h_{Ni} and I_{qi} as functions of h is related to closely-linked and well-studied phenomena known as eigenvalue curve veering [61-65] and mode localization [66-68]. Curve veering and mode localization are described as catastrophic-type phenomena because small changes in the system parameters result in large variations in the natural frequencies and mode shapes [68]. One very pertinent implication of curve veering and mode localization for vibration isolation systems is their potential to create critical configurations in structures subject to wide-band input, as first indicated by Igusa [63]. When critical configurations exist in a structure, small variations in parameters can lead to large variations in the response. For example, resonance and anti-resonance are well-known critical configurations of harmonically loaded structures. Critical configurations can be useful in design if minor

modifications significantly reduce the system's response [63], as will be shown in the subsequent sections to be true for isolation system design.

2.3. Effects of Isolator Location (Mode Coupling) on Residual Vibration Minimization

The variance of a system H in response to a zero-mean, band-limited white noise input of unit magnitude is given by

$$\sigma_H^2 = \int_{\omega_{min}}^{\omega_{max}} \left|H(\omega)\right|^2 d\omega. \tag{2.12}$$

It is a measure of the energy of the system's response to stationary random excitations [69,70] but also provides a qualitative indicator of the system's transient response magnitude [69-71]. Consequently, the goal of minimizing the residual vibrations due to F_y and F_z can be indirectly achieved, based on Eq.(2.9), by minimizing the variances σ^2_{Hy} and σ^2_{Hz} w.r.t. $\tilde{h}$.

In calculating σ^2_{Hy} and σ^2_{Hz}, $\omega_{min} = 0$ is used to ensure that the low-frequency components of the response are captured; ω_{max} is kept as a design variable which can be chosen based on the highest frequency content of the input signal and/or the level of attenuation provided by H_y or H_z.

The analytical integrals for σ^2_{Hy} and σ^2_{Hz} result in very complicated mathematical functions whose stationary points cannot be derived analytically in closed-form. Consequently, they do not provide intuitive design guidelines for the optimal selection of h, which is our goal in this chapter. Therefore, in the following subsections, we perform perturbation analyses of σ^2_{Hy} and σ^2_{Hz} about $h = 0$ to provide machine designers with the conditions for which the coupled system is preferable over the decoupled system, in terms of residual vibration minimization. $\varepsilon = 1$ is not considered in our analysis because it represents a degenerate situation that can very rarely (if ever) be achieved in practice.

2.3.1. Perturbation Analysis of σ^2_{Hy}

Based on Eq.(2.9), σ^2_{Hy} can be written as

$$\sigma^2_{Hy} = \left(\frac{1}{m\rho}\right)^2 \left(A^2_{y1}\Gamma_1 + A^2_{y2}\Gamma_2 + 2A_{y1}A_{y2}\Gamma_3\right), \tag{2.13}$$

where Γ_1, Γ_2 and Γ_3 are given by

$$\Gamma_1 = \int_0^{\tilde{\omega}_{max}} |X_1|^2 \, d\tilde{\omega}, \quad \Gamma_2 = \int_0^{\tilde{\omega}_{max}} |X_2|^2 \, d\tilde{\omega}, \quad \Gamma_3 = \int_0^{\tilde{\omega}_{max}} \left(\mathrm{Re}\, X_1 \, \mathrm{Re}\, X_2 + \mathrm{Im}\, X_1 \, \mathrm{Im}\, X_2 \right) d\tilde{\omega}. \tag{2.14}$$

The first-order Taylor expansion of Eq.(2.13) about $\tilde{h} = 0$ yields

$$\sigma_{Hy}^2 \cong \left(\frac{1}{m\rho} \right)^2 \left(C_{y0} + C_{y1} \tilde{h} \right), \tag{2.15}$$

C_{y0} and C_{y1} are defined as

$$C_{y0} = \begin{cases} \tilde{h}_F^2 \Gamma_1^\circ & \varepsilon < 1 \\ \tilde{h}_F^2 \Gamma_2^\circ & \varepsilon > 1 \end{cases}, \quad C_{y1} = \begin{cases} -2\tilde{h}_F \dfrac{1}{|\varepsilon^2 - 1|} \left(\Gamma_1^\circ - \Gamma_3^\circ \right) & \varepsilon < 1 \\ 2\tilde{h}_F \dfrac{1}{|\varepsilon^2 - 1|} \left(\Gamma_2^\circ - \Gamma_3^\circ \right) & \varepsilon > 1 \end{cases}. \tag{2.16}$$

The superscript $^\circ$ attached to the variables in Eq.(2.16) indicates that they are each evaluated at $h = 0$. Recall that $C_{y1} = 0$ is a necessary condition for σ^2_{Hy} to have a local minimum at $h = 0$. According to Eq.(2.16), besides the typically impractical case of $h_F = 0$, $C_{y1} = 0$ only if $\Gamma_1^\circ - \Gamma_3^\circ = 0$ or $\Gamma_2^\circ - \Gamma_3^\circ = 0$ for $\varepsilon < 1$ and $\varepsilon > 1$, respectively. Γ_1°, Γ_2° and Γ_3° are functions of ε, $\tilde{\omega}_{max}$ and ζ_i° (i.e., value of ζ_i at $h = 0$). They can be represented graphically as the areas under the curves labeled 1, 2 and 3 in Figure 2.6. As the plot suggests, $\Gamma_1^\circ - \Gamma_3^\circ$ or $\Gamma_2^\circ - \Gamma_3^\circ$ are not likely to be zero under most circumstances. To determine the conditions for which $C_{y1} = 0$, $\Gamma_1^\circ - \Gamma_3^\circ$ and $\Gamma_2^\circ - \Gamma_3^\circ$ are computed numerically (using the trapezoidal integration method) for values of ζ_1° and ζ_2° over the interval [0.01, 0.5] with a step size $\Delta\zeta = 0.01$. The selected range for ζ_1° and ζ_2° encompasses the practical range of modal damping ratios used in vibration isolation systems. The upper limit of integration ω_{max} is chosen such that $\alpha = 1.005$ in Figure 2.6 (b). In other words, the choice of ω_{max} ensures that the larger of $|X_1(\omega_{max})|$ and $|X_2(\omega_{max})|$ is within 0.5% of the high frequency asymptote of $|X_i|$ (i.e., $|X_i| = 1$) so that the contributions of both modes are fully captured. Figure 2.7 (a) and (b) respectively show the contour plots of $\Gamma_1^\circ - \Gamma_3^\circ = 0$ and $\Gamma_2^\circ - \Gamma_3^\circ = 0$ for various values of ε. For any given $\varepsilon \neq 1$, only the values of ζ_i° on the corresponding ε curve can give rise to a local minimum in σ^2_{Hy} for the decoupled system. To obtain minimal σ^2_{Hy} for the majority of ζ_i° which do not lie on the curve for any given $\varepsilon \neq 1$, the system would have to be coupled.

Consequently, the perturbation analysis on σ^2_{Hy} demonstrates that, if h is selected properly, coupling vibration modes using $h \neq 0$ is in most scenarios better than decoupling the modes, when the objective is to reduce residual vibrations caused by horizontal excitation forces. Section 2.3.3 provides insights on how to properly select h for the coupled system.

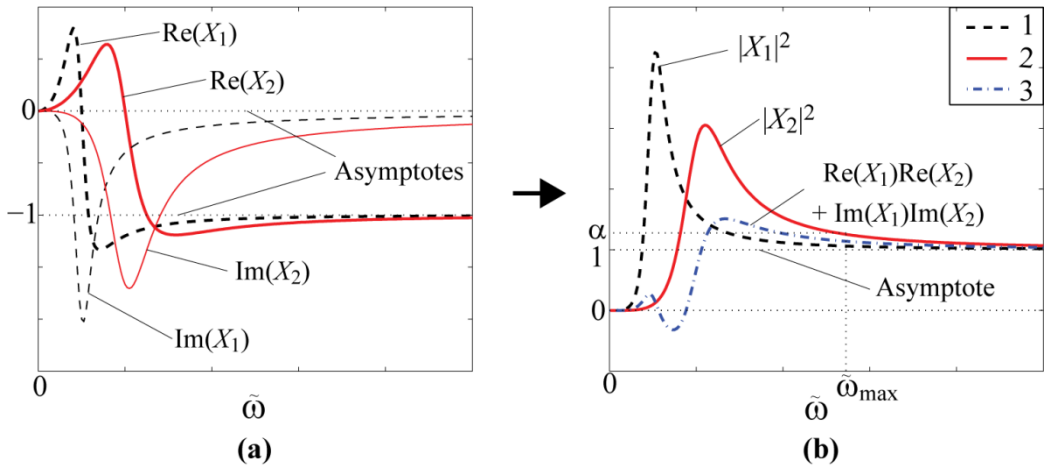

Figure 2.6: Characteristic Plots of (a) X_1 and X_2 (b) Curves for Calculating Γ_1°, Γ_2° and Γ_3°

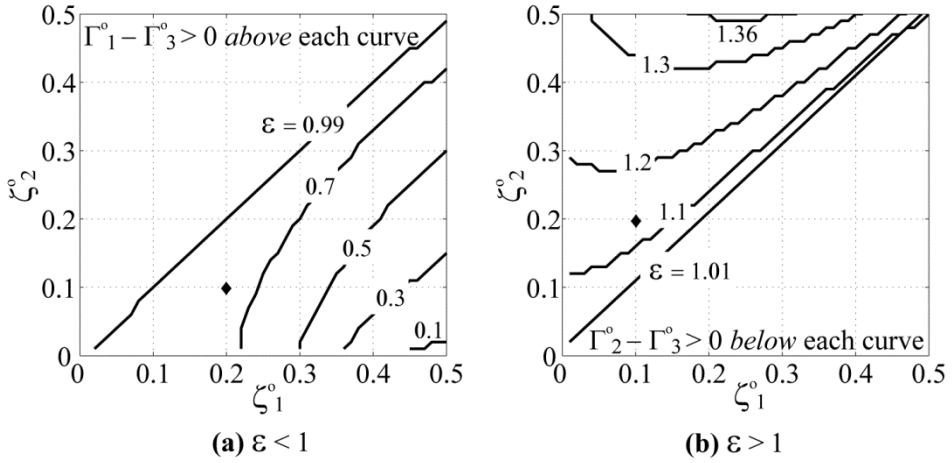

Figure 2.7: Contour Plots of (a) $\Gamma_1^\circ - \Gamma_3^\circ = 0$ (b) $\Gamma_2^\circ - \Gamma_3^\circ = 0$ as Functions of ζ_1° and ζ_2° for Various Values of ε

2.3.2. Perturbation Analysis of σ^2_{Hz}

Similar to Eq.(2.13), σ^2_{Hz} can be expressed as

$$\sigma^2_{Hz} = \left(\frac{1}{m\rho}\right)^2 \left(A^2_{z1}\Gamma_1 + A^2_{z2}\Gamma_2 + 2A_{z1}A_{z2}\Gamma_3\right), \tag{2.17}$$

where Γ_1, Γ_2 and Γ_3 retain their definitions given in Eq.(2.14). The second-order Taylor expansion of σ^2_{Hz} about $h = 0$ is given by the equation

$$\sigma^2_{Hz} \cong \left(\frac{1}{m\rho}\right)^2 \left(C_{z0} + C_{z1}\tilde{h} + \frac{C_{z2}}{2}\tilde{h}^2\right), \tag{2.18}$$

where

$$C_{z0} = \begin{cases} \tilde{r}^2\Gamma_1^\circ & \varepsilon < 1 \\ \tilde{r}^2\Gamma_2^\circ & \varepsilon > 1 \end{cases}, \quad C_{z1} = 0, \quad C_{z2} = \begin{cases} -\dfrac{4\tilde{r}^2}{(\varepsilon^2-1)^2}\left(\Gamma_1^\circ - \Gamma_3^\circ\right) + \tilde{r}^2\dfrac{\partial^2\Gamma_1^\circ}{\partial\tilde{h}^2} & \varepsilon < 1 \\ -\dfrac{4\tilde{r}^2}{(\varepsilon^2-1)^2}\left(\Gamma_2^\circ - \Gamma_3^\circ\right) + \tilde{r}^2\dfrac{\partial^2\Gamma_2^\circ}{\partial\tilde{h}^2} & \varepsilon > 1 \end{cases}, \tag{2.19}$$

The mathematical expression for $\partial^2\Gamma_i^\circ / \partial\tilde{h}^2$ is given by

$$\frac{\partial^2\Gamma_i^\circ}{\partial\tilde{h}^2} = \frac{\partial^2\tilde{\omega}_{ni}^\circ}{\partial\tilde{h}^2}\cdot\frac{\partial\Gamma_i^\circ}{\partial\tilde{\omega}_{ni}} = \frac{\varepsilon^2}{\varepsilon^2-1}\cdot\int_0^{\tilde{\omega}_{max}} \frac{4\varepsilon\tilde{\omega}^4\left[\tilde{\omega}^2(1-2\zeta_i^{\circ 2}) - \varepsilon^2\right]}{\left[\tilde{\omega}^4 + \varepsilon^4 - 2\varepsilon^2\tilde{\omega}^2(1-2\zeta_i^{\circ 2})\right]^2} d\tilde{\omega} \quad (i = 1, 2). \tag{2.20}$$

As seen from Eq.(2.19), C_{z1} is always zero hence $h = 0$ is always a stationary point of σ^2_{Hz}. The nature of the stationary point (i.e., local maximum, minimum or inflection point) is determined by numerically evaluating the sign of C_{z2} for various combinations of ζ_1°, ζ_2° and ε. The same numerical technique and ζ_i° values used in Section 2.3.1 for C_{y1} are employed in the analysis. Figure 2.8 (a) and (b) show the contour plots of $C_{z2} = 0$ for various values of $\varepsilon < 1$ and $\varepsilon > 1$, respectively. The similarity between Figures 2.7 and 2.8 indicates that the first term of C_{z2} dominates its behavior. However, the sign of C_{z2} is opposite those of $\Gamma_1^\circ - \Gamma_3^\circ$ and $\Gamma_2^\circ - \Gamma_3^\circ$. Consequently, C_{z2} is negative for most combinations of ζ_1° and ζ_2° thus implying that $h = 0$ is most often a local maximum of σ^2_{Hz}. The implication is that coupling vibration modes (i.e., selecting $h \neq 0$) is more often better than decoupling, in terms of reducing residual vibrations caused by F_z. Of course, this conclusion is guaranteed to be true only if h is selected in the immediate vicinity of $h = 0$. Further insights on the practical implications of Figure 2.8 on the selection of h are provided in Section 2.3.3 below.

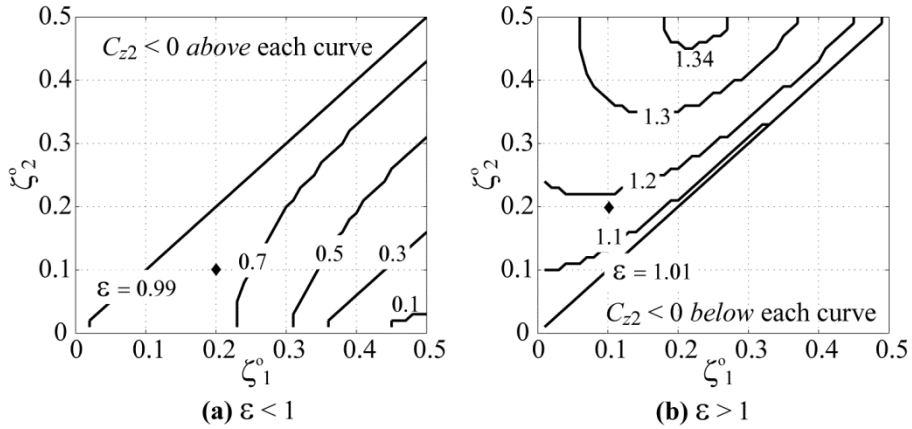

Figure 2.8: Contour Plots of $C_{z2} = 0$ as Functions of ζ_1° and ζ_2° for Various Values of ε

2.3.3. Practical Design Guidelines Based on Perturbation Analyses

The results of the perturbation analyses presented above can provide useful hints to a designer on when and how to couple the vibration modes of a given UPM machine by changing h. In this section, first two practical scenarios are presented to demonstrate how the results from the analyses can be used make informed design decisions then more general guidelines are provided based on the results of the perturbation analyses.

Scenario 1

A UPM machine which can be represented by the model of Figure 2.1 is isolated using passive isolators with $h = 0$, $h_F > 0$, and $r \neq 0$. It is experiencing undesirable residual vibrations due to the motion of its y and z-axes. Parameters ε, ζ_1° and ζ_2° are determined to be 0.7, 0.2 and 0.1, respectively, for the machine. Note that, because $\varepsilon < 1$, Mode 1 is the purely rotational mode and Mode 2 is the purely translational mode at $h = 0$. The machine's parameters place it at the point marked ♦ on Figure 2.7 (a) and Figure 2.8 (a), so $\Gamma_1^\circ - \Gamma_3^\circ > 0$ and $C_{z2} < 0$. From Eq.(2.16), $C_{y1} < 0$, which means that lowering the CG (i.e., $h > 0$) will lead to a reduction in σ^2_{Hy}. Note that σ^2_{Hz} will also be reduced by lowering (or raising) the CG since $h = 0$ is a local maximum of σ^2_{Hz}. Now assume that the machine is re-designed such that ε increases to about 0.99 (for instance by increasing the half-span b of the isolators), while keeping ζ_1° and ζ_2° unchanged. This means that $\Gamma_1^\circ - \Gamma_3^\circ < 0$ and $C_{z2} > 0$, implying that the CG would now have to be raised (i.e., $h < 0$) to reduce σ^2_{Hy}. However, raising the CG will increase σ^2_{Hz} (because it has a local minimum at $h = 0$). Consequently, it may be preferable to keep $h = 0$ for the re-designed machine.

Scenario 2

Let us now assume that the UPM machine in Scenario 1 has ε, ζ_1° and ζ_2° values of 1.1, 0.1 and 0.2, respectively. Note that, since $\varepsilon > 1$, Mode 1 is the purely translational mode and Mode 2 is the purely rotational mode at $h = 0$. Thus the machine can be characterized by the point marked ♦ on Figure 2.7 (b) and Figure 2.8 (b) which has $\Gamma_2^\circ - \Gamma_3^\circ < 0$ and $C_{z2} > 0$. Therefore, lowering the CG will reduce σ^2_{Hy} but will compromise σ^2_{Hz}. However, in this scenario, re-designing the machine by increasing ε, for instance to 1.2, while keeping ζ_1° and ζ_2° unchanged will lead to $\Gamma_2^\circ - \Gamma_3^\circ > 0$ and $C_{z2} < 0$. Consequently, σ^2_{Hy} and σ^2_{Hz} can both be reduced by raising the CG.

Generally, if $h_F > 0$ (as it typically is) and $r \neq 0$, we observe from Figures 2.7 and 2.8 that to simultaneously reduce σ^2_{Hy} and σ^2_{Hz} via mode coupling, the CG should be lowered (i.e., $h > 0$) for $\varepsilon < 1$ and raised (i.e., $h < 0$) for $\varepsilon > 1$. The conditions reverse if $h_F < 0$. Note that the perturbation analyses do not provide any information on how much the CG can be lowered or raised before the residual vibrations begin to increase or the system becomes unstable. Such limits may be determined through simulations or experiments, as will be shown in the following section. However, as shown in this section, the analyses help point the designer in the right direction.

2.4. Simulations and Experiments

The theoretical principles presented in the section above are validated in simulations and experiments using Mori Seiki's NN1000 ultra-precision 5-axis machine tool [72] shown in Figure 2.9. Stemming from a granite base supported on four pneumatic vibration isolators, the machine has its *x* and *C* axes on the workpiece side and its *y*, *z* and *A* axes on the tool side. The machine is symmetrical about its centroidal *x*-*z* and *y*-*z* planes, so the 2-D model presented in this chapter is applicable to both planes. However, because of the relatively small moving mass of the *x*-axis, the residual vibrations in *x*-*z* plane are negligible. Consequently, the simulations and experiments are focused on the *y*-*z* plane of the machine.

2.4.1. Simulation Results

The residual vibrations in the *y*-*z* plane are primarily caused by the motion of the *y*-axis. The *z*-axis can also contribute to the vibrations when it is located, in the worst case, at $r = \pm 70$ mm

(i.e., the maximum stroke of the *y*-axis). For this reason, the contributions of both axes are studied in simulations using the parameters given in Table 2.1, which have been either identified experimentally or obtained from the solid model of the machine.

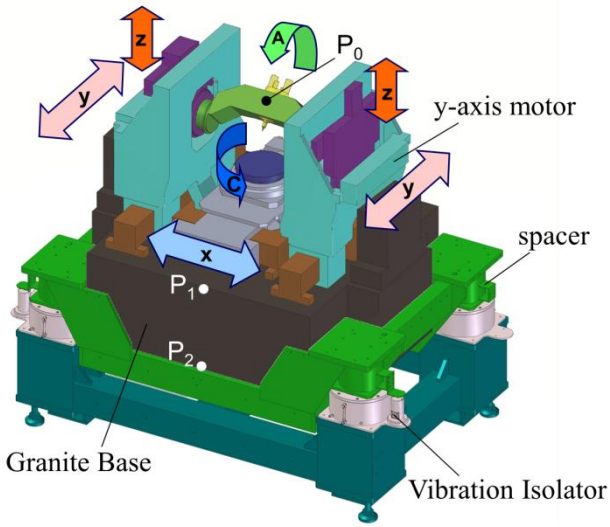

Figure 2.9: Schematic of Mori Seiki's NN1000 DCG 5-Axis Ultra-Precision Machine Tool Used for Simulations and Experiments

Parameter	Value
m [kg]	1,182
I [kgm^2]	96
k_y [N/mm]	880
k_θ [Nm/rad]	104,430
ζ_1°, ζ_2°	0.15
h_F [mm]	435
r [mm]	70

Table 2.1: Key Parameters of NN1000 DCG Used for Simulations

Based on parameters provided in Table 2.1, ρ = 285 mm, $\tilde{h}_F$ = 1.53, $\tilde{r}$ = 0.246 and ε = 1.21. $\tilde{\omega}_{max}$ = 16.75 (i.e., 72.7 Hz) is calculated based on α = 1.005 (see Figure 2.6). Figure 2.10 shows the normalized plots of σ^2_{Hy} and σ^2_{Hz} for $\tilde{h} \in [-1.5, 1.5]$ (i.e. $h \in [-427, 427]$ mm); σ^2_{Hy} has a positive slope while σ^2_{Hz} has a local maximum at h = 0, as predicted from the analysis in Section 2.3. Therefore, raising the CG reduces σ^2_{Hy} and σ^2_{Hz} until their respective local minima of h = −248 mm ($\tilde{h}$ = −0.87) and h = −168 mm ($\tilde{h}$ = −0.59) are reached. The granite base of NN1000 can however not be raised more than 116 mm (using the spacer in Figure 2.9) due to the

overall height restrictions of the machine. Therefore, h = −116 mm is selected as the optimal location of the isolators w.r.t. the CG.

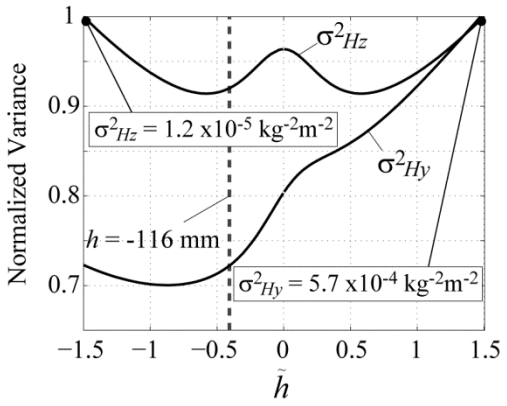

Figure 2.10: Normalized Variances σ^2_{Hy} and σ^2_{Hz} of NN1000 DCG as Functions of Dimensionless Isolator Height $\tilde{h}$

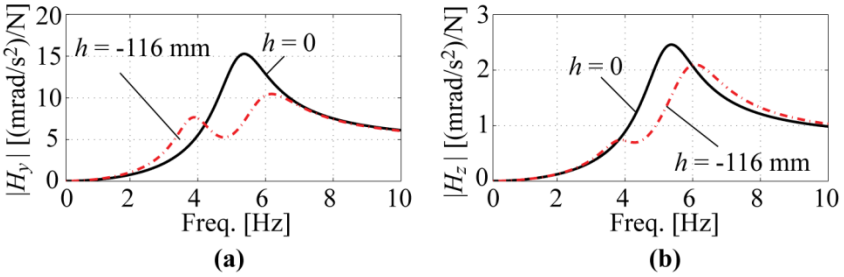

Figure 2.11: Simulated Magnitudes of (a) H_y and (b) H_z for h = 0 and h = −116 mm

Figure 2.11 (a) and (b) respectively show the magnitude plots of H_y and H_z for h = 0 and h = −116 mm. As expected, the areas under the FRFs calculated using the optimal isolator height are smaller than those for h = 0. Notice that, even though the worst case scenario for H_z (i.e., r = ±70 mm) is considered in Figure 2.10, max(σ^2_{Hz}) is about 50 times smaller than max(σ^2_{Hy}). Moreover, the moving mass of the z-axis is only a third of that of the y-axis. Therefore, for the NN1000 machine, the maximum level of residual vibrations caused by the z-axis is significantly less than that caused by the y-axis, for the same acceleration command.

2.4.2. Experimental Results

The vibrations induced by the z-axis could not be measured reliably due to their relatively low levels. Therefore, our experiments are focused on the residual vibrations caused by the y-axis. Figure 2.12 shows the magnitude of H_y measured by applying a swept sine wave excitation signal to the y-axis motor and measuring the net rotational acceleration of the base using four

accelerometers located at the points P_1, P_2 (both indicated on Figure 2.9) and points P_3, P_4 (opposite P_1 and P_2 on the centroidal *y*-*z* plane). As seen, $h = -116$ mm yields a lower variance than $h = 0$, in agreement with the simulations. The slight discrepancies between the simulated and measured FRFs are attributable to approximations in the model, errors in the identified parameters and inaccuracies in the experimental measurement. Figure 2.13 (a) shows the *y*-acceleration of the machine, measured using an accelerometer attached to the point marked P_0 on Figure 2.9, during the motion of the *y*-axis from rest to a speed of 1000 mm/min. As seen, raising the CG reduces the measured residual vibrations significantly, leading to a dramatic five-fold reduction in the RMS position error measured from the *y*-axis encoder, as shown in Figure 2.13 (b).

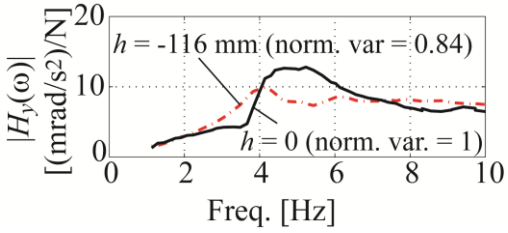

Figure 2.12: Experimentally Measured Magnitude of H_y for $h = 0$ and $h = -116$ mm

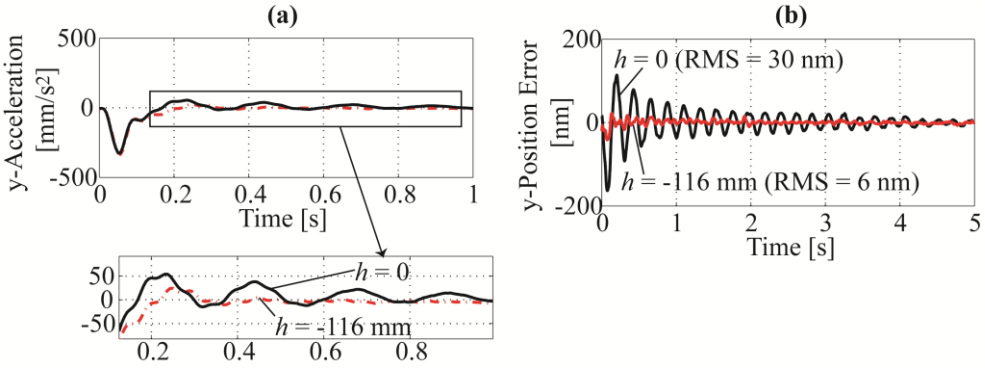

Figure 2.13: (a) Acceleration of Base Measured at Point P_0 (b) Position Error Measured from Encoder for $h = 0$ and $h = -116$ mm during Motion of *y*-Axis from Rest to 1000 mm/min

2.4.3. Remarks Regarding Transmissibility

As mentioned in Chapter 1, the requirement to decouple vibration modes is based on concerns related to transmissibility. However, changing the isolator height does not result in the unwanted coupling of vertical floor vibrations to the horizontal vibrations of the base (i.e., the

transmissibility in the vertical direction is theoretically unaffected) [29]. However, it affects the transmissibility in the horizontal (y) direction, given by the expression

$$H_{tr}(\omega) = \sum_{i=1}^{2} \frac{k_y}{I_{qi}} \frac{(h - h_{Ni})(h_w - h_{Ni})}{-\omega^2 + 2j\omega\zeta_i\omega_{ni} + \omega_{ni}^2}, \tag{2.21}$$

where h_w represents the height of the work surface measured from the CG. Note that the effect of the horizontal damping coefficient is ignored in Eq.(2.21).

Due to lack of test equipment, the transmissibility of the NN1000 machine could not be measured experimentally. However, simulation results (Figure 2.14) using the parameters in Table 2.1 show that the variance of the horizontal transmissibility with respect to the top of the isolated base (h_w = 116 mm) is slightly improved by raising the CG from h = 0 to h = −116 mm. This result is in agreement with the paper [37] which shows that mode coupling can also improve transmissibility compared to decoupling. Moreover, due to the mode shape of the machine, the second resonance peak of the coupled system is virtually eliminated such that high frequency attenuation of the ground motions is also improved by raising the CG [36]. Thus one cannot conclude in a general sense that coupling vibration modes is always detrimental to vibration isolation quality. Also, because of the effect of mode coupling on the isolated system's mode shapes, a mode-coupled system is not subject to the inherent trade-off between residual vibration and transmissibility in the manner observed in single degree-of-freedom systems [26]. An in depth study into the effect of mode coupling on transmissibility is provided in Chapters 3 and 4.

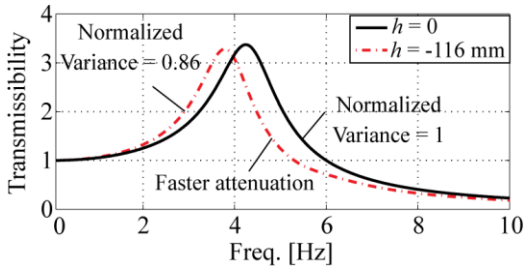

Figure 2.14: Simulated Transmissibility of NN1000 Based on Work Surface Height h_w = 116 mm for h = 0 and h = −116 mm

2.5. Conclusion

This chapter has analyzed mode coupling in a single-variable, modally-damped, planar isolation system, and has shown through eigenvalue analyses that the drastic reductions of

vibration caused by mode coupling are primarily linked to critical configurations created by curve veering and mode localization. It has also used perturbation analyses to show that coupling the vibration modes of a passively isolated machine by judiciously locating its isolators more often than not provides conditions that lead to the reduction of residual vibration compared to the recommended practice of decoupling. The practical design guidelines that have been obtained from the theoretical analyses presented in this chapter are successfully used in simulations/experiments to achieve a five-fold reduction in the dominant residual vibration of an ultra-precision machine tool, without sacrificing vibration isolation quality.

CHAPTER 3
REDUCTION OF VIBRATIONS OF PASSIVELY-ISOLATED ULTRA-PRECISION MANUFACTURING MACHINES USING MODE COUPLING

3.1. Introduction

Chapter 2 has shown that, when modally coupled, small changes in the isolator location of a UPM machine can cause large variations in its mode shapes, leading to drastic changes in its vibration response due to curve veering and mode localization. In studying curve veering and mode localization, it is customary to ignore the effects of damping [73-75] or to assume modal damping [76]. However, the response of a non-proportionally damped system under coupling can be quite different from an undamped or modally damped system, as recently demonstrated by Vijayan and Woodhouse [77]. (Balmes [76] also alludes to this fact).

The analyses of the effects of mode coupling on the residual vibration of passively-isolated UPM machines presented in Chapter 2 [1] was based on the simplifying assumption of modal damping. Moreover, the study in Chapter 2 did not analyze the effects of mode coupling on transmissibility. Therefore, building on some preliminary work by the author [78,79], the goals of this chapter are to: (1) characterize the effects of mode coupling on the residual vibration and transmissibility of a non-proportionally damped UPM machine – which is more realistic than modal damping; and (2) provide design guidelines for properly exploiting mode coupling for the reduction of residual vibration and transmissibility.

The rest of this chapter is organized as follows. Section 3.2 presents a planar model of a passively-isolated machine, having non-proportional (NP) damping, and proposes frequency response functions (FRFs) for assessing the machine's residual vibration and transmissibility. A perturbation method is used in Sections 3.3 to study the gradient or curvature of the H_∞/H_2 norms of the residual vibration and transmissibility FRFs, respectively, subject to mode coupling. The

magnitude and direction of the gradients are used to deduce conditions under which mode coupling is most advantageous relative to decoupling, and the effects of NP damping on the results are highlighted. Section 3.4 provides practical design guidelines for judiciously placing vibration isolators to achieve reductions of residual vibration and transmissibility using mode coupling. In Section 3.5, the simulation and experimental studies conducted on a 5-axis ultra-precision milling machine in Chapter 2 are re-evaluated based on the NP damping analysis presented in this chapter. Simulations and experiments are also carried out using a prototype UPM machine to further demonstrate the benefits and limitations of the analyses presented in this chapter. Finally, conclusions are presented in Section 3.6

3.2. Machine Model and Frequency Response Functions for Analyzing Vibration

3.2.1. Machine Model

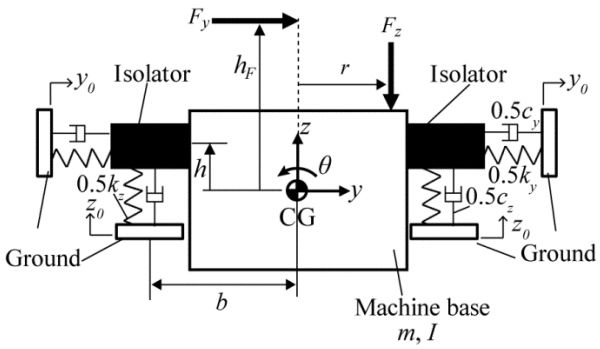

Figure 3.1: Planar Model of an Isolated Machine with Damping

Figure 3.1 shows a 2-D model of an isolated machine; m and I are respectively the mass and centroidal moment of inertia of the machine base about the x-axis; k_y, k_z and c_y, c_z are the collective stiffness and damping constants of the passive isolators in the y and z directions, respectively; b is the half-span of the isolators while h is the vertical height of the isolator mounting point, measured from the center of gravity (CG) of the base. The vibrations of the machine base are assumed to occur only in the y-z plane. Such planar analyses can be applied, for instance, when the machine's structure and loading are symmetrical in a specific direction (in this case, the x-direction). In general, the dynamics of passive (typically pneumatic) isolators is nonlinear [40,59]. However, for small vibratory motions, linear models are adequate [40].

Let F_y and F_z (shown in Figure 3.1) represent onboard disturbance forces applied at distances h_F and r, respectively, from the machine's CG, and let y_0 and z_0 represent the horizontal and vertical displacements of the ground. The equation of motion of the isolated base is given by

$$\mathbf{M}\ddot{\mathbf{u}} + \mathbf{C}\dot{\mathbf{u}} + \mathbf{K}\mathbf{u} = \mathbf{F} + \mathbf{C}\dot{\mathbf{u}}_\mathbf{0} + \mathbf{K}\mathbf{u}_\mathbf{0}, \tag{3.1}$$

where **M**, **C, K** are respectively the mass, damping and stiffness matrices, while **u**, $\mathbf{u_0}$ and **F** are respectively vectors of generalized base displacements, ground displacements and forces of the system. They are given by

$$\begin{gathered}\mathbf{M} = \begin{bmatrix} m & 0 & 0 \\ 0 & m & 0 \\ 0 & 0 & I \end{bmatrix},\ \mathbf{C} = \begin{bmatrix} c_y & 0 & -c_y h \\ 0 & c_z & 0 \\ -c_y h & 0 & c_\theta + c_y h^2 \end{bmatrix},\ \mathbf{K} = \begin{bmatrix} k_y & 0 & -k_y h \\ 0 & k_z & 0 \\ -k_y h & 0 & k_\theta + k_y h^2 \end{bmatrix}, \\ \mathbf{u} = \begin{Bmatrix} y \\ z \\ \theta \end{Bmatrix},\ \mathbf{u_0} = \begin{Bmatrix} y_0 \\ z_0 \\ 0 \end{Bmatrix},\ \mathbf{F} = \begin{bmatrix} 1 & 0 \\ 0 & -1 \\ -h_F & -r \end{bmatrix} \begin{bmatrix} F_y \\ F_z \end{bmatrix},\end{gathered} \tag{3.2}$$

with $k_\theta = b^2 k_z$ and $c_\theta = b^2 c_z$. Note that the system's damping is explicitly considered in Eq.(3.1), unlike in Eq.(2.1) (Chapter 2) where the damping was ignored. As can be inferred from Eq. (3.2), only the dynamics in the y and θ directions are coupled as a result of h. Therefore, the effects of h on the dynamics of the isolated system can be studied by focusing on the coupled subsystem

$$\begin{gathered}\mathbf{M} = \begin{bmatrix} m & 0 \\ 0 & I \end{bmatrix},\ \mathbf{C} = \begin{bmatrix} c_y & -c_y h \\ -c_y h & c_\theta + c_y h^2 \end{bmatrix},\ \mathbf{K} = \begin{bmatrix} k_y & -k_y h \\ -k_y h & k_\theta + k_y h^2 \end{bmatrix}, \\ \mathbf{u} = \begin{Bmatrix} y \\ \theta \end{Bmatrix}, \mathbf{u_0} = \begin{Bmatrix} y_0 \\ 0 \end{Bmatrix},\ \mathbf{F} = \begin{bmatrix} 1 & 0 \\ -h_F & -r \end{bmatrix} \begin{bmatrix} F_y \\ F_z \end{bmatrix}.\end{gathered} \tag{3.3}$$

Equation (3.3) gives rise to two vibration modes, described by the coordinates y and θ, which are coupled by non-zero values of h. The effect of this coupled dynamics on residual vibration and transmissibility is the subject of the rest of the chapter.

3.2.2. FRFs for Residual Vibrations

Residual vibration is transient in nature; it occurs freely after F_y or F_z is applied then removed, and is typically quantified using time domain characteristics like settling time and maximum overshoot [71,80]. However, frequency domain metrics, based on steady state

assumptions, often correlate closely with time domain characteristics [69,71], while being more convenient for analysis. Therefore, in this chapter, residual vibration is quantified using FRFs.

Let us consider the effects of F_y and F_z on residual vibration separately. When F_y is applied to the machine, it generates responses in the y and θ directions. Our previous analysis in Chapter 2 was focused on the θ response (or rocking vibration) because it often dominates the residual vibration dynamics of UPM machines [13,14]. However, in this chapter, we take a more general approach by considering both responses using the equation

$$H_{Fy}(\omega) = \max_{\omega} \left\{ \left| H_{y,Fy}(\omega) \right|, w \left| H_{\theta,Fy}(\omega) \right| \right\}, \tag{3.4}$$

where the variable ω represents dimensionless excitation frequencies and w is a user-defined weighting factor having the dimension of length, while $H_{y,Fy}$ and $H_{\theta,Fy}$ are respectively the FRFs from force input F_y to the y and θ accelerations of the machine base. Note that, for a decoupled machine, the weighting factor w can be viewed as the absolute value of the height of a specific vibration-sensitive point above or below the CG. In practice, such a point could be a sensor, workpiece or tool location, depending on the application. Without loss of generality, w = 1 m is assumed in the rest of this chapter.

The FRFs $H_{y,Fy}$ and $H_{\theta,Fy}$ of Eq.(3.4) can be expressed as

$$H_{y,Fy}(\omega) = \frac{\ddot{y}}{F_y} = \frac{1}{m} \sum_{i=1}^{2} \left(A_{yi} X_i - B_{yi} \right) h_{Ni}, \tag{3.5}$$

$$H_{\theta,Fy}(\omega) = \frac{\ddot{\theta}}{F_y} = \frac{1}{m\rho} \sum_{i=1}^{2} \left(A_{yi} X_i - B_{yi} \right), \tag{3.6}$$

where ρ is the centroidal radius of gyration of the isolated machine, while A_{yi}, B_{yi} and X_i are dimensionless functions pertaining to each mode i (i = 1, 2). They are given by

$$\begin{aligned} A_{yi} &= \frac{\tilde{h}_F - h_{Ni}}{I_{qi}}, \quad X_i = \frac{\omega^2}{-\omega^2 + 2j\omega\zeta_y\omega_{ni}^2 + \omega_{ni}^2}, \\ B_{yi} &= \frac{X_i}{I_{qi}} \frac{2j\varepsilon\beta\omega \left(A_{y1}X_1 + A_{y2}X_2 \right)}{2j\varepsilon\beta\omega \left(X_1/I_{q1} + X_2/I_{q2} \right) + \omega^2}, \end{aligned} \tag{3.7}$$

where j is the unit imaginary number and $\tilde{h}_F = h_F/\rho$ is the dimensionless forcing location of F_y, while ω_{ni}, h_{Ni} and I_{qi} respectively denote the dimensionless natural frequency, node height and modal inertia of each vibration mode i; their definitions have been provided in Chapter 2, the

only difference being that the ~ accent used in Chapter 2 has been omitted here (except when absolutely needed) to help simplify the notation. The variable β is given by

$$\beta = \zeta_\theta - \varepsilon\zeta_y, \tag{3.8}$$

where

$$\zeta_y = \frac{c_y}{2\sqrt{k_y m}},\ \zeta_\theta = \frac{c_\theta}{2\sqrt{k_\theta I}},\ \varepsilon = \sqrt{\frac{k_\theta}{I}\frac{m}{k_y}}. \tag{3.9}$$

Similarly, the influence of F_z on residual vibration can be characterized by accelerations in the z and θ directions (for $r \neq 0$). However, as mentioned in Section 3.2.1, the motions in the z direction are not of interest in this study because they are unaffected by h. Therefore, the residual vibration FRF in the θ direction is suitably described by

$$H_{Fz}(\omega) = \frac{\ddot{\theta}}{F_z} = \frac{1}{m\rho}\sum_{i=1}^{2}\left(A_{zi}X_i - B_{zi}\right), \tag{3.10}$$

where X_i is defined in Eq.(3.7), while A_{zi} and B_{zi} are expressed as

$$A_{zi} = \frac{\tilde{r}}{I_{qi}},\ \ B_{zi} = \frac{X_i}{I_{qi}}\frac{2j\varepsilon\beta\omega\left(A_{z1}X_1 + A_{z2}X_2\right)}{2j\varepsilon\beta\omega\left(X_1/I_{q1} + X_2/I_{q2}\right) + \omega^2}, \tag{3.11}$$

with $\tilde{r} = r/\rho$ representing the dimensionless version of r.

3.2.3. FRFs for Transmissibility

It was mentioned in Chapters 1 and 2 that the requirement to decouple vibration modes in UPM machines was based on concerns related to transmissibility. The key reason being that coupling could make vertical ground motions to be transmitted to the typically more-sensitive horizontal axes of the machine [14,29]. While this observation is generally true about coupling, it is not an issue if coupling is achieved by changing h, because the vertical motion is not coupled by h. In other words, transmissibility in the vertical direction is theoretically unaffected by changing h [29]. Therefore, we focus our attention on transmissibility in the horizontal direction. Specifically, we consider transmissibility between input y_0 and output y_w, the horizontal motion at height h_w measured vertically from the CG (similar to h_F in Figure 3.1). It is given by the expression

$$H_{tr}(\omega)=\frac{y_w}{y_0}=\sum_{i=1}^{2}\left(A_{tri}X_{tri}-B_{tri}\right)\left(h_{Ni}-\tilde{h}_w\right), \tag{3.12}$$

where h_w (or its dimensionless form $\tilde{h}_w = h_w/\rho$) represents the height of a sensitive location on the machine base. It could be, for instance, the location of the workpiece; A_{tri}, B_{tri} and X_{tri} are defined as

$$\begin{aligned} A_{tri}&=\frac{h_{Ni}-\tilde{h}}{I_{qi}}, \quad X_{tri}=\frac{1+2j\zeta_y\omega}{-\omega^2+2j\omega\zeta_y\omega_{ni}^2+\omega_{ni}^2}, \\ B_{tri}&=\frac{X_i}{I_{qi}}\frac{2j\varepsilon\beta\omega\left(A_{tr1}X_1+A_{tr2}X_2\right)}{2j\varepsilon\beta\omega\left(X_1/I_{q1}+X_2/I_{q2}\right)+1}, \end{aligned} \tag{3.13}$$

where $\tilde{h} = h/\rho$ is the dimensionless isolator height.

It is important, at this juncture, to explain the important role β defined in Eq.(3.8) plays in the dynamics of the isolated system with NP damping. The decoupled system (with h = 0) is always proportionally damped because each motion direction acts independently [60]; however, the coupled system can be proportionally or non-proportionally damped depending on the value of β. If β = 0, the B terms in Eqs.(3.5), (3.6), (3.10) and (3.12) equal zero, so the coupled system dynamics is proportionally damped, making it suitable for the modal damping assumption employed in Chapter 2. For β to be zero, the relationship $\zeta_\theta/\zeta_y = \varepsilon$ must be satisfied, which is scarcely achieved in practice. In most cases, therefore, $\beta \neq 0$ so the system dynamics is non-proportionally damped. The implication is that, as the system is coupled by changing h, it transitions suddenly from proportional to NP damping. At the same time, ω_{ni}, h_{Ni} and I_{qi} experience drastic changes linked to curve veering and mode localization, as discussed in Chapter 2. The next section explores how these different changes combine together to influence the residual vibration and transmissibility of the coupled system compared to the decoupled.

3.3. Analysis of Residual Vibration and Transmissibility of Mode-Coupled UPM Machines

The steady state responses of vibrating systems are often quantified in frequency domain using either H_2 or H_∞ norms of FRFs [53,70]. A system's H_2 norm is a measure of the energy of its response to stationary random excitations. It is thus well suited for quantifying the effect of the transmissibility of a UPM machine over a wide band of frequencies [30,54]. The H_∞ norm is

its worst case steady-state response to sinusoidal inputs. It is represented by the peak magnitude of the FRF. Both norms are useful indicators of the system's response to transient vibrations [69]. In Chapter 2, the output variance (which at its limit is equivalent to the H_2 norm [53]) was adopted as a measure of the system's residual vibration response because it permits the effects of all resonance modes in an FRF to be captured. However, the output variance is sensitive to the anti-resonances as well as the frequency limits of the FRF, which are often not key contributors to the system's transient response. Therefore, for quantifying residual vibration in this chapter, the H_∞ norm is preferred because it focuses on the highest resonance peak in the FRF, which often correlates well with the dominant frequency in the transient vibration response. In this section, the H_∞ norms of the residual vibration FRFs and output variance of the transmissibility FRF are analyzed using a perturbation technique to understand the effects mode coupling on UPM machines with NP damping

3.3.1. Residual Vibration

The H_∞ norm of residual vibration due to F_y (i.e., H_{Fy} defined in Eq.(3.4)) is expressed as

$$\left\|H_{Fy}\right\|_\infty = \max\left(\left|H_{y,Fy}\left(\omega_y\right)\right|, w\left|H_{\theta,Fy}\left(\omega_\theta\right)\right|\right), \tag{3.14}$$

where ω_y and ω_θ are the respective resonance frequencies of $H_{y,Fy}$ and $H_{\theta,Fy}$. At h = 0, they are given by

$$\omega_y = \frac{1}{\sqrt{1-2\zeta_y^2}}, \quad \omega_\theta = \frac{\varepsilon}{\sqrt{1-2\zeta_\theta^2}}. \tag{3.15}$$

The effect of mode coupling on $||H_{Fy}||_\infty$ by evaluating the first-order Taylor expansion of $|H_{y,Fy}(\omega_y)|$ and $|H_{\theta,Fy}(\omega_\theta)|$ about h = 0 is investigated; i.e.,

$$\left|H_{y,Fy}\left(\omega_y\right)\right| \cong C_{y,Fy}\left(1+T_y\tilde{h}\right), \tag{3.16}$$

and

$$\left|H_{\theta,Fy}\left(\omega_\theta\right)\right| \cong C_{\theta,Fy}\left(1+T_\theta\tilde{h}\right), \tag{3.17}$$

where $C_{y,Fy}$ and $C_{\theta,Fy}$ represent the values of $|H_{y,Fy}(\omega_y)|$ and $|H_{\theta,Fy}(\omega_\theta)|$ at h = 0. They are given by

$$C_{y,Fy} = \frac{1}{m}\frac{1}{2\zeta_y\sqrt{1-\zeta_y^2}}, \quad C_{\theta,Fy} = \frac{1}{m\rho}\frac{\left|\tilde{h}_F\right|}{2\zeta_\theta\sqrt{1-\zeta_\theta^2}}. \tag{3.18}$$

T_y and T_θ are the corresponding gradients at $h = 0$ expressed as

$$T_y = \frac{-\tilde{h}_F\left(\varepsilon^2 + \left(4\varepsilon\zeta_y\zeta_\theta - 1\right)\omega_y{}^2\right)}{\left(\left(\varepsilon^2 - \omega_y{}^2\right)^2 + 4\omega_y{}^2\varepsilon^2\zeta_\theta^2\right)},\quad T_\theta = \frac{-\left(1 + \left(4\zeta_y^2 - 1\right)\omega_\theta{}^2\right)}{\tilde{h}_F\left(\left(1 - \omega_\theta{}^2\right)^2 + 4\omega_\theta{}^2\zeta_y^2\right)}. \tag{3.19}$$

The dominant peak of $|H_{Fy}|$ (i.e., $\|H_{Fy}\|_\infty$) at $h = 0$ is determined by evaluating the ratio $wC_{\theta,Fy}/C_{y,Fy}$; i.e.,

$$\frac{wC_{\theta,Fy}}{C_{y,Fy}} = \left|\frac{wh_F}{\rho^2}\right|\frac{\zeta_y\sqrt{1-\zeta_y{}^2}}{\zeta_\theta\sqrt{1-\zeta_\theta{}^2}}. \tag{3.20}$$

If the ratio is greater than unity, the rocking vibration dominates the response of the decoupled system and $|H_{\theta,Fy}(\omega_\theta)|$ should be the focus of the analysis. Otherwise, the translatory vibration is dominant and the analysis is focused on $|H_{y,Fy}(\omega_y)|$. From Eq.(3.20), one observes that the rocking vibration dominates when ζ_θ is small relative to ζ_y or h_F is large relative to ρ^2 (for a given w).

The gradients, T_y and T_θ, provide useful hints about the effects of small perturbations of h (from $h = 0$) on the dominant residual vibration response of the coupled system. In mode localization literature, coupling with small values of h is referred to as "weak coupling" [74,81]. The magnitude of the gradient indicates the sensitivity of the decoupled system to weak coupling while its direction shows whether residual vibration can be expected to increase or decrease due to weak coupling.

The direction of each gradient can be determined by solving for the values of ε where the gradient crosses zero. They are given by

$$\varepsilon = \begin{cases} \dfrac{\sqrt{1-2\zeta_y^2+4\zeta_y^2\zeta_\theta^2}-2\zeta_y\zeta_\theta}{1-2\zeta_y^2} & \text{for } T_y = 0 \\ \dfrac{\sqrt{1-2\zeta_\theta^2}}{\sqrt{1-4\zeta_y^2}} & \text{for } T_\theta = 0 \end{cases}. \tag{3.21}$$

Figure 3.2 (a) and (b) provide graphical depictions of Eq.(3.21) for various values of ε as functions ζ_y and ζ_θ between 0 and 0.5. In Figure 3.2 (and the rest of this chapter) it is assumed that $h_F > 0$ because it is common in practice to have moving masses above the CG of the machine. However, please keep in mind that if $h_F < 0$, the signs of T_y and T_θ must be reversed in

the ensuing discussions. Observe that when $\varepsilon < 1$, $T_y > 0$ and $T_\theta < 0$ for most combinations of ζ_y and ζ_θ. Conversely, when $\varepsilon > 1$, $T_y < 0$ and $T_\theta > 0$ under most scenarios. The implication of these observations on isolation system design is discussed in Section 3.4.

Figure 3.3 (a) and (b) show the T_y and T_θ plots for the modally damped system, with ζ_1 and ζ_2 representing the modal damping ratios of the lower and higher frequency modes, respectively. When $\varepsilon < 1$, ζ_1 and ζ_2 correspond to ζ_θ and ζ_y, respectively; the opposite is true for $\varepsilon > 1$. As can be seen from the plots, the general conclusions reached for the NP damped system apply to the modally damped system. The behavior of the signs of T_y and T_θ are consistent with the changes in the system's mode shapes as the system transitions from $\varepsilon < 1$ to $\varepsilon > 1$ (see h_{Ni} plot and detailed discussion in Section 2.2.2). Notice, however, that the pattern of the contours in Figure 3.3 is different from those in Figure 3.2 due to the effect of NP damping.

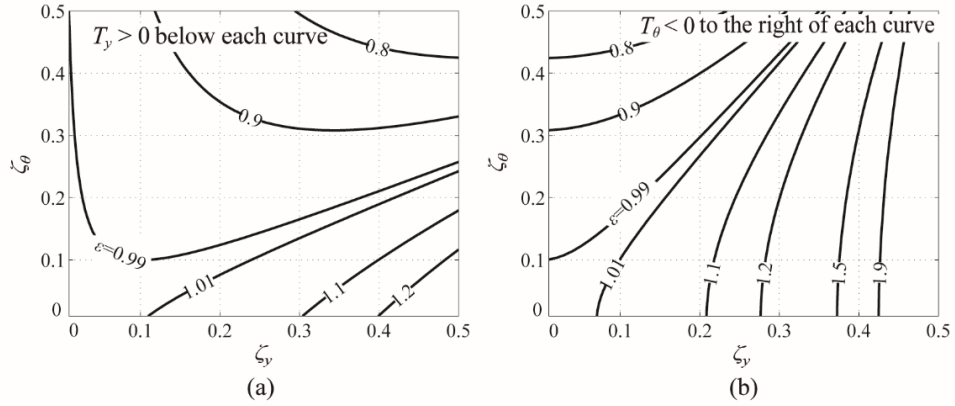

Figure 3.2: Contour Plots of (a) $T_y = 0$ (b) $T_\theta = 0$ of NP Damped System as Functions of ζ_y and ζ_θ for Various Values of ε ($h_F > 0$ is assumed)

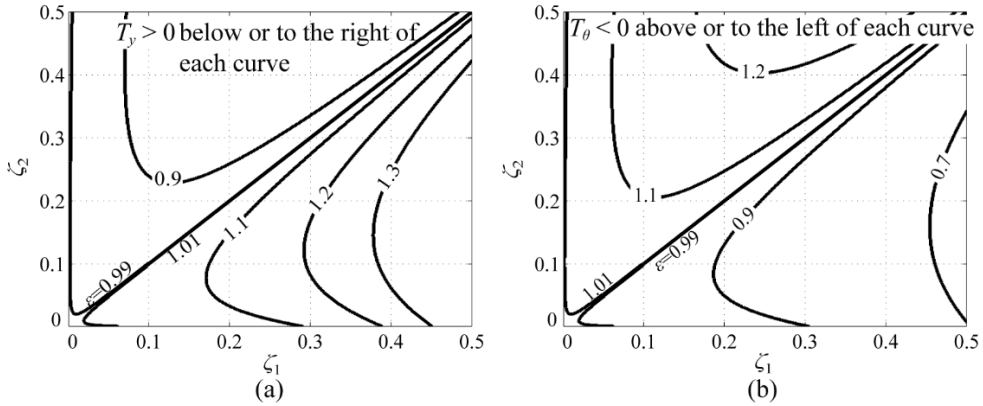

Figure 3.3: Contour Plots of (a) $T_y = 0$ (b) $T_\theta = 0$ of Modally Damped System as Functions of ζ_1 and ζ_2 for Various Values of ε ($h_F > 0$ is assumed)

The magnitude of the gradient is an indicator of how sensitive the residual vibration magnitude of the decoupled system is to weak coupling. It is helpful to know the conditions for maximum sensitivity in order to more fully exploit the beneficial effects of mode coupling in design. If modal damping is assumed, the gradients of T_y and T_θ have their highest magnitude (which tends to infinity) as $\varepsilon \to 1$. It corresponds to the condition of maximal sensitivity of the system's mode shapes due to mode coupling in Chapter 2 [1]. However, when NP damping is considered, the transition of system's mode shapes from real to complex gives rise to very different conditions for maximum sensitivity to mode coupling. Let ε^*_y and ε^*_θ denote the ε values where the respective magnitudes of T_y and T_θ are highest; i.e.,

$$\left.\frac{dT_y}{d\varepsilon}\right|_{\varepsilon=\varepsilon^*_y} = 0, \quad \left.\frac{dT_\theta}{d\varepsilon}\right|_{\varepsilon=\varepsilon^*_\theta} = 0. \tag{3.22}$$

Obtaining ε^*_y from Eq.(3.22) requires the determination of the roots of a fifth order polynomial,

$$\begin{aligned} &\varepsilon^5 + a_4\varepsilon^4 + a_3\varepsilon^3 + a_2\varepsilon^2 + a_1\varepsilon + a_0\Big|_{\varepsilon=\varepsilon^*_y} = 0; \\ &a_4 \triangleq 6\omega_y{}^2\zeta_y\zeta_\theta,\ a_3 \triangleq -2\omega_y{}^2,\ a_2 \triangleq 4\omega_y{}^4\zeta_\theta\left(-1+2\zeta_\theta^2\right)\zeta_y, \\ &a_1 \triangleq \omega_y{}^4\left(1-4\zeta_\theta^2\right),\ \ a_0 \triangleq -2\omega_y{}^6\zeta_y\zeta_\theta. \end{aligned} \tag{3.23}$$

Figure 3.4 (a) shows a sampling of the positive real values of ε^*_y obtained by solving Eq.(3.23) numerically for ζ_y and ζ_θ values ranging from 0 to 0.5. Each root is tested numerically to ensure that it results in a local maximum. As seen, there is a wide range of ε values that give rise to maximum sensitivity in $|H_{y,Fy}(\omega_y)|$ due to weak coupling. Solving for ε^*_θ from Eq.(3.22) yields two real roots which can be obtained in closed-form as

$$\varepsilon^*_\theta = \frac{\sqrt{1-2\zeta_\theta^2}}{\sqrt{1\pm 2\zeta_y}}. \tag{3.24}$$

Both roots result in local maxima in $|T_\theta|$. Figure 3.4 (b) shows various values of ε^*_θ as functions of the damping ratios ζ_y and ζ_θ. We observe that the smaller value of ε^*_θ in Eq.(3.24) always yields a negative value for T_θ while the larger value results in positive T_θ. Also, the smaller ε^*_θ always results in a larger magnitude of $|T_\theta|$ than the larger ε^*_θ. Notice from Eq.(3.24) that, for non-zero damping ratios, $\varepsilon^*_\theta = 1$ only when $\zeta_\theta = \sqrt{\zeta_y}$. One can therefore conclude that, because of NP damping, the coupled system has finite sensitivities to mode coupling and that the maximum

sensitivity does not necessarily occur as $\varepsilon \to 1$, where the mode shapes of the modally damped system are most sensitive.

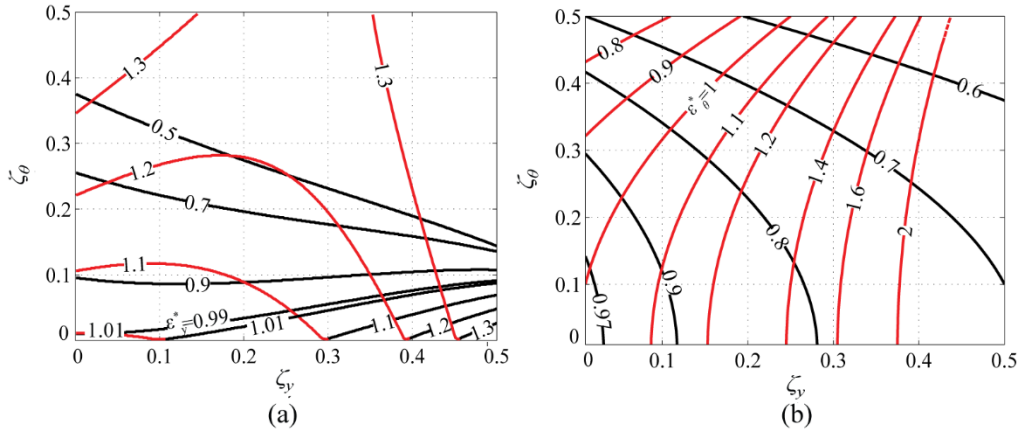

Figure 3.4: Contour Plots of (a) ε^*_y and (b) ε^*_θ as Functions of ζ_y and ζ_θ. The Red and Black Line Colors are Used to Differentiate Each of the Two (positive real) Roots of Eq.(3.22). All Roots of Eq.(3.22) Correspond to Local Maxima in $|T_y|$ or $|T_\theta|$

Considering residual vibration due to F_z, the H_∞ norm of H_{Fz} is given by

$$\left\|H_{Fz}\right\|_\infty = \left|H_{\theta,Fz}\left(\omega_\theta\right)\right|, \tag{3.25}$$

where ω_θ is the resonance frequency defined in Eq.(3.15) for $h = 0$. A second-order Taylor expansion is needed to evaluate $\|H_{Fz}\|_\infty$ because the gradient term in its first-order expansion is always zero, meaning that it always has a stationary point at $h = 0$ (as was also observed in Chapter 2 for the modally damped system). Evaluating the second-order Taylor expansion of $\|H_{Fz}\|_\infty$ about $h = 0$, we get

$$\left|H_{Fz}\left(\omega_\theta\right)\right| \cong C_{Fz}\left(1+\frac{1}{2}T_z\tilde{h}^2\right), \tag{3.26}$$

The value of $\|H_{Fz}\|_\infty$ at $h = 0$, C_{Fz}, is given by

$$C_{Fz} = \frac{1}{m\rho}\frac{\left|\tilde{r}\right|}{2\zeta_\theta\sqrt{1-\zeta_\theta^2}}, \tag{3.27}$$

where T_z represents the curvature at $h = 0$ expressed as

$$T_z = \frac{-2\omega_\theta{}^2\left[\left(4\varepsilon\zeta_\theta\zeta_y - 1 + 4\zeta_y{}^2\right)\omega_\theta{}^4 + \left(1+\varepsilon^2-4\varepsilon^2\zeta_y{}^2\right)\omega_\theta{}^2 - \varepsilon^2\right]}{\left[\omega_\theta{}^4 - 2\left(1-2\zeta_\theta{}^2\right)\varepsilon^2\omega_\theta{}^2 + \varepsilon^4\right]\left[\omega_\theta{}^4 - 2\left(1-2\zeta_y{}^2\right)\omega_\theta{}^2 + 1\right]}. \tag{3.28}$$

The nature of the stationary point (i.e., local maximum/minimum or inflection point) at $h = 0$ is determined by numerically evaluating the sign of T_z for various combinations of ζ_y, ζ_θ and ε. Note that $\tilde{r}$ has no influence on T_z. Figure 3.5 shows the contour plot of $T_z = 0$ for various values of ε. Notice that T_z is negative for most combinations of ε, ζ_y and ζ_θ, meaning that $h = 0$ is most often a local maximum of $\|H_{Fz}\|_\infty$. The implication is that (weak) coupling of vibration modes by raising or lowering the isolators w.r.t. the CG is more often better than decoupling, in terms of reducing residual vibration caused by F_z. The same conclusion was reached in the analysis presented in Chapter 2. However, much like the case of $\|H_{Fy}\|_\infty$ discussed above, it can be observed that NP damping changes the pattern of the curves significantly compared to the modally damped case. Figure 3.6 (a) and (b) show the T_z plots for the modally damped system when $\varepsilon < 1$ and $\varepsilon > 1$; ζ_1 and ζ_2 are the same as described in the context of Figure 3.3.

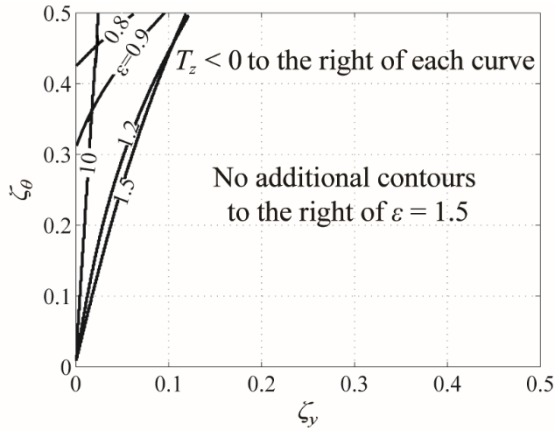

Figure 3.5: Contour Plot of $T_z = 0$ of NP Damped System as Functions of ζ_y and ζ_θ for Various Values of ε

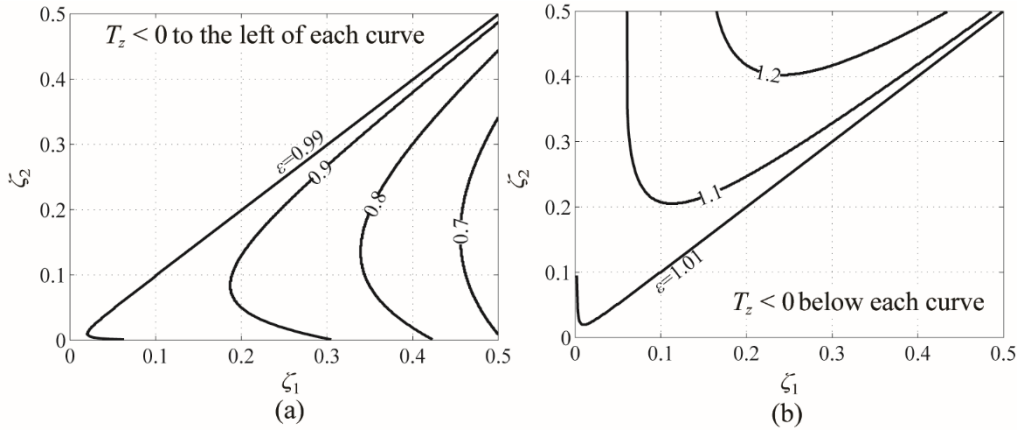

Figure 3.6: Contour Plots of $T_z = 0$ of Modally Damped System as Functions of ζ_1 and ζ_2 for Various Values of (a) $\varepsilon < 1$ (b) $\varepsilon > 1$

To characterize the sensitivity of the system with NP damping to mode coupling, we determine ε^*_z, the ε values where the magnitude of T_z is highest, by solving the equation

$$\left.\frac{dT_z}{d\varepsilon}\right|_{\varepsilon=\varepsilon^*_z} = 0, \tag{3.29}$$

and selecting the solutions that yield local maxima in $|T_z|$. Obtaining ε^*_z from Eq.(3.29) requires the determination of the roots of a fifth order polynomial,

$$\begin{aligned}
&a_5\varepsilon^5 + a_4\varepsilon^4 + a_3\varepsilon^3 + a_2\varepsilon^2 + a_1\varepsilon + a_0\Big|_{\varepsilon=\varepsilon^*_z} = 0;\\
&a_5 \triangleq \zeta_y,\ \ a_4 \triangleq -\zeta_\theta\left(1-4\zeta_y^2\right),\ \ a_3 \triangleq 2\zeta_y\left(1-2\zeta_\theta^2\right)\left(1-2\zeta_y^2\right),\\
&a_2 \triangleq 2\zeta_\theta\left(1-2\zeta_\theta^2\right),\ \ a_1 \triangleq -3\zeta_y\left(1-2\zeta_\theta^2\right)^2,\ \ a_0 \triangleq -\zeta_\theta\left(1-2\zeta_\theta^2\right)^2.
\end{aligned} \tag{3.30}$$

Figure 3.7 shows a sampling of the positive real values of ε^*_z (that yield local maxima) obtained by solving Eq.(3.30) numerically for ζ_y and ζ_θ values ranging from 0 to 0.5. Again, we see that the maximum sensitivity to coupling does not necessarily occur as $\varepsilon \to 1$, where the modally damped system is most sensitive.

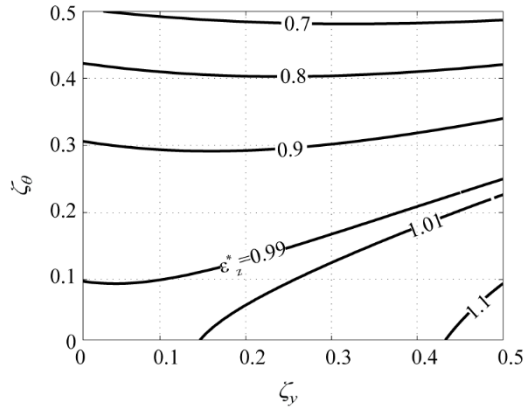

Figure 3.7: Contour Plot of ε^*_z as Functions of ζ_y and ζ_θ, Obtained by Selecting the Positive Real Roots of Eq.(3.29) that Yield Local Maxima in $|T_z|$

3.3.2. Transmissibility

The output variance (or simply variance) of transmissibility FRF H_{tr} to a zero-mean white noise input of unit magnitude is given by [54]

$$\sigma_H^2 = \int_0^{\omega_{max}} \left|H_{tr}(\omega)\right|^2 d\omega. \tag{3.31}$$

The integration limit ω_{max} is usually set to infinity. However, if the system's input is known, ω_{max} can be taken as the highest frequency of its spectrum. The effect of weak coupling on transmissibility can be studied by analyzing the first-order Taylor expansion of σ^2_H about $h = 0$, given by the expression

$$\sigma_H^2 \cong C_{tr}\left(1+T_{tr}\tilde{h}\right), \tag{3.32}$$

where C_{tr} and T_{tr} represent the value and gradient of σ^2_H at $h = 0$, respectively. They are defined as

$$C_{tr} = \int_0^{\omega_{max}} \left|\mathrm{I}_0\right|^2 d\omega, \quad T_{tr} = \frac{2\tilde{h}_w}{C_{tr}} \int_0^{\omega_{max}} \mathrm{I}_1 \cdot \left|\mathrm{I}_0\right|^2 d\omega, \tag{3.33}$$

where I_0 and I_1 are given by

$$\mathrm{I}_0 = \frac{1+ j2\zeta_y\omega}{1-\omega^2 + j2\zeta_y\omega}, \quad \mathrm{I}_1 = \frac{\omega^2\left(\omega^2-\varepsilon^2\right)}{\left[\left(\omega^2-\varepsilon^2\right)^2 + \left(2\beta\varepsilon\omega + 2\varepsilon^2\omega\zeta_y\right)^2\right]}. \tag{3.34}$$

It is very challenging to calculate the integral for T_{tr} in Eq.(3.33) analytically; therefore, it is evaluated numerically. To approximate the integration limit of infinity, $\omega_{max} = 100$ is selected – i.e., 100 times the horizontal natural frequency of the decoupled system (please see definition of dimensionless ω in Chapter 2). The direction of the gradient is determined by numerically solving for the values of ε where each gradient crosses zero, using values of ζ_y and ζ_θ over the interval [0.01, 0.5]. The analysis reveals that T_{tr} is always positive when $\varepsilon < 1$. For $\varepsilon > 1$, the sign of T_{tr} can be determined from Figure 3.8. The ε value (i.e., ε^*_{tr}) corresponding to the maximum sensitivity of T_{tr} is obtained by investigating the roots of the equation

$$\left.\frac{dT_{tr}}{d\varepsilon}\right|_{\varepsilon=\varepsilon^*_{tr}} = 0, \tag{3.35}$$

which requires the following equation to be satisfied

$$\left.\int_0^{\omega_{max}} \mathrm{I}_2 \cdot \left|\mathrm{I}_0\right|^2 d\omega\right|_{\varepsilon=\varepsilon^*_{tr}} = 0, \tag{3.36}$$

where I_2 is given by

$$\mathrm{I}_2 = \frac{2\varepsilon\tilde{h}_w\omega^2\left[\left(\omega^2-\varepsilon^2\right)^2 - 4\varepsilon\omega^2\zeta_y\zeta_\theta\left(\omega^2-\varepsilon^2\right) - 4\omega^4{\zeta_\theta}^2\right]}{\left[\left(\omega^2-\varepsilon^2\right)^2 + \left(2\beta\varepsilon\omega + 2\varepsilon^2\omega\zeta_y\right)^2\right]^2}. \tag{3.37}$$

Figure 3.9 shows a sampling of ε^*_{tr} values obtained by solving Eq.(3.36) numerically and selecting the roots that yield local maxima in $|T_{tr}|$. As seen, there is a wide range of ε values that give rise to maximum sensitivity in H_{tr} due to weak coupling.

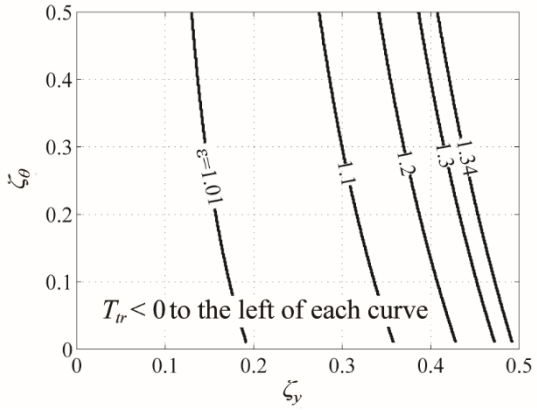

Figure 3.8: Contour Plot of T_{tr} = 0 of NP Damped System as Functions of ζ_y and ζ_θ for Various Values of $\varepsilon > 1$ ($h_w > 0$ is assumed)

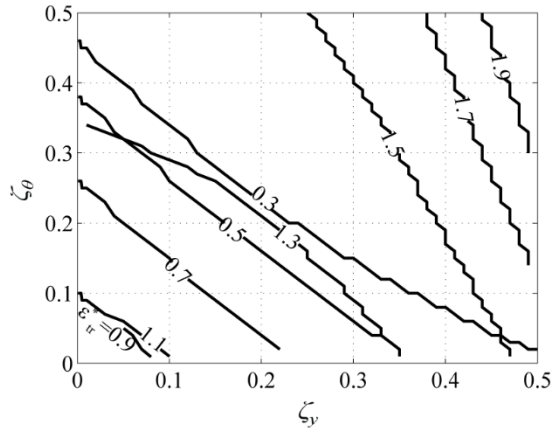

Figure 3.9: Contour Plot of ε^*_{tr} as Functions of ζ_y and ζ_θ

3.4. Practical Design Guidelines Based on Analysis

This section demonstrates how the results from the analyses of Section 3.3 can be used to provide hints to a designer on when and how to couple the vibration modes of a given UPM

machine by changing h. Design considerations for residual vibration reduction are provided first followed by those for transmissibility reduction.

3.4.1. Design Consideration for Residual Vibration Reduction

Equation (3.20) combined with Figures 3.2 and 3.4 are useful tools for designing a UPM machine to reduce $\|H_{Fy}\|_\infty$ via weak coupling. Using Eq.(3.20), one can determine which vibration mode – y or θ – is dominant for the decoupled machine; the dominant mode can then become the focus of attention for residual vibration reduction. Armed with the knowledge of the dominant mode, Figure 3.2 provides hints on what direction to make small changes h in order to reduce residual vibration. For instance, if the y-mode is dominant, one can determine the sign of T_y that corresponds to the ε, ζ_y and ζ_θ values of a given UPM machine. If $T_y < 0$ then placing the isolators higher than the CG (i.e., positive h) is more desirable; the opposite is true if $T_y > 0$. Similar inferences can be drawn if the θ-mode is dominant by monitoring the sign of T_θ. Figure 3.4 is useful in that it tells a designer which ε, ζ_y and ζ_θ combinations would provide the greatest reduction of $\|H_{Fy}\|_\infty$ through small changes in h. For instance, pneumatic isolators usually have a knob for adjusting ζ_θ (by changing c_z). Given ε and ζ_y for a specific UPM machine, a designer may want to tweak ζ_θ so that the combination of ε, ζ_y and ζ_θ for the machine lands on one of the curves of Figure 3.4.

Note that special care has to be taken when wC_θ/C_y is close to unity due to the tendency to have opposite trends in the signs of T_y and T_θ for a given ε, ζ_y and ζ_θ combination (as can be seen by comparing Figure 3.2 (a) and (b)). The implication is that coupling may reduce the dominant peak of the decoupled system but at the same time increase the non-dominant peak such that it becomes dominant after coupling. Another point to remember is that the analysis of Section 3.3 is only valid for small changes in h. It does not provide any information on how much the CG can be lowered or raised before residual vibration begins to increase or the system becomes unstable. The analysis by Ryaboy [36] provides useful guidance to a designer with regard to stability limits. In addition, a designer may want to plot $\|H_{Fy}\|_\infty$ as a function of h to determine the limits of h with regard to vibration reduction. To highlight why such a plot is important, let us assume that a UPM machine is designed for maximum sensitivity in the θ direction (i.e., $\varepsilon = \varepsilon^*_{\theta 1}$, the smaller of ε^*_θ in Eq.(3.24)). We would like to know the value of $|\tilde{h}| = \tilde{h}_{\max}$ beyond which $\|H_{Fy}\|_\infty$ becomes higher than its original magnitude at $h = 0$. In other words, $\tilde{h}_{\max}$ is the

dimensionless height of the isolators beyond which the vibration reduction benefits achieved by mode coupling (relative to decoupling) are nullified. Figure 3.10 shows contour plots of $\tilde{h}_{\max}$ as functions of ζ_y and ζ_θ for $\tilde{h}_F$ = 0.5, 1, 1.5 and 2. The hatched portion of each plot represents the design space where coupling increases residual vibration relative to decoupling. The color spectrum indicates the relative magnitudes of $\tilde{h}_{\max}$. As one observes, the relative sizes of the various regions of each are slightly different for each $\tilde{h}_F$ value. In each case, however, there is a sizeable region where coupling remains more beneficial than decoupling for large values of $\tilde{h}_{\max}$ (> 1.5). However, each plot also has a region where $\tilde{h}_{\max}$ values greater than about 0.4 nullify any benefits of coupling relative to decoupling.

Extending the design insights to $||H_{Fz}||_\infty$, we observe that since $T_z < 0$ in most scenarios, the decoupled state of the machine yields a local maximum of $||H_{Fz}||_\infty$, except for the very small subset of the design space to the left of each ε curve in Figure 3.5 where $||H_{Fz}||_\infty$ has a local minimum at $h = 0$. This result is very auspicious for residual vibration reduction in general using weak mode coupling because most of the conditions that reduce $||H_{Fy}||_\infty$ also reduce $||H_{Fz}||_\infty$. Therefore, a designer often does not have to tradeoff one for the other. However, notice that the curves for ε^*_z in Figure 3.7 are very different from those of ε^*_y or ε^*_θ in Figure 3.4. This means that a designer may have to choose between tuning their machine for maximum sensitivity in $||H_{Fy}||_\infty$ or $||H_{Fz}||_\infty$, depending on which they deem to be more critical or beneficial.

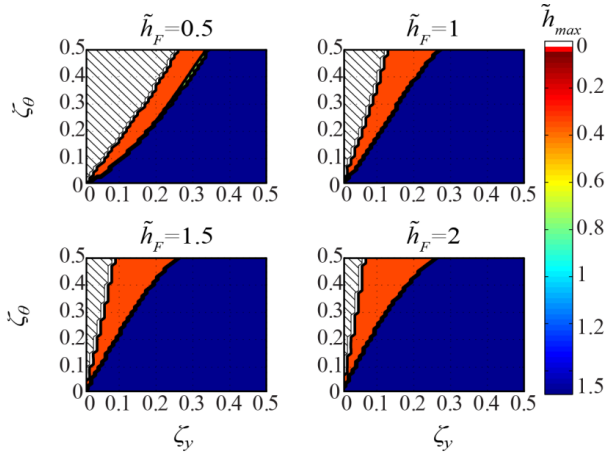

Figure 3.10: Contour Plot of $\tilde{h}_{\max}$ as Functions of ζ_y and ζ_θ for Various values of $\tilde{h}_F$. In This Example, the System is Assumed to be Designed with $\varepsilon = \varepsilon^*_{\theta 1}$. The Hatched Sections of Each Plot Indicate Regions where Mode Coupling Increases Vibrations

3.4.2. Design Consideration for Transmissibility Reduction

The logic used for determining design guidelines for residual vibration reduction can be applied to transmissibility. When $\varepsilon < 1$, $T_{tr} > 0$ always, meaning that weak coupling with negative h is always better than decoupling in terms of transmissibility. We had also observed that for $\varepsilon < 1$, $T_y > 0$ for most combinations of ζ_y and ζ_θ in Figure 3.2. This means that it is highly probable to simultaneously reduce transmissibility and residual vibration via weak coupling when $\varepsilon < 1$. The broader implication is that vibration reduction using mode coupling is not necessarily constrained by the well-known tradeoff between transmissibility and residual vibration reduction in passive systems! For $\varepsilon > 1$ the situation is not as straightforward; there is much less overlap between the conditions for reduction of residual vibration and transmissibility. However, a designer can use the directions and most sensitive conditions for $\|H_{Fy}\|_\infty$, $\|H_{Fz}\|_\infty$ and σ^2_H presented in this chapter as a guide to locate h (and tune ε, ζ_y or ζ_θ) so that a good compromise is struck between residual vibration and transmissibility reduction for the UPM machine.

3.5. Simulation and Experimental Validation

This section presents two sets of simulation and experiment results to validate the theoretical analysis presented in this chapter. The first set revisits the simulations and experiments conducted in Chapter 2 on a 5-axis ultra-precision milling machine to highlight the importance of considering NP damping compared to modal damping. The machine used in Chapter 2 was a commercial UPM machine to which the author no longer has access. Moreover, as reported in Chapter 2, there were practical limitations to the experiments that could be conducted on the machine. Therefore, a second set of simulations and laboratory experiments are conducted on a prototype of a UPM machine base which has been specially designed to remove many of the restrictions that may be presented by a specific commercial UPM machine.

3.5.1. Simulation and Experiments on 5-Axis Milling Machine

Refer back to Figure 2.9 showing the schematic of the Mori Seiki's NN1000 ultra-precision 5-axis milling machine that was employed for the simulations and experiments in Chapter 2. As explained in Chapter 2, the residual vibrations in its x-z plane were negligible because of the relatively small moving mass of its x-axis. Consequently, the simulations and experiments

reported in Chapter 2 were focused on the *y-z* plane of the machine. Furthermore, transmissibility was not analyzed in the Chapter 2. Therefore, only $\|H_{Fy}\|_\infty$ and $\|H_{Fz}\|_\infty$ are considered in this first set of simulations/experiments.

Considering $\|H_{Fy}\|_\infty$, the parameters provided in Table 3.1 are used to calculate ρ = 285 mm, $\tilde{h}_F$ = 1.53, ε =1.21, $\zeta_y = \zeta_\theta$ = 0.15 and β = 0.0315 (i.e., machine is non-proportionally damped). Eq.(3.20), with w = 1 m gives the ratio $C_{\theta,Fy}/C_{y,Fy}$ as 5.36, meaning that $H_{\theta,Fy}(\omega_\theta)$ (i.e., the rocking vibration) is dominant when h = 0. With ε =1.21 and $\zeta_y = \zeta_\theta$ = 0.15, $T_\theta > 0$ can be deduced from Figure 3.2 (b). This means that placing the isolators below the CG (i.e., $h < 0$) will reduce the resonance peak of $|H_{\theta,Fy}|$. From Eq.(3.24), ε^*_θ = 0.86 or ε^*_θ = 1.17 can be calculated. This means that, with ε =1.21, the machine is close to a condition for maximum sensitivity to weak coupling (i.e., ε^*_θ = 1.17). Note, however, that $T_y < 0$ at ε = 1.21, meaning that selecting $h <$ 0 will increase the peak of the less-dominant $|H_{y,Fy}|$; but since $C_{\theta,Fy}/C_{y,Fy}$ is far from unity, the reduction in the peak of $|H_{\theta,Fy}|$ can be expected to outweigh the increase in the peak of $|H_{y,Fy}|$ for small changes in h. Weak coupling can therefore be expected to reduce residual vibration compared to decoupling. The same conclusions were reached in Chapter 2 based on the analysis employing modal damping, and the residual vibrations of the machine were observed in experiments to drastically reduce when h was changed from 0 to −116 mm, as was shown in Figure 2.13. Figure 3.11 provides an explanation for the similarities between the modal and the NP damping predictions for the machine. As can be seen, the resonance peak of $|H_{\theta,Fy}|$ for modal and NP damping have the same qualitative behavior in the interval $\tilde{h} \in [-0.41, 0]$ (i.e., $h \in$ [−116, 0] mm). It was mere coincidence that the analysis of Chapter 2 was conducted within this interval. However, the influence of NP damping can be observed in the slightly different sensitivities to weak coupling around h = 0 – the magnitude of T_θ is a bit smaller with NP damping compared to the modally damped case. Moreover, even though the analysis presented in this chapter is focused on the region around h = 0, one observes that the influence of NP damping on the machine's vibration response is much more significant when $h > 0$ and $h < -116$ mm. Also, the $h > 0$ portion of the plot demonstrates that conclusions derived based on coupling in the vicinity of h = 0 may not hold for larger values of h, hence the need to determine $\tilde{h}_{\max}$ for the particular condition of interest, as discussed in Section 3.4. Simulated and measured $|H_{\theta,Fy}|$ plots for the machine are shown in Figure 3.12 (a) and (b). At h = 0, the modally and NP damped

systems have exactly the same response, which is reasonably close to that measured from the machine. At $h = -116$ mm one observes that the peaks of the NP damped system (which differ slightly from those of the modally damped) are in better agreement with those of the measured response, as should be expected since $\beta \neq 0$ for the machine.

Parameter	Value
m [kg]	1,182
I [kg-m^2]	96
k_y [N/m]	880,000
k_θ [Nm/rad]	104,430
h_F [mm]	435
c_y [kg/s]	9676
c_θ [Nm-s/rad]	950
r [mm]	70

Table 3.1: Key Parameters of NN1000 DCG Used for Simulations

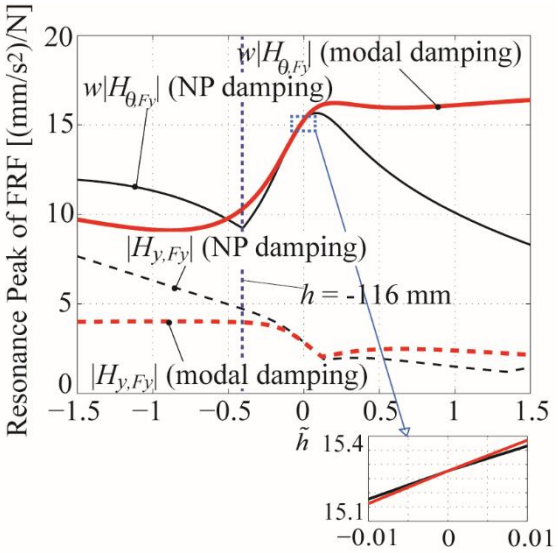

Figure 3.11: Resonance Peaks of $|H_{y,Fy}|$ and $w|H_{\theta,Fy}|$ of NN1000 as Functions of Dimensionless Isolator Height (w = 1 m). Note: $h = -116$ mm corresponds to $\tilde{h} = -0.41$

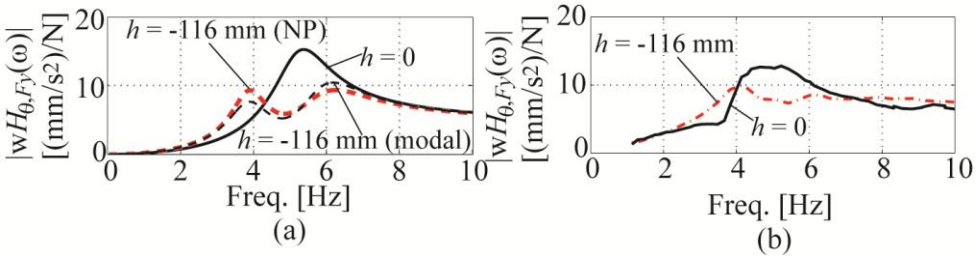

Figure 3.12: FRFs of NN1000 obtained from (a) Simulations and (b) Experiments for h = 0 and h= −116 mm. w = 1m

For the z direction, $\|H_{Fz}\|_\infty$ is investigated in simulation only because the vibrations induced by the z-axis could not be measured reliably in the NN1000 machine due to their relatively low levels, as reported in Chapter 2. Using ε =1.21 and $\zeta_y = \zeta_\theta = 0.15$, $T_z < 0$ can be deduced from Figure 3.5, which means that $\|H_{Fz}\|_\infty$ decreases in either direction of h. Figure 3.13 provides a comparison between the modal and NP damping-based plots of $\|H_{Fz}\|_\infty$. In the contrast with results of $\|H_{Fy}\|_\infty$, the $\|H_{Fz}\|_\infty$ of the NN1000 machine is more sensitive to coupling with NP damping compared to modal damping. However, similar to $\|H_{Fy}\|_\infty$, the influence of NP damping on the machine's vibration response becomes more pronounced as the system becomes more coupled. It is interesting to note that with ε =1.21, the machine is approximately three times less sensitive to weak coupling than with $\varepsilon^*_z = 0.997$ ($T_z = -23.24$ and -8, respectively, at $\varepsilon = 0.977$ and 1.21). This means that a lot of value could be gained by tweaking the machine's parameters to coincide with ε^*_z, as shown in Figure 3.13.

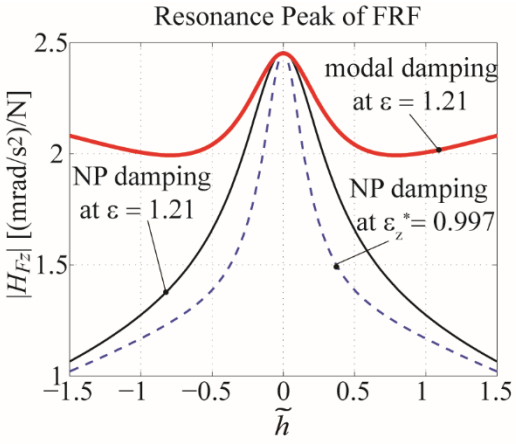

Figure 3.13: $|H_{Fz}|$ of NN1000 as Functions of Dimensionless Isolator Height

3.5.2. Simulation and Experiments on UPM Machine Base Prototype

Figure 3.14 shows the reconfigurable UPM machine base prototype used for additional simulations/experiments. The prototype consists of a 0.8 ton base of dimensions 749.3 mm × 749.3 mm × 495.3 mm, supported symmetrically on a foundation by four pneumatic isolators (Bilz model BiAir 1-ED). The arrays of threaded holes on the base allow the isolators to be mounted at different discrete locations so that h can be varied. For evaluating residual vibration, an electromagnetic shaker (APS Dynamics model APS 113) is attached to the base and is used to provide the excitation forces F_y and F_z at locations h_F and r. The vibration of the structure is measured using accelerometers (PCB Piezotronics model 393B05) with sensitivity of 10.42 V/g.

Transmissibility experiments are conducted by using an impact hammer (PCB Piezotronics model 086D20) to excite the foundation in the horizontal direction; the horizontal accelerations of the foundation (i.e., $\ddot{y}_0$) and those of the base (at height h_w = 220 mm from the CG) are measured and used to determine the transmissibility. Table 3.2 summarizes the relevant parameters of the prototype. The isolator stiffness and damping coefficients have been identified experimentally, while the mass and moment of inertia of the base have been determined from its CAD model. Its mass and inertia are reported as a range of values in the table due to slight variations resulting from the repositioning of the shaker (and balance masses to keep the base level) for each experiment.

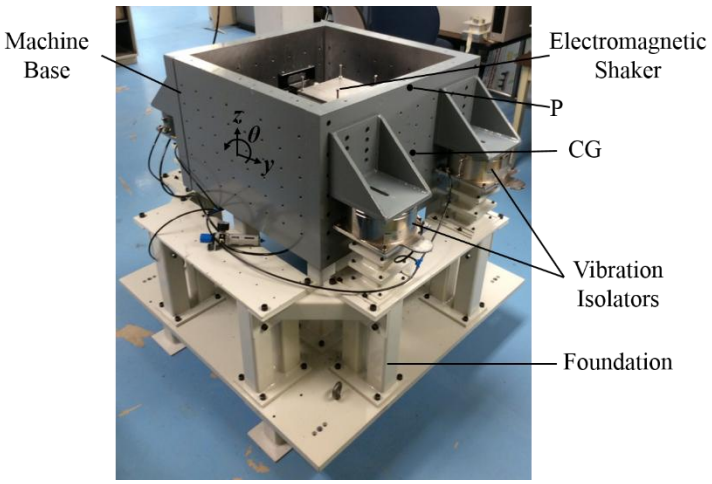

Figure 3.14: Reconfigurable UPM Machine Base Prototype Used for Simulations and Experiments. Note that the Point Labelled P represents a Sensitive Location on the Machine Base (i.e., the Distance between the CG and Point P is h_w)

Parameter	Value
m [kg]	830-834
I [kg-m^2]	77-80
k_y [N/m]	1,150,319
k_θ [Nm/rad]	80,289
c_y [kg/s]	3,739
c_θ [Nm-s/rad]	1,118
h_F [mm]	130
r [mm]	119
h_w [mm]	220

Table 3.2: Key Parameters of UPM Machine Base Prototype Used for Simulations

To evaluate $||H_{Fy}||_\infty$, we use the parameters in Table 3.2 (with m = 834 kg and I = 77 kg-m^2) to calculate ρ = 303.9 mm, $\tilde{h}_F$ = 0.43, ε = 0.87, ζ_y = 0.06, ζ_θ = 0.22, and β = 0.168 (i.e., non-proportionally damped). The ratio C_θ/C_y = 0.39, implying that $|H_{y,Fy}|$ has the dominant peak for the decoupled system. Figure 3.2 reveals that $T_y > 0$; therefore placing the isolators below the CG (i.e., $h < 0$) will reduce the peak of $|H_{y,Fy}|$. This is confirmed by Figure 3.15 (a) which depicts the simulated variation of the peaks of $|H_{y,Fy}|$ and $w|H_{\theta,Fy}|$ as functions of h. For evaluating $||H_{Fz}||_\infty$, m = 830 kg and I = 80 kg-m^2. Therefore, ρ = 310.5 mm, $\tilde{r}$ = 0.382 and ε = 0.85, ζ_y = 0.06, ζ_θ = 0.22 and β = 0.169. From Figure 3.5, $T_z < 0$ (i.e., a local maximum occurs at h = 0); selecting $h < 0$ or $h > 0$ will reduce the peak of $|H_{Fz}|$; Figure 3.15 (b) attests to this fact.

Transmissibility (i.e., σ^2_H) is evaluated using the same parameters applied to $||H_{Fy}||_\infty$; therefore $\tilde{h}_w$ = 0.72. $T_{tr} > 0$ for any value of $\varepsilon < 1$ so $h < 0$ is favorable for vibration reduction, as confirmed by Figure 3.15 (c). We therefore have the very desirable condition where, compared to the recommended practice of decoupling, weak mode coupling (with $h < 0$) is predicted to simultaneously reduce $||H_{Fy}||_\infty$, $||H_{Fz}||_\infty$ and σ^2_H. In the rest of this section, we validate this finding experimentally by comparing residual vibration and transmissibility responses for h = 0 (decoupled) and h = −65 mm (coupled).

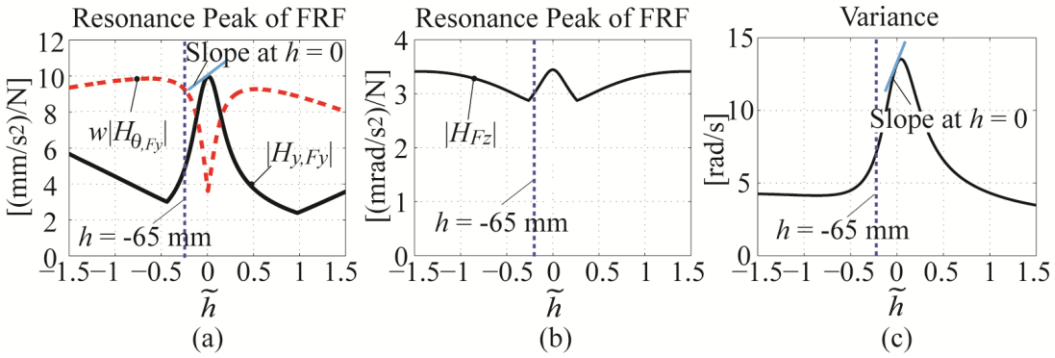

Figure 3.15: Simulated Plots of (a) $|H_{y,Fy}|$ and $w|H_{\theta,Fy}|$, (b) $|H_{Fz}|$, and (c) Variance of H_{tr} of UPM Machine Base Prototype as Functions of Dimensionless Isolator Height. w = 1m

Figure 3.16 (a) and (b) show the simulated and experimentally measured $|H_{y,Fy}|$ for the decoupled and coupled systems. Both are in close agreement and show about 40% reduction in the resonance peak due to mode coupling. A similar comparison of simulated and measured FRFs is presented in Figure 3.16 (c) and (d) for residual vibration in the z-direction, showing about 25% reduction in the resonance peak. The effect of the reported resonance peak reductions

can be seen in Figure 3.17 which shows the residual vibration response of the base to a constant acceleration (1g) motion command applied to the shaker to move it from rest to 2590 mm/min. The settling time of the coupled system is significantly improved relative to the decoupled.

Figure 3.18 (a) and (b) compare the simulated and experimentally measured $|H_{tr}|$ of the machine. A close agreement is obtained between both plots except for very low frequencies (< 4 Hz) where the experiment results are poor due to the inability of the hammer to properly excite the foundation. However, the benefit of mode coupling is very evident in the reduction of the resonance peaks by about 50%. Moreover, attenuation beyond resonance is not adversely affected by coupling. As a final note, the conditions for maximum sensitivity for the UPM machine prototype are calculated as $\varepsilon^*_y = 0.71$ or $\varepsilon^*_y = 1.18$, $\varepsilon^*_z = 0.95$ and $\varepsilon^*_{tr} = 0.65$ or $\varepsilon^*_{tr} = 1.24$. Therefore, there is some room for improvement in each response, if desired. However, one would have to decide on which response to maximize, since the conditions for maximum sensitivity are not the same for all three responses.

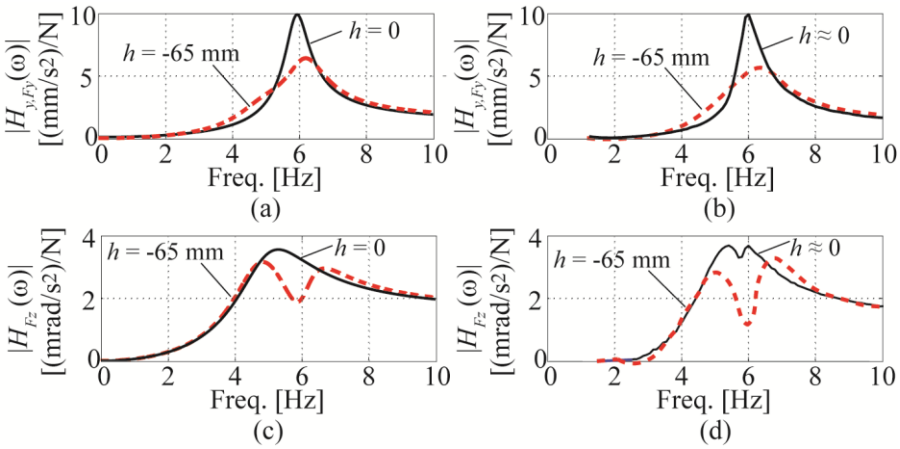

Figure 3.16:$|H_{y,Fy}|$ Obtained from (a) Simulations and (b) Experiments; $|H_{Fz}|$ Obtained from (c) Simulations and (d) Experiments for h = 0 and h = −65 mm

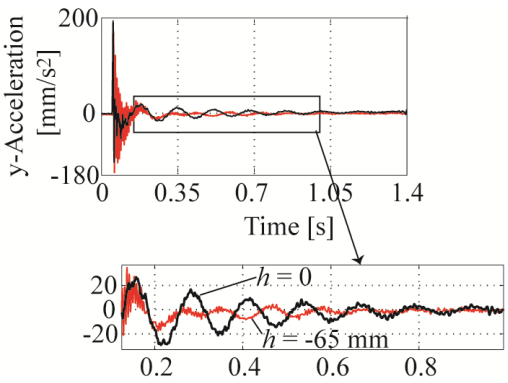

Figure 3.17: *y*-Acceleration of Base Measured at Point P (in Figure 3.14) for $h = 0$ and $h = -65$ mm during Motion of *y*-axis from Rest to 2590 mm/min

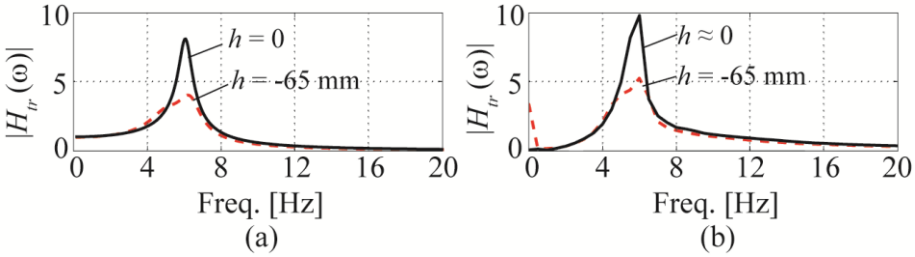

Figure 3.18: $|H_{tr}|$ Obtained from (a) Simulations and (b) Experiments for $h = 0$ and $h = -65$ mm.

3.6. Conclusion

This chapter has investigated the effects mode coupling on the residual vibration and transmissibility of single-variable, planar, passively-isolated UPM machines with non-proportional (NP) damping. It complements a similar investigation in Chapter 2 which was based on the assumption of modal damping. A perturbation technique is used to analyze the H_∞ and H_2 norms of residual vibration and transmissibility FRFs, respectively. The results show that, even though NP damping changes the vibration behavior of the isolated machine compared to modal damping, mode coupling still provides ample opportunities to reduce base vibrations, providing that the machine is properly designed. Guidelines for properly designing a UPM machine to best exploit mode coupling for vibration reduction in non-proportionally damped isolation systems are provided. Simulations and experiments on UPM machine prototypes are used to demonstrate significant benefits of mode coupling relative to decoupling with regard to both residual vibration and transmissibility for two non-proportionally damped systems.

CHAPTER 4
A LINEAR FEEDBACK CONTROL FRAMEWORK FOR OPTIMALLY LOCATING PASSIVE VIBRATION ISOLATORS WITH KNOWN STIFFNESS AND DAMPING PARAMETERS

4.1. Introduction

The analyses presented in Chapters 2 and 3 have provided useful design guidelines for exploiting mode coupling for vibration reduction in passively-isolated UPM machines. However, the guidelines of Chapters 2 and 3 are very limited because they only apply to weak mode coupling on single-variable, planar systems. Moreover, they do not consider issues of gravitational stability that may result from (strong) mode coupling. This chapter seeks to provide a versatile tool that can be used to optimally place passive isolators for multivariable, 3-D systems, including the effects of strong mode coupling and gravitational stability.

A lot of work has been done related to the optimal tuning and placement of passive isolators to minimize unwanted vibration [1,2,26,42-53]. One very powerful framework for optimizing passive systems is to re-formulate the optimization problem into an optimal, preferably linear time invariant (LTI), control problem [26,46-53]. A major benefit of an LTI control theoretic formulation is that it is very systematic and thus scalable to large problems. Furthermore, it allows well-established LTI control theories and techniques to be applied to the solution and analyses of the optimization problem, thus improving the solution process and lending useful insights about the problem and its solution.

It is however observed that the vast majority of LTI control formulations in the literature, for optimizing passive isolated systems, focus on the stiffness/damping coefficients of the isolators as optimization variables, while isolator locations are considered to be fixed parameters [26,46-

53]. This is because stiffness and damping terms are linearly related to system states and so can be readily represented as feedback gains in an LTI control framework. Some works have presented the placement of isolators at multiple discrete locations as LTI control problems involving the optimal design of the input matrix (of a system described in state-space) via iteration (e.g., [48]) or based on measures of controllability (e.g., [50]). However, the discrete nature of such optimization problems and the open-loop criterion (i.e., controllability) with which they are defined may lead to solutions that do not minimize the cost function in a closed-loop sense [82].

When isolator locations are non-discrete variables, they are nonlinearly related to the system states; hence they do not readily fit into an LTI control framework. Attempts to optimize non-discrete passive isolator locations within LTI control frameworks have not been systematic. For example, Zuo and Nayfeh [53] optimized tuned mass damper (TMD) locations by running repeated optimizations of TMD stiffness/damping values for multiple TMD locations and then selecting the best result. Bagdatli et al. [52] generated optimal eigenvalues for an isolated system using the LQR method and then used nonlinear least squares to determine stiffness/damping parameters and isolator locations that approximately matched the optimal eigenvalues. To the author's knowledge, there is currently no approach for systematically incorporating non-discrete isolator locations into an LTI framework for the purpose of optimization.

This chapter shows that the optimal placement of isolators into non-discrete locations can be formulated as an LTI control problem if the stiffness and damping of the vibration isolators are assumed to be known. This assumption is valid in many practical situations where isolators have been provided to an engineer who is then tasked to properly locate them. A static output feedback gain matrix is used to represent the isolator locations to be optimized, and the nonlinear relationships between isolator locations and system states are cast into an LTI framework by defining a non-zero feedforward matrix. H_2/H_∞ optimal control theory is then applied to the resulting control system to determine optimal isolator locations, using a recently-proposed convex-overbounding technique [83-85] to deal with the non-convexity of the optimization problem.

The rest of this chapter is organized as follows. In Section 4.2, the isolator placement problem is defined for a generalized (multivariable, 3-D) isolation system and the proposed

control theoretic approach is formulated. In Section 4.3, H_2 and H_∞ techniques are formally introduced for minimizing unwanted vibration based on the proposed framework, and a convex-overbounding technique [83-85] for solving the resulting nonconvex H_2/H_∞ optimization problem is outlined. Section 4.4 presents practical case studies to demonstrate the effectiveness of the proposed approach, and to exemplify some of the analysis tools and insights that control theory provides. Finally, conclusions are presented in Section 4.5.

4.2. Isolator Placement Problem and its Control Theoretic Representation

4.2.1. Problem Formulation

Consider the generalized isolation system shown in Figure 4.1, consisting of a rigid body supported by n isolators, of which only isolator $i \in \{1, 2,\ldots,n\}$ is shown. In the context of this dissertation, the rigid body is assumed be the base of a UPM machine, but it could equally represent an automobile, aircraft engine, building, etc. A global inertial coordinate system (CS) is defined such that its origin coincides with the CG of the base, when the base is at its equilibrium position; its axes (x, y and z) are aligned with the base's principal axes of inertia. The base has mass m and principal moments of inertia I_x, I_y and I_z about the x, y and z axes, respectively. Each isolator i is mounted at point P_i, positioned at distance $\mathbf{a}_i = \{a_{x,i}\ a_{y,i}\ a_{z,i}\}^{\mathrm{T}}$ relative to the global CS. A local CS (x_i, y_i, z_i) is established at P_i such that each isolator i is described by three stiffness coefficients ($k_{x,i}$, $k_{y,i}$, $k_{z,i}$) and three damping coefficients ($c_{x,i}$, $c_{y,i}$, $c_{z,i}$) aligned along the x_i, y_i and z_i directions, respectively. The stiffness and damping coefficients of each isolator are assumed to be known.

The isolated system experiences exogenous disturbances from: (i) seismic excitations caused by displacements $\{x_0\ \ y_0\ \ z_0\}^{\mathrm{T}}$ of the ground; (ii) forces $\mathbf{F}_e = \{F_{x,e}\ \ F_{y,e}\ \ F_{z,e}\}^{\mathrm{T}}$ ($e \in \{1, 2,\ldots,E\}$) acting at points P_e on the isolated base; and (iii) the force of gravity (mg). Position vectors $\mathbf{r}_e = \{r_{x,e}\ \ r_{y,e}\ \ r_{z,e}\}^{\mathrm{T}}$ relative to the global CS are used to define points P_e, of which only one is shown in Figure 4.1. Without loss of generality, in the context of this chapter, we assume that $\mathbf{F}_e$ are caused by inertial reactions of moving masses on the machine base.

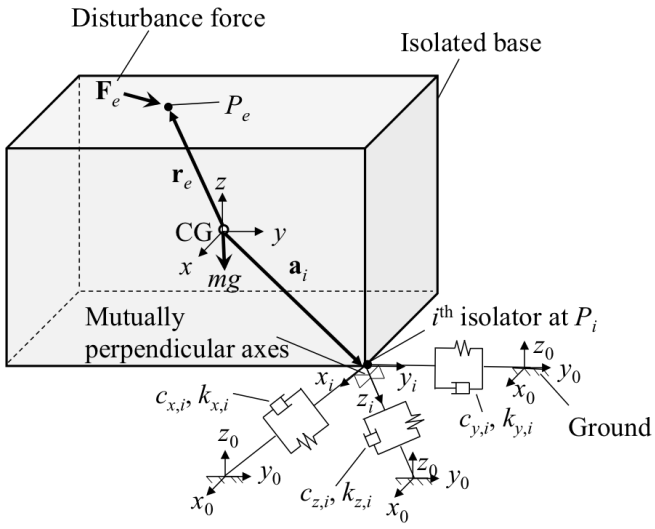

Figure 4.1: Model of Generalized Passive Isolation System

Let us define the generalized displacement vectors of the isolated system and ground in the global CS as $\mathbf{q} = \{x\ y\ z\ \theta_x\ \theta_y\ \theta_z\}^{\mathrm{T}}$ and $\mathbf{q}_0 = \{x_0\ y_0\ z_0\ 0\ 0\ 0\}^{\mathrm{T}}$, respectively, where θ_x, θ_y and θ_z represent small angle rotations about the x, y and z axes. Accordingly, the equation of motion of the isolated system can be written as

$$\mathbf{M}\ddot{\mathbf{q}} + \mathbf{C}\dot{\mathbf{q}} + \mathbf{K}\mathbf{q} = \mathbf{C}\dot{\mathbf{q}}_0 + \mathbf{K}\mathbf{q}_0 + \mathbf{F}_g + \mathbf{F}, \tag{4.1}$$

where

$$\mathbf{M} = \mathrm{diag}\left(\begin{Bmatrix} m & m & m & I_x & I_y & I_z \end{Bmatrix}\right),\ \mathbf{C} = \sum_{i=1}^{n} \mathbf{T}_i^{\mathrm{T}} \mathbf{C}_i \mathbf{T}_i,\ \mathbf{K} = \sum_{i=1}^{n} \mathbf{T}_i^{\mathrm{T}} \mathbf{K}_i \mathbf{T}_i. \tag{4.2}$$

In Eq.(4.1), $\mathbf{F}_g$ and $\mathbf{F}$ respectively represent the equivalent forces and moments at the origin of the global CS caused by gravity and by the combination of all forces $\mathbf{F}_e$. The matrices $\mathbf{K}_i$ and $\mathbf{C}_i$ in Eq.(4.2) are respectively the equivalent stiffness and damping matrices of i^{th} isolator transformed to the global CS; they are given by

$$\mathbf{C}_i = \mathbf{T}_{rot,i}^{\mathrm{T}}\, \mathrm{diag}\left(\begin{Bmatrix} c_{x,i} & c_{y,i} & c_{z,i} \end{Bmatrix}\right) \mathbf{T}_{rot,i},\ \ \mathbf{K}_i = \mathbf{T}_{rot,i}^{\mathrm{T}}\, \mathrm{diag}\left(\begin{Bmatrix} k_{x,i} & k_{y,i} & k_{z,i} \end{Bmatrix}\right) \mathbf{T}_{rot,i}, \tag{4.3}$$

with $\mathbf{T}_{rot,i}$ representing a rotation matrix expressed as

$$\mathbf{T}_{rot,i} = \begin{bmatrix} \cos\beta_i \cos\gamma_i & \cos\beta_i \sin\gamma_i & -\sin\beta_i \\ -\cos\alpha_i \sin\gamma_i + \sin\alpha_i \sin\beta_i \cos\gamma_i & \cos\alpha_i \cos\gamma_i + \sin\alpha_i \sin\beta_i \sin\gamma_i & \sin\alpha_i \cos\beta_i \\ \sin\alpha_i \sin\gamma_i + \cos\alpha_i \sin\beta_i \cos\gamma_i & -\sin\alpha_i \cos\gamma_i + \cos\alpha_i \sin\beta_i \sin\gamma_i & \cos\alpha_i \cos\beta_i \end{bmatrix}. \quad (4.4)$$

The rotation matrix aligns the axes of the local CS to those of the global CS based on Euler angles α_i, β_i and γ_i (i.e., the orientation of the i^{th} isolator) about the *x, y* and *z* axes. The matrix $\mathbf{T}_i = [\mathbf{I} \quad L(\mathbf{a}_i)]$ in Eq.(4.2) transforms $\mathbf{C}_i$ and $\mathbf{K}_i$ from their point of action at P_i to equivalent matrices acting at the origin of the global CS, where $\mathbf{I}$ is the identity matrix of appropriate size and L is an operator which converts a vector to a skew symmetric tensor. For example, $L(\mathbf{a}_i)$ is given by

$$L(\mathbf{a}_i) = \begin{bmatrix} 0 & a_{z,i} & -a_{y,i} \\ -a_{z,i} & 0 & a_{x,i} \\ a_{y,i} & -a_{x,i} & 0 \end{bmatrix}. \quad (4.5)$$

Note that if $\boldsymbol{\theta} = \{\theta_x \; \theta_y \; \theta_z\}^{\mathrm{T}}$ then $L(\mathbf{a}_i)\boldsymbol{\theta} = -L^{\mathrm{T}}(\mathbf{a}_i)\boldsymbol{\theta} = \boldsymbol{\theta} \times \mathbf{a}_i$, where × denotes the cross product of two vectors. Accordingly, $\mathbf{F}_g$ and $\mathbf{F}$ can be expressed as

$$\mathbf{F}_g = \begin{bmatrix} \mathbf{0} & \mathbf{0} \\ L(m\mathbf{g}) & \mathbf{0} \end{bmatrix} (\mathbf{q} - \mathbf{q}_0), \quad \mathbf{F} = \sum_{e=1}^{E} \underbrace{\begin{bmatrix} \mathbf{I} \\ L^{\mathrm{T}}(\mathbf{r}_e) \end{bmatrix} \mathbf{T}_e \hat{\mathbf{f}}}_{\mathbf{F}_e} = \mathbf{T}_{CG-e} \hat{\mathbf{f}}, \quad (4.6)$$

where $\mathbf{g} = \{0 \; 0 \; -g\}^{\mathrm{T}}$, $\hat{\mathbf{f}} = \{\hat{f}_x \quad \hat{f}_y \quad \hat{f}_z\}^{\mathrm{T}}$ is a unit vector such that $\mathbf{F}_e = \mathbf{T}_e \hat{\mathbf{f}}$, and $[\mathbf{I} \quad L(\mathbf{r}_e)]^{\mathrm{T}}$ is a matrix that transforms $\mathbf{F}_e$ (acting at point P_e) to equivalent forces and moments acting at the CG. Observe that $\mathbf{F}_g$ considers only the moments caused by gravity when the base deviates from its equilibrium position (i.e., $\mathbf{q} - \mathbf{q}_0 = \mathbf{0}$). This is because, when the base is at its equilibrium position, the effects of gravity are cancelled out by the elastic forces from the isolators.

4.2.2. Control Theoretic Representation of Isolator Placement Problem

It can be observed from Eqs.(4.1) and (4.2) that the isolator locations ($\mathbf{a}_i$), which are contained in $\mathbf{T}_i$, are quadratically related to $\mathbf{q}$ and $\mathbf{q}_0$ (and their derivatives) through $\mathbf{K}$ and $\mathbf{C}$; a simple single-variable example is presented in the Appendix to help demonstrate this quadratic relationship more clearly. In this section, we present a framework that allows this quadratic (i.e., nonlinear) relationship to be represented as a multivariable LTI feedback controller, with the

isolator locations as the feedback gains. To do this, let us re-organize Eq.(4.1) such that every term containing isolator locations is moved into a vector $\mathbf{F}_a$; i.e.,

$$\mathbf{M}\ddot{\mathbf{q}} + \underbrace{\sum_{i=1}^{n}\begin{bmatrix}\mathbf{C}_i & \mathbf{0}\\ \mathbf{0} & \mathbf{0}\end{bmatrix}}_{\hat{\mathbf{C}}}(\dot{\mathbf{q}}-\dot{\mathbf{q}}_0) + \underbrace{\sum_{i=1}^{n}\begin{bmatrix}\mathbf{K}_i & \mathbf{0}\\ \mathbf{0} & \mathbf{0}\end{bmatrix}}_{\hat{\mathbf{K}}}(\mathbf{q}-\mathbf{q}_0) + \underbrace{\begin{bmatrix}\mathbf{0} & \mathbf{0}\\ L^{\mathrm{T}}(m\mathbf{g}) & \mathbf{0}\end{bmatrix}}_{\hat{\mathbf{K}}_g}(\mathbf{q}-\mathbf{q}_0) = \mathbf{F}+\mathbf{F}_a, \tag{4.7}$$

where $\mathbf{F}_a$ is given by

$$\mathbf{F}_a = \sum_{i=1}^{n}\begin{bmatrix}\mathbf{0} & \mathbf{C}_i L(\mathbf{a}_i)\\ L^{\mathrm{T}}(\mathbf{a}_i)\mathbf{C}_i & L^{\mathrm{T}}(\mathbf{a}_i)\mathbf{C}_i L(\mathbf{a}_i)\end{bmatrix}(\dot{\mathbf{q}}_0-\dot{\mathbf{q}}) + \sum_{i=1}^{n}\begin{bmatrix}\mathbf{0} & \mathbf{K}_i L(\mathbf{a}_i)\\ L^{\mathrm{T}}(\mathbf{a}_i)\mathbf{K}_i & L^{\mathrm{T}}(\mathbf{a}_i)\mathbf{K}_i L(\mathbf{a}_i)\end{bmatrix}(\mathbf{q}_0-\mathbf{q}). \tag{4.8}$$

Notice that, because of its dependence on $\mathbf{q}-\mathbf{q}_0$, $\mathbf{F}_g$ has been moved to the left hand side of Eq.(4.7), where it acts as an equivalent stiffness term. Accordingly, $\mathbf{F}_a$ can be re-written as

$$\mathbf{F}_a = \sum_{i=1}^{n}\underbrace{\begin{bmatrix}\mathbf{C}_i & \mathbf{0}\\ \mathbf{0} & \mathbf{I}\end{bmatrix}}_{\bar{\mathbf{C}}_{L,i}}\underbrace{\begin{bmatrix}L(\mathbf{a}_i) & \mathbf{0}\\ \mathbf{0} & L^{\mathrm{T}}(\mathbf{a}_i)\end{bmatrix}}_{\boldsymbol{\Gamma}_{c,i}}\mathbf{v}_{c,i} + \sum_{i=1}^{n}\underbrace{\begin{bmatrix}\mathbf{K}_i & \mathbf{0}\\ \mathbf{0} & \mathbf{I}\end{bmatrix}}_{\bar{\mathbf{K}}_{L,i}}\underbrace{\begin{bmatrix}L(\mathbf{a}_i) & \mathbf{0}\\ \mathbf{0} & L^{\mathrm{T}}(\mathbf{a}_i)\end{bmatrix}}_{\boldsymbol{\Gamma}_{k,i}}\mathbf{v}_{k,i}, \tag{4.9}$$

based on so-called 'measured outputs', $\mathbf{v}_{c,i}$ and $\mathbf{v}_{k,i}$, defined as

$$\mathbf{v}_{c,i} = \underbrace{\begin{bmatrix}\mathbf{0} & \mathbf{I}\\ \mathbf{C}_i & \mathbf{0}\end{bmatrix}}_{\bar{\mathbf{C}}_{q,i}}(\dot{\mathbf{q}}_0-\dot{\mathbf{q}}) + \underbrace{\begin{bmatrix}\mathbf{0} & \mathbf{0}\\ \mathbf{C}_i & \mathbf{0}\end{bmatrix}}_{\bar{\mathbf{C}}_{u,i}}\mathbf{u}_{c,i},\ \mathbf{v}_{k,i} = \underbrace{\begin{bmatrix}\mathbf{0} & \mathbf{I}\\ \mathbf{K}_i & \mathbf{0}\end{bmatrix}}_{\bar{\mathbf{K}}_{q,i}}(\mathbf{q}_0-\mathbf{q}) + \underbrace{\begin{bmatrix}\mathbf{0} & \mathbf{0}\\ \mathbf{K}_i & \mathbf{0}\end{bmatrix}}_{\bar{\mathbf{K}}_{u,i}}\mathbf{u}_{k,i}. \tag{4.10}$$

Vectors $\mathbf{u}_{c,i}$ and $\mathbf{u}_{k,i}$ are respectively the damping and stiffness-related portions of the equivalent control inputs for the i^{th} isolator, given by

$$\mathbf{u}_{c,i} = \boldsymbol{\Gamma}_{c,i}\mathbf{v}_{c,i},\ \ \mathbf{u}_{k,i} = \boldsymbol{\Gamma}_{k,i}\mathbf{v}_{k,i}, \tag{4.11}$$

where $\boldsymbol{\Gamma}_{c,i}$ and $\boldsymbol{\Gamma}_{k,i}$ respectively represent the feedback gain matrices associated with $\mathbf{u}_{c,i}$ and $\mathbf{u}_{k,i}$. Notice from Eq.(4.9) that $\boldsymbol{\Gamma}_{c,i} = \boldsymbol{\Gamma}_{k,i}$ because they both depend (linearly) on the location of the i^{th} isolator, which is assumed to have its spring and damper collocated. However, if it is preferred to treat the spring and damper of the isolator as non-collocated elements, $\boldsymbol{\Gamma}_{c,i}$ and $\boldsymbol{\Gamma}_{k,i}$ would be different. The overall control input vector, measured output vector and control gain matrix for the i^{th} isolator can therefore be defined as

$$\mathbf{u}_i = \begin{Bmatrix} \mathbf{u}_{k,i} \\ \mathbf{u}_{c,i} \end{Bmatrix}, \quad \mathbf{v}_i = \begin{Bmatrix} \mathbf{v}_{k,i} \\ \mathbf{v}_{c,i} \end{Bmatrix}, \quad \mathbf{\Gamma}_i = \begin{bmatrix} \mathbf{\Gamma}_{k,i} & \mathbf{0} \\ \mathbf{0} & \mathbf{\Gamma}_{c,i} \end{bmatrix}. \tag{4.12}$$

The implication is that each isolator has a 12×12 structured feedback gain matrix associated with it, representing the *x*, *y* and *z* components of $\mathbf{a}_i$ for the spring and damper of the isolator. (Please see the Appendix for a simple example of the structured feedback matrix involving only one variable, to aid clarity).

The equation of motion of the system of *n* isolators given in Eq.(4.1) can now be re-written in state space form as

$$\dot{\mathbf{x}} = \mathbf{A}\mathbf{x} + \mathbf{B}_{\mathrm{w}}\mathbf{w} + \mathbf{B}_{\mathrm{u}}\mathbf{u}, \tag{4.13}$$

where

$$\begin{aligned} &\mathbf{x} = \left\{ (\mathbf{q} - \mathbf{q}_0)^{\mathrm{T}} \quad (\dot{\mathbf{q}} - \dot{\mathbf{q}}_0)^{\mathrm{T}} \right\}^{\mathrm{T}}, \quad \mathbf{w} = \left\{ \hat{\mathbf{f}}^{\mathrm{T}} \quad \hat{\ddot{\mathbf{q}}}_0^{\mathrm{T}} \right\}^{\mathrm{T}}, \quad \mathbf{u} = \left\{ \mathbf{u}_1^{\mathrm{T}} \quad \mathbf{u}_2^{\mathrm{T}} \quad \dots \quad \mathbf{u}_n^{\mathrm{T}} \right\}^{\mathrm{T}}, \\ &\mathbf{A} = \begin{bmatrix} \mathbf{0} & \mathbf{I} \\ -\mathbf{M}^{-1}(\hat{\mathbf{K}} + \hat{\mathbf{K}}_g) & -\mathbf{M}^{-1}\hat{\mathbf{C}} \end{bmatrix}, \mathbf{B}_{\mathrm{w}} = \begin{bmatrix} \mathbf{0} & \mathbf{0} \\ \mathbf{M}^{-1}\mathbf{T}_{CG\text{-}e} & -\mathbf{T}_q \end{bmatrix}, \\ &\mathbf{B}_{\mathrm{u}} = \begin{bmatrix} \mathbf{0} & \mathbf{0} & \cdots & \mathbf{0} & \mathbf{0} \\ -\mathbf{M}^{-1}\bar{\mathbf{K}}_{L,1} & -\mathbf{M}^{-1}\bar{\mathbf{C}}_{L,1} & \cdots & -\mathbf{M}^{-1}\bar{\mathbf{K}}_{L,n} & -\mathbf{M}^{-1}\bar{\mathbf{C}}_{L,n} \end{bmatrix}. \end{aligned} \tag{4.14}$$

The vector $\hat{\ddot{\mathbf{q}}}_0^{\mathrm{T}} = \{\hat{\ddot{x}}_0 \quad \hat{\ddot{y}}_0 \quad \hat{\ddot{z}}_0\}^{\mathrm{T}}$ is a unit vector associated with ground accelerations, and $\mathbf{T}_q$ is a matrix such that $\ddot{\mathbf{q}}_0 = \mathbf{T}_q \hat{\ddot{\mathbf{q}}}_0$.

The control input, **u**, can be expressed in feedback form as

$$\mathbf{u} = \underbrace{\mathrm{diag}(\mathbf{\Gamma}_1, \mathbf{\Gamma}_2, \dots, \mathbf{\Gamma}_n)}_{\mathbf{\Gamma}} \mathbf{v}, \tag{4.15}$$

where **Γ** is the block diagonal feedback gain matrix and $\mathbf{v} = \{\mathbf{v}_1^{\mathrm{T}} \; \mathbf{v}_2^{\mathrm{T}} \; \dots \; \mathbf{v}_n^{\mathrm{T}}\}^{\mathrm{T}}$ is the measured output vector of the isolated system which, according to Eq.(4.10), can be written as

$$\mathbf{v} = \mathbf{C}_{\mathrm{v}}\mathbf{x} + \mathbf{D}_{\mathrm{vw}}\mathbf{w} + \mathbf{D}_{\mathrm{vu}}\mathbf{u}, \tag{4.16}$$

with $\mathbf{C}_{\mathrm{v}}$, $\mathbf{D}_{\mathrm{vw}}$, and $\mathbf{D}_{\mathrm{vu}}$ given by

$$\mathbf{C}_{\mathrm{v}} = \begin{bmatrix} \bar{\mathbf{K}}_{q,1} & \mathbf{0} \\ \mathbf{0} & \bar{\mathbf{C}}_{q,1} \\ \vdots & \vdots \\ \bar{\mathbf{K}}_{q,n} & \mathbf{0} \\ \mathbf{0} & \bar{\mathbf{C}}_{q,n} \end{bmatrix},\ \mathbf{D}_{\mathrm{vw}} = \mathbf{0},\ \mathbf{D}_{\mathrm{vu}} = \mathrm{diag}\left(\bar{\mathbf{K}}_{u,1}, \bar{\mathbf{C}}_{u,1}, \ldots, \bar{\mathbf{K}}_{u,n}, \bar{\mathbf{C}}_{u,n}\right). \tag{4.17}$$

The performance output of the isolated system can be expressed as

$$\mathbf{z} = \mathbf{C}_{\mathrm{z}}\mathbf{x} + \mathbf{D}_{\mathrm{zw}}\mathbf{w} + \mathbf{D}_{\mathrm{zu}}\mathbf{u}, \tag{4.18}$$

where $\mathbf{C}_{\mathrm{z}}$, $\mathbf{D}_{\mathrm{zw}}$ and $\mathbf{D}_{\mathrm{zu}}$ are user defined matrices that can be used to specify any performance output that is linearly related to **x**, **w** and **u**. The equivalent control system described by Eqs.(4.13) to (4.18) can be represented in the standard feedback control configuration [86] shown in Figure 4.2, and can thus be used for control gain (i.e., isolator location) optimization and for various analyses based on LTI control theory, as is demonstrated in the rest of this chapter.

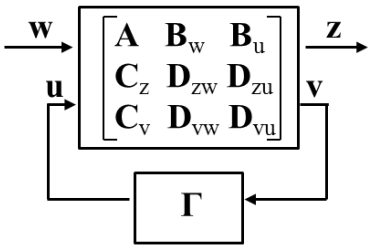

Figure 4.2: Standard Feedback Control Configuration

4.3. H_2/H_∞ Optimization of Isolator Locations using Control Theoretic Framework

Recall that the system is subject to exogenous disturbances from seismic excitations ($\mathbf{q}_0$), from gravity ($\mathbf{F}_{\mathrm{g}}$) and from equivalent disturbance force **F**. The goal of optimization is to select isolator locations that minimize the effects of these three exogenous disturbances on the defined performance output, **z**. The H_2 and H_∞ norms are two metrics commonly used for performance optimization of control systems [86]. They are also used extensively as performance metrics for isolator system design and optimization [6,43,46,48,50,56,57,70,83]. A system's H_2 norm is a measure of the energy of its response to stationary random excitations, while its H_∞ norm measures its worst case response to persistent harmonic inputs [2,6,46,49,53,70]. Following Chapter 3, the effects of $\mathbf{q}_0$ on the isolated system are quantified here using the H_2 norm, because

ground vibration is typically random in nature [30,54]. On the other hand, the effects of **F** are quantified using the H_∞ norm, based on the assumption that **F** represents inertial forces which cause residual (transient) vibration, and the H_∞ norm correlates well with the dominant frequency in the transient vibration response of a vibrating system [2,70]. The effects of gravity are considered implicitly through the equivalent stiffness matrix, $\hat{\mathbf{K}}_g$, which could have destabilizing effects on the isolated system.

Let $\mathbf{z} = [\mathbf{z}_\infty^{\mathrm{T}}, \mathbf{z}_2^{\mathrm{T}}]^{\mathrm{T}}$ and $\mathbf{w} = [\mathbf{w}_\infty^{\mathrm{T}}, \mathbf{w}_2^{\mathrm{T}}]^{\mathrm{T}}$, where $\mathbf{w}_2$, $\mathbf{z}_2$ and $\mathbf{w}_\infty$, $\mathbf{z}_\infty$ denote the input-output pairs associated with the H_2 and H_∞ norms, respectively. Specifically, we let $\mathbf{w}_\infty = \hat{\mathbf{f}}$ and $\mathbf{w}_2 = \ddot{\hat{\mathbf{q}}}_0$. Consequently, the state-space representation of the isolated system, given by Eqs.(4.13) to (4.18), can be re-written as

$$\begin{bmatrix} \dot{\mathbf{x}} \\ \mathbf{z}_\infty \\ \mathbf{z}_2 \\ \mathbf{v} \end{bmatrix} = \begin{bmatrix} \mathbf{A} & \mathbf{B}_{\mathrm{w}\infty} & \mathbf{B}_{\mathrm{w}2} & \mathbf{B}_{\mathrm{u}} \\ \mathbf{C}_{\mathrm{z}\infty} & \mathbf{D}_{\mathrm{zw}\infty} & \mathbf{0} & \mathbf{D}_{\mathrm{zu}\infty} \\ \mathbf{C}_{\mathrm{z}2} & \mathbf{0} & \mathbf{D}_{\mathrm{zw}2} & \mathbf{D}_{\mathrm{zu}2} \\ \mathbf{C}_{\mathrm{v}} & \mathbf{D}_{\mathrm{vw}\infty} & \mathbf{D}_{\mathrm{vw}2} & \mathbf{D}_{\mathrm{vu}} \end{bmatrix} \begin{bmatrix} \mathbf{x} \\ \mathbf{w}_\infty \\ \mathbf{w}_2 \\ \mathbf{u} \end{bmatrix}, \tag{4.19}$$

where it follows from Eqs.(4.14) and (4.17) that

$$\mathbf{B}_{\mathrm{w}\infty} = \begin{bmatrix} \mathbf{0} \\ \mathbf{M}^{-1}\mathbf{T}_{CG\text{-}e} \end{bmatrix},\ \mathbf{B}_{\mathrm{w}2} = \begin{bmatrix} \mathbf{0} \\ -\mathbf{T}_q \end{bmatrix},\ \mathbf{D}_{\mathrm{vw}\infty} = \mathbf{0},\ \mathbf{D}_{\mathrm{vw}2} = \mathbf{0}. \tag{4.20}$$

The **C** and **D** matrices associated with $\mathbf{z}_\infty$ and $\mathbf{z}_2$ can be obtained by appropriately partitioning the user-defined matrices of Eq.(4.18).

Based on the relationship $\mathbf{u} = \boldsymbol{\Gamma}\mathbf{v}$ (from Eq.(4.15)), we can re-write the control input **u** from Eq.(4.19) as

$$\mathbf{u} = (\mathbf{I} - \boldsymbol{\Gamma}\mathbf{D}_{\mathrm{vu}})^{-1}\boldsymbol{\Gamma}(\mathbf{C}_{\mathrm{v}}\mathbf{x} + \mathbf{D}_{\mathrm{vw}\infty}\mathbf{w}_\infty + \mathbf{D}_{\mathrm{vw}2}\mathbf{w}_2), \tag{4.21}$$

For this particular problem, since $\mathbf{D}_{\mathrm{vu}}$ and $\boldsymbol{\Gamma}$ are block diagonal matrices, we get

$$(\mathbf{I} - \boldsymbol{\Gamma}\mathbf{D}_{\mathrm{vu}})^{-1} = \mathrm{diag}\left((\mathbf{I} - \boldsymbol{\Gamma}_{k,i}\bar{\mathbf{K}}_{u,1})^{-1}, (\mathbf{I} - \boldsymbol{\Gamma}_{c,i}\bar{\mathbf{C}}_{u,1})^{-1}, \ldots, (\mathbf{I} - \boldsymbol{\Gamma}_{k,n}\bar{\mathbf{K}}_{u,n})^{-1}, (\mathbf{I} - \boldsymbol{\Gamma}_{c,n}\bar{\mathbf{C}}_{u,n})^{-1}\right), \tag{4.22}$$

Notice that $(\mathbf{I} - \boldsymbol{\Gamma}\mathbf{D}_{\mathrm{vu}})^{-1} = (\mathbf{I} + \boldsymbol{\Gamma}\mathbf{D}_{\mathrm{vu}})$ because

$$
\begin{aligned}
(\mathbf{I}-\boldsymbol{\Gamma}_{c,i}\bar{\mathbf{C}}_{u,i})^{-1} &= \begin{bmatrix} \mathbf{I} & \mathbf{0} \\ -L(\mathbf{a}_i)^{\mathrm{T}}\mathbf{C}_i & \mathbf{I} \end{bmatrix}^{-1} = \begin{bmatrix} \mathbf{I} & \mathbf{0} \\ L(\mathbf{a}_i)^{\mathrm{T}}\mathbf{C}_i & \mathbf{I} \end{bmatrix} = \left(\mathbf{I}+\boldsymbol{\Gamma}_{c,i}\bar{\mathbf{C}}_{u,i}\right), \\
(\mathbf{I}-\boldsymbol{\Gamma}_{k,i}\bar{\mathbf{K}}_{u,i})^{-1} &= \begin{bmatrix} \mathbf{I} & \mathbf{0} \\ -L(\mathbf{a}_i)^{\mathrm{T}}\mathbf{K}_i & \mathbf{I} \end{bmatrix}^{-1} = \begin{bmatrix} \mathbf{I} & \mathbf{0} \\ L(\mathbf{a}_i)^{\mathrm{T}}\mathbf{K}_i & \mathbf{I} \end{bmatrix} = \left(\mathbf{I}+\boldsymbol{\Gamma}_{k,i}\bar{\mathbf{K}}_{u,i}\right).
\end{aligned}
\tag{4.23}
$$

For convenience, we can therefore define

$$
\bar{\boldsymbol{\Gamma}} = \boldsymbol{\Gamma} + \boldsymbol{\Gamma}\mathbf{D}_{\mathrm{vu}}\boldsymbol{\Gamma}. \tag{4.24}
$$

Combining Eq.(4.24) with Eq.(4.21) and substituting the result in Eq.(4.19), we get an equivalent closed loop system given by

$$
\begin{bmatrix} \dot{\mathbf{x}} \\ \mathbf{z}_\infty \\ \mathbf{z}_2 \end{bmatrix} = \begin{bmatrix} \mathbf{A}+\mathbf{B}_{\mathrm{u}}\bar{\boldsymbol{\Gamma}}\mathbf{C}_{\mathrm{v}} & \mathbf{B}_{\mathrm{w}\infty}+\mathbf{B}_{\mathrm{u}}\bar{\boldsymbol{\Gamma}}\mathbf{D}_{\mathrm{vw}\infty} & \mathbf{B}_{\mathrm{w}2}+\mathbf{B}_{\mathrm{u}}\bar{\boldsymbol{\Gamma}}\mathbf{D}_{\mathrm{vw}2} \\ \mathbf{C}_{\mathrm{z}\infty}+\mathbf{D}_{\mathrm{zu}\infty}\bar{\boldsymbol{\Gamma}}\mathbf{C}_{\mathrm{v}} & \mathbf{D}_{\mathrm{zw}\infty}+\mathbf{D}_{\mathrm{zu}\infty}\bar{\boldsymbol{\Gamma}}\mathbf{D}_{\mathrm{vw}\infty} & \mathbf{D}_{\mathrm{zu}\infty}\bar{\boldsymbol{\Gamma}}\mathbf{D}_{\mathrm{vw}2} \\ \mathbf{C}_{\mathrm{z}2}+\mathbf{D}_{\mathrm{zu}2}\bar{\boldsymbol{\Gamma}}\mathbf{C}_{\mathrm{v}} & \mathbf{D}_{\mathrm{zu}2}\bar{\boldsymbol{\Gamma}}\mathbf{D}_{\mathrm{vw}\infty} & \mathbf{D}_{\mathrm{zw}2}+\mathbf{D}_{\mathrm{zu}2}\bar{\boldsymbol{\Gamma}}\mathbf{D}_{\mathrm{vw}2} \end{bmatrix} \begin{bmatrix} \mathbf{x} \\ \mathbf{w}_\infty \\ \mathbf{w}_2 \end{bmatrix}. \tag{4.25}
$$

Accordingly, we can define two transfer functions: $\mathbf{G}_{\mathrm{z2w2}}$, from $\mathbf{w}_2$ to $\mathbf{z}_2$, and $\mathbf{G}_{\mathrm{z}\infty\mathrm{w}\infty}$, from $\mathbf{w}_\infty$ to $\mathbf{z}_\infty$, as

$$
\mathbf{G}_{\mathrm{z2w2}} = \left[\begin{array}{c|c} \mathbf{A}+\mathbf{B}_{\mathrm{u}}\bar{\boldsymbol{\Gamma}}\mathbf{C}_{\mathrm{v}} & \mathbf{B}_{\mathrm{w}2}+\mathbf{B}_{\mathrm{u}}\bar{\boldsymbol{\Gamma}}\mathbf{D}_{\mathrm{vw}2} \\ \hline \mathbf{C}_{\mathrm{z}2}+\mathbf{D}_{\mathrm{zu}2}\bar{\boldsymbol{\Gamma}}\mathbf{C}_{\mathrm{v}} & \mathbf{D}_{\mathrm{zw}2}+\mathbf{D}_{\mathrm{zu}2}\bar{\boldsymbol{\Gamma}}\mathbf{D}_{\mathrm{vw}2} \end{array}\right], \tag{4.26}
$$

$$
\mathbf{G}_{\mathrm{z}\infty\mathrm{w}\infty} = \left[\begin{array}{c|c} \mathbf{A}+\mathbf{B}_{\mathrm{u}}\bar{\boldsymbol{\Gamma}}\mathbf{C}_{\mathrm{v}} & \mathbf{B}_{\mathrm{w}\infty}+\mathbf{B}_{\mathrm{u}}\bar{\boldsymbol{\Gamma}}\mathbf{D}_{\mathrm{vw}\infty} \\ \hline \mathbf{C}_{\mathrm{z}\infty}+\mathbf{D}_{\mathrm{zu}\infty}\bar{\boldsymbol{\Gamma}}\mathbf{C}_{\mathrm{v}} & \mathbf{D}_{\mathrm{zw}\infty}+\mathbf{D}_{\mathrm{zu}\infty}\bar{\boldsymbol{\Gamma}}\mathbf{D}_{\mathrm{vw}\infty} \end{array}\right]. \tag{4.27}
$$

The H_2 and H_∞ norms of $\mathbf{G}_{\mathrm{z2w2}}$ and $\mathbf{G}_{\mathrm{z}\infty\mathrm{w}\infty}$ are respectively given by

$$
\left\|\mathbf{G}_{\mathrm{z2w2}}\right\|_2 = \sqrt{\frac{1}{2\pi}\int_{-\infty}^{\infty}\mathrm{trace}\left[\mathbf{G}_{\mathrm{z2w2}}^{\mathrm{H}}(j\omega)\mathbf{G}_{\mathrm{z2w2}}(j\omega)\right]d\omega}, \tag{4.28}
$$

$$
\left\|\mathbf{G}_{\mathrm{z}\infty\mathrm{w}\infty}\right\|_\infty = \sup_{\omega}\left(\sigma_{\max}\left(\mathbf{G}_{\mathrm{z}\infty\mathrm{w}\infty}(j\omega)\right)\right), \tag{4.29}
$$

where j and ω respectively represent the unit imaginary number and frequencies in rad/s; the superscript H denotes the Hermitian transpose and $\sigma_{\max}$ denotes the maximum singular value. Consequently, the problem of optimally locating isolators to simultaneously minimize the responses of the isolated system to $\mathbf{q}_0$ (or its derivatives) and $\mathbf{F}$ can be formally defined as the mixed H_2/H_∞ objective:

$$\boldsymbol{\Gamma} = \text{sol}\begin{cases} \text{Minimize:} & \left\|\mathbf{G}_{z2w2}\right\|_2 \\ \text{Over:} & \boldsymbol{\Gamma} \in \boldsymbol{\Phi} \\ \text{Subject to:} & \left\|\mathbf{G}_{z\infty w\infty}\right\|_\infty < \gamma_\infty \end{cases}, \tag{4.30}$$

where $\boldsymbol{\Phi}$ is the admissible domain for $\boldsymbol{\Gamma}$, and γ_∞ is an upper bound specified for $\|\mathbf{G}_{z\infty w\infty}\|_\infty$. Note that in order for the optimization problem to be well posed, $\mathbf{G}_{z2w2}$ must have a finite H_2 norm [53]. The implication is that $\mathbf{D}_{zw2} + \mathbf{D}_{zu2}\bar{\boldsymbol{\Gamma}}\mathbf{D}_{vw2} = \mathbf{0}$ for all $\boldsymbol{\Gamma} \in \boldsymbol{\Phi}$, which is trivially satisfied for the isolator placement problem considered in this chapter because $\mathbf{D}_{vw2}$ = **0** and $\mathbf{D}_{zw2}$ = **0**, assuming, as is typical, that $\mathbf{z}_2$ is defined using absolute quantities (e.g., $\ddot{\mathbf{q}}$, rather than $\ddot{\mathbf{q}} - \ddot{\mathbf{q}}_0$).

The following two theorems establish the conditions for the existence of a solution to Eq.(4.30). Proofs for these theorems are standard, and are therefore omitted here. The interested reader is referred to a standard robust controls textbook (e.g., [87]) for a detailed derivation of the proofs.

THEOREM 1. For a given $\boldsymbol{\Gamma} \in \boldsymbol{\Phi}$, $\|\mathbf{G}_{z2w2}\|_2 < \gamma_2$ if and only if $\exists\ \mathbf{P}_2 = \mathbf{P}_2{}^{\mathrm{T}} > 0$ such that

$$\mathbf{M}_2(\mathbf{P}_2, \bar{\boldsymbol{\Gamma}}) \triangleq \begin{bmatrix} \mathbf{P}_2(\mathbf{A} + \mathbf{B}_u\bar{\boldsymbol{\Gamma}}\mathbf{C}_v) + (\mathbf{A} + \mathbf{B}_u\bar{\boldsymbol{\Gamma}}\mathbf{C}_v)^{\mathrm{T}}\mathbf{P}_2 & (\mathbf{C}_{z2} + \mathbf{D}_{zu2}\bar{\boldsymbol{\Gamma}}\mathbf{C}_v)^{\mathrm{T}} \\ (\mathbf{C}_{z2} + \mathbf{D}_{zu2}\bar{\boldsymbol{\Gamma}}\mathbf{C}_v) & -\mathbf{I} \end{bmatrix} < 0, \tag{4.31}$$

$$\text{trace}\left\{(\mathbf{B}_{w2} + \mathbf{B}_u\bar{\boldsymbol{\Gamma}}\mathbf{D}_{vw2})^{\mathrm{T}}\mathbf{P}_2(\mathbf{B}_{w2} + \mathbf{B}_u\bar{\boldsymbol{\Gamma}}\mathbf{D}_{vw2})\right\} < \gamma_2^2. \tag{4.32}$$

We remark that Eq.(4.32) simplifies in the problem considered here, for which $\mathbf{D}_{vw2}$ = **0**. In particular the left-hand side of the inequality becomes trace$\{\mathbf{B}_{w2}{}^{\mathrm{T}}\mathbf{P}_2\mathbf{B}_{w2}\}$. In order to simplify the presentation, we will assume this simplification henceforth.

THEOREM 2. For a given $\boldsymbol{\Gamma} \in \boldsymbol{\Phi}$, $\|\mathbf{G}_{z\infty w\infty}\| < \gamma_\infty$ if and only if $\exists\ \mathbf{P}_\infty = \mathbf{P}_\infty{}^{\mathrm{T}} > 0$ such that

$$\mathbf{M}_\infty(\mathbf{P}_\infty, \bar{\boldsymbol{\Gamma}}) \triangleq$$
$$\begin{bmatrix} \mathbf{P}_\infty(\mathbf{A} + \mathbf{B}_u\bar{\boldsymbol{\Gamma}}\mathbf{C}_v) + (\mathbf{A} + \mathbf{B}_u\bar{\boldsymbol{\Gamma}}\mathbf{C}_v)^{\mathrm{T}}\mathbf{P}_\infty & \mathbf{P}_\infty(\mathbf{B}_{w\infty} + \mathbf{B}_u\bar{\boldsymbol{\Gamma}}\mathbf{D}_{vw\infty}) & (\mathbf{C}_{z\infty} + \mathbf{D}_{zu\infty}\bar{\boldsymbol{\Gamma}}\mathbf{C}_v)^{\mathrm{T}} \\ (\mathbf{B}_{w\infty} + \mathbf{B}_u\bar{\boldsymbol{\Gamma}}\mathbf{D}_{vw\infty})^{\mathrm{T}}\mathbf{P}_\infty & -\gamma_\infty\mathbf{I} & (\mathbf{D}_{zw\infty} + \mathbf{D}_{zu\infty}\bar{\boldsymbol{\Gamma}}\mathbf{D}_{vw\infty})^{\mathrm{T}} \\ (\mathbf{C}_z + \mathbf{D}_{zu\infty}\bar{\boldsymbol{\Gamma}}\mathbf{C}_v) & (\mathbf{D}_{zw\infty} + \mathbf{D}_{zu\infty}\bar{\boldsymbol{\Gamma}}\mathbf{D}_{vw\infty}) & -\gamma_\infty\mathbf{I} \end{bmatrix} < 0. \tag{4.33}$$

Using the inequality relationships of the above theorems, the optimization problem in Eq.(4.30) is equivalent to the following problem:

$$\boldsymbol{\Gamma} = \text{sol}\begin{cases} \text{Minimize:} & \text{trace}\left\{\mathbf{C}_{z2}\mathbf{P}_2\mathbf{C}_{z2}^{\mathrm{T}}\right\} \\ \text{Over:} & \left\{\mathbf{P}_2, \mathbf{P}_\infty, \boldsymbol{\Gamma}\right\} \in \mathbf{D} \\ \text{Subject to:} & (4.31), (4.33) \end{cases}. \tag{4.34}$$

where $\mathbf{D} = \mathbf{H}\times\mathbf{H}\times\boldsymbol{\Phi}$, and $\mathbf{H}$ is the set of all (Hermitian) positive definite matrices.

Notice that the optimization in Eq.(4.34) is nonconvex. This non-convexity arises due to the existence of bilinear matrix products in $\mathbf{M}_2(\mathbf{P}_2, \bar{\boldsymbol{\Gamma}})$ and $\mathbf{M}_\infty(\mathbf{P}_\infty, \bar{\boldsymbol{\Gamma}})$ in Eqs.(4.31) and (4.33), as well as the quadratic relationship between $\bar{\boldsymbol{\Gamma}}$ and $\boldsymbol{\Gamma}$ in Eq.(4.24). Therefore, in order to obtain the optimal solution of Eq.(4.34), a non-convex optimization algorithm is employed. The optimization algorithm makes the use of iterative convex over-bounding techniques (i.e., "convexification" techniques) [83-86]. It requires the establishment of an initial parameter set, denoted as $\{\mathbf{P}_{20}, \mathbf{P}_{\infty 0}, \boldsymbol{\Gamma}_0\}$, which is feasible; i.e., which satisfies Eqs.(4.31) and (4.33). It then recursively solves for a sequence of feasible parameters (or "design points"), denoted as $\{\mathbf{P}_{2k}, \mathbf{P}_{\infty k}, \boldsymbol{\Gamma}_k\}$, where the subscript k refers to the k^{th} recursion. It is shown in the papers [3, 83-86] that the set of design points (i.e.,$\{\mathbf{P}_{2(k+1)}, \mathbf{P}_{\infty(k+1)}, \boldsymbol{\Gamma}_{(k+1)}\}$) for iteration k+1 is guaranteed to produce a feasible solution which has incrementally better performance than the those of iteration k. Accordingly, the optimization objective decreases monotonically with each iteration. Therefore, if the objective is bounded from below (which the H_2 objective is known to be), then the algorithm is guaranteed to converge to a local minimum. Note, the algorithm is not guaranteed to converge in polynomial time, and the attained minimum is only guaranteed to be local. The formulation of the algorithm involves a significant amount of algebraic manipulation, on the matrices in Eqs.(4.31) and (4.33), as detailed in [3, 83-86].

4.4. Illustrative Examples

This section presents examples to demonstrate how the proposed control theoretic framework in this chapter can be used to optimize and analyze the placement of isolators. All examples are based on the 5-axis ultra-precision machine tool shown in Figure 4.3, which was employed in Chapters 2 and 3. For the analysis of the generalized system, we focus on all planes of the machine. Table 4.1 summarizes the inertia, damping and stiffness parameters of the machine's isolation system, while Table 4.2 provides the position vectors of the inertial forces generated by the x, y and z axes of the machine (denoted by e = 1, 2 and 3, respectively). Table

4.3 lists the nominal locations for the four isolators of the machine. Notice that the isolators have been placed symmetrically in an *x*-*y* plane that passes through the CG of the isolated system. As discussed in Chapter 1, this particular arrangement of isolators is widely recommended in industry and academic literature because it decouples all six vibration modes of the isolated base [29,31,55] thus simplifying the isolator placement problem. The examples presented in this section will show how the proposed control theoretic framework can help uncover much more effective isolator arrangements, based on the assumption that each isolator can be placed within ± 200 mm along the *x*, *y* and *z* directions relative to its nominal position.

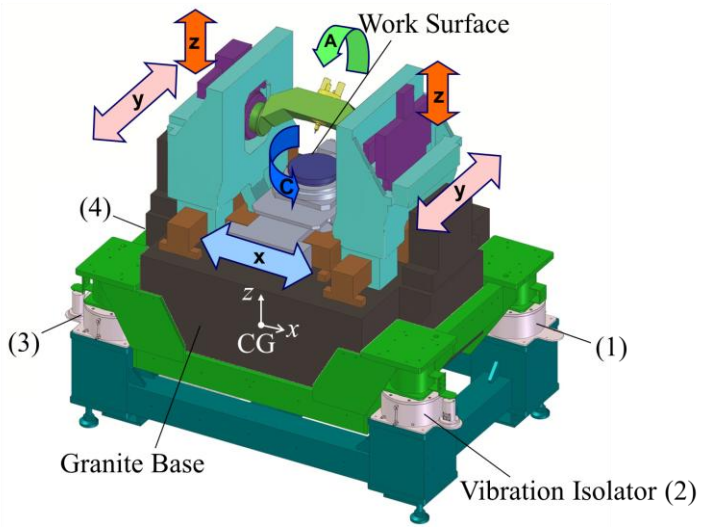

Figure 4.3: Schematic of Mori Seiki's NN1000 DCG 5-Axis Ultra-Precision Machine Tool used for Simulations and Experiments

Parameter	Value	Parameter	Value
m [kg]	1,182	$k_{x,i} = k_{y,i}$ [N/m]	220,000
I_x [kg-m^2]	96	$k_{z,i}$ [N/m]	300,000
I_y [kg-m^2]	219	$c_{x,i} = c_{y,i}$ [kg/s]	2,419
I_z [kg-m^2]	179	$c_{z,i}$ [kg/s]	2,729

Table 4.1: Inertia, Damping and Stiffness Parameters of NN1000's Isolation System. (Note: All Isolators have the Same Damping and Stiffness Properties)

Position ($\mathbf{r}_e$)	*x-axis* (e =1)	*y-axis* (e =2)	*z-axis* (e =3)
$r_{x,e}$ [mm]	*	0	0
$r_{y,e}$ [mm]	0	*	70
$r_{z,e}$ [mm]	211	425	*

Table 4.2: Position of Inertial Forces Generated by *x*, *y* and *z* axes of NN1000. The Asterisk Indicates a Component of the Position Vector that is Irrelevant because it does not Create Moments. Note that even though $r_{y,3}$ is a Variable Ranging from −70 mm to 70 mm, its Largest Value (i.e., $r_{y,3}$ = 70 mm) has been Selected.

Location/Orientation	**Isolator Number**			
	i =1	i =2	i =3	i =4
$a_{x,i}$ [mm]	500	500	−500	−500
$a_{y,i}$ [mm]	295	−295	−295	295
$a_{z,i}$ [mm]	0	0	0	0
$\alpha_i = \beta_i = \gamma_i$	0	0	0	0

Table 4.3: Nominal Locations/Orientations of Isolators of NN1000. Note: Isolators are Placed to Achieve Modal Decoupling (i.e., $a_{x,i}$ and $a_{y,i}$ are symmetric with $a_{z,i}$ = 0)

4.4.1. Isolator Placement for Residual Vibration Minimization

Example 1: Minimization of Rocking Vibration due to Motion of y-Axis

This example re-visits the case studied in Chapters 2 and 3 where the nominal $a_{x,i}$ and $a_{y,i}$ locations of all four isolators were left unchanged, and the height $a_{z,i} = a_z$ of the plane containing the isolators was optimized to minimize accelerations in the θ_x direction, caused by the motion of the machine's massive *y*-axis located at $\mathbf{r}_2$ described in Table 4.2. Gravity was not considered in Chapters 2 and 3; therefore, for the sake of consistency, it is omitted in this example. According to the proposed control framework, the following definitions are made:

$$\begin{aligned}
&\mathbf{T}_q = \mathbf{0},\ \mathbf{T}_{e=2} = \mathrm{diag}(\{0 \quad 1 \quad 0\}),\ \mathbf{T}_{e=1} = \mathbf{T}_{e=3} = \mathbf{0},\\
&\mathbf{C}_{z\infty} = \mathbf{T}_{out}\left[-\mathbf{M}^{-1}\hat{\mathbf{K}} \quad -\mathbf{M}^{-1}\hat{\mathbf{C}}\right],\ \mathbf{D}_{zw\infty} = \mathbf{T}_{out}\mathbf{M}^{-1}\mathbf{T}_{CG\text{-}e},\\
&\mathbf{D}_{zu\infty} = \mathbf{T}_{out}\left[-\mathbf{M}^{-1}\bar{\mathbf{K}}_{L,1} \quad -\mathbf{M}^{-1}\bar{\mathbf{C}}_{L,1} \quad \cdots \quad -\mathbf{M}^{-1}\bar{\mathbf{K}}_{L,n} \quad -\mathbf{M}^{-1}\bar{\mathbf{C}}_{L,n}\right],
\end{aligned} \tag{4.35}$$

where $\mathbf{T}_{out}$ = {0 0 0 1 0 0} in order to select the θ_x acceleration. The optimization is performed using MATLAB's® *hinfstruct* command, which performs H_∞ optimization for a structured feedback gain matrix. Constraints are added to *hinfstruct* to fix $a_{x,i}$ and $a_{y,i}$ at their nominal values, as well as to place the ± 200 mm bound on a_z. Using the nominal a_z (i.e., a_z = 0) as the initial condition, a_z^* = −116.8 mm (i.e., isolators are located 116.8 mm below CG) is returned as

the optimal height. For this simple single variable optimization problem, $\|\mathbf{G}_{z\infty w\infty}\|_\infty$ can easily be plotted as a function of a_z, as shown in Figure 4.4, to prove that −116.8 mm is indeed a local minimum. Figure 4.5 compares the simulated and experimentally measured frequency response functions (FRFs) for $|G_{z\infty w\infty}|$, showing significant reductions in $\|G_{z\infty w\infty}\|_\infty$ using a_z = −116 mm compared with the nominal placement with a_z = 0. Figure 4.6 shows the position error measured from the *y*-axis encoder of the machine in response to a motion command, showing a five times reduction in RMS errors as a result of implementing a_z = −116 mm on the machine (see also Chapters 2 and 3). Note that a_z^* changes slightly to – 105.7 mm and $\|\mathbf{G}_{z\infty w\infty}\|_\infty$ = 9.4 (mrad/s^2)/N instead of 9.3 (mrad/s^2)/N if gravity is included in the optimization.

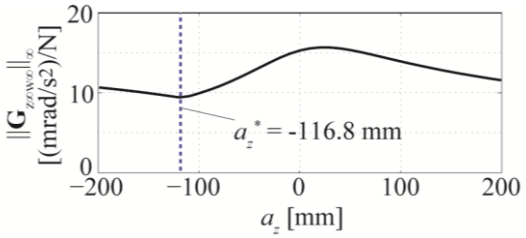

Figure 4.4: Plot of $\|\mathbf{G}_{z\infty w\infty}\|_\infty$ vs. a_z Showing Local Optimum at a_z^* = −116.8 mm

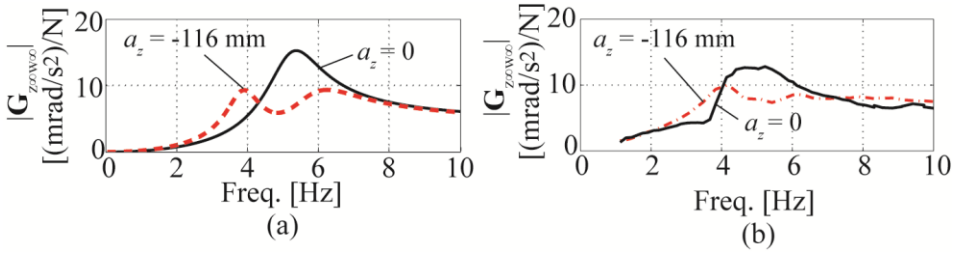

Figure 4.5: FRFs of NN1000 Obtained from (a) Simulations and (b) Experiments for a_z = 0 and a_z = −116 mm

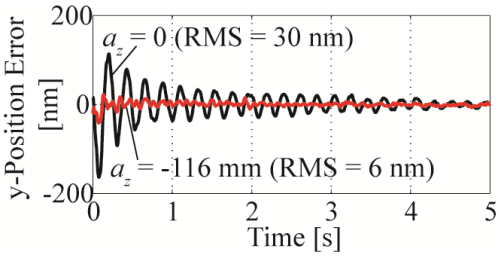

Figure 4.6: Position Error Measured from Encoder for a_z = 0 and a_z = −116 mm during Motion of *y*-axis from Rest to 1000 mm/min. Position Error is due to Residual Vibration

Example 2: Multivariable Isolator Placement to Minimize Rocking Vibration due to Motion of x, y and z Axes.

The author no longer has access to the NN1000 machine for further experiments. Therefore, this example explores two alternative placement cases using simulations.

Case 1 (Symmetric Case): Isolators are constrained to lie symmetrically in the same *x*-*y* plane but their *x*, *y* and *z* locations are free to change within the specified (± 200 mm) bounds.

Case 2 (Unrestricted Case): Isolator positions are unrestricted, as long as they each lie within the specified (± 200 mm) bounds.

In both cases, the objective in Example 1 has been extended to also consider the inertial forces from the *x* and *z* axes, in addition to that from the *y* axis. Furthermore, the effect of gravity is incorporated and $\ddot{\boldsymbol{\theta}} = \left\{ \ddot{\theta}_x \quad \ddot{\theta}_y \quad \ddot{\theta}_z \right\}^{\mathrm{T}}$ is considered as the response of interest. Accordingly, the following definitions are made:

$$\begin{aligned} &\mathbf{C}_{z\infty} = \mathbf{T}_{out} \left[-\mathbf{M}^{-1}(\hat{\mathbf{K}} + \hat{\mathbf{K}}_g) \quad -\mathbf{M}^{-1}\hat{\mathbf{C}} \right], \\ &\mathbf{T}_q = \mathbf{0},\ \mathbf{T}_{e=1} = \mathrm{diag}(\{1 \quad 0 \quad 0\}),\ \mathbf{T}_{e=2} = \mathrm{diag}(\{0 \quad 1 \quad 0\}),\ \mathbf{T}_{e=3} = \mathrm{diag}(\{0 \quad 0 \quad 1\}); \end{aligned} \tag{4.36}$$

$\mathbf{D}_{zw\infty}$ and $\mathbf{D}_{zu\infty}$ are the same as in Eq.(4.35) but $\mathbf{T}_{out}$ = [**0** **I**]. Table 4.4 summarizes the optimal isolator locations while Figure 4.7 compares the FRF magnitudes from each input to each output for Cases 1 and 2 and the nominal case. One observes that in both Case 1 and the nominal case, the machine experiences θ_x accelerations due to F_y and F_z, as well as θ_y accelerations due to F_x. However, the θ_x accelerations due to F_y are the most dominant of the responses because of the large moment arm of the *y*-axis inertial force and the relatively small value of I_x. Compared to the nominal case, Case 1 achieves a 47% reduction in the peak of the F_y-induced θ_x accelerations by spreading $a_{y,i}$ as far as possible, and by placing the plane of the isolators below the CG, thus exploiting the benefits of mode coupling. Case 2 further reduces the F_y-induced θ_x acceleration peak by 12%, compared to Case 1, by creating mode coupling in directions that cannot be accessed by Case 1 due to its symmetry constraints. Note that, because of the imposed symmetry constraints, the mode coupling in Case 1 involves only one curve veering event, close to $a_{z,i} = 0$, similar to those already studied in Chapters 2 and 3. However, because Case 2 exploits mode coupling in many directions, there could be several instances of curve veering and mode

localization at various combinations of $\mathbf{a}_i$ [62,64,88] which could provide more opportunities for critical configurations.

As mentioned in Section 4.3, the H_∞ norm is a measure of the worst-case response of a system. For a multivariable system, the worst-case response entails a worst-case frequency and associated worst-case input and output directions at that frequency. Figure 4.7 gives some hints regarding the worst-case response but a more accurate picture can be obtained by computing the singular value decomposition (SVD) of the optimized system [86]. Table 4.5 summarizes the worst-case frequencies, and input/output directions, as well as the corresponding values of $\|\mathbf{G}_{z\infty w\infty}\|_\infty$ for the optimized systems from Cases 1 and 2 and the nominal case. One observes that the worst-case input and output directions are not always perfectly aligned with the *y*-axis force and the θ_x accelerations, respectively; though they are very close, as one would expect.

Case 1	$i=1$	$i=2$	$i=3$	$i=4$
$a_{x,i}$ [mm]	500	500	−500	−500
$a_{y,i}$ [mm]	495	−495	−495	495
$a_{z,i}$ [mm]	−200	−200	−200	−200
Case 2	$i=1$	$i=2$	$i=3$	$i=4$
$a_{x,i}$ [mm]	300	700	−700	−700
$a_{y,i}$ [mm]	495	−495	−109	495
$a_{z,i}$ [mm]	−200	−200	−200	−200

Table 4.4: Optimal Isolator Locations for Cases 1 and 2 of Example 2

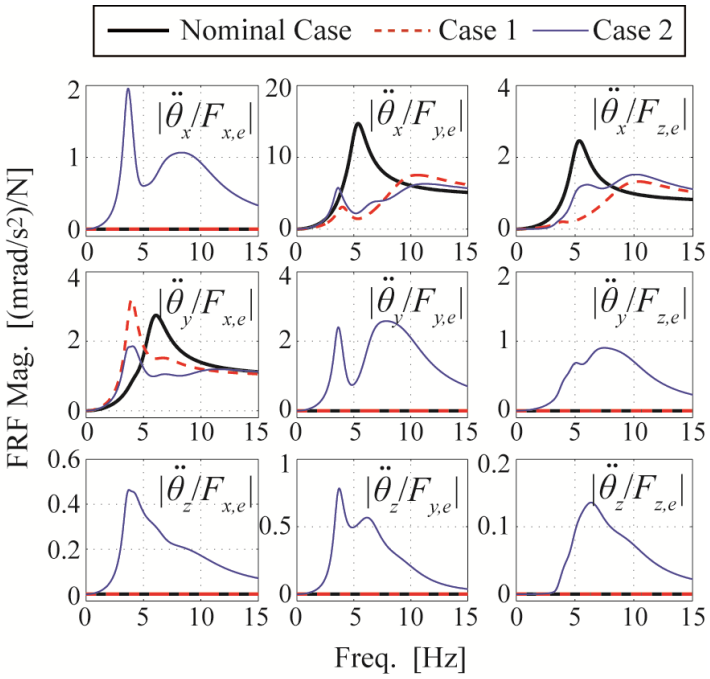

Figure 4.7: FRF Magnitudes from the Inputs to Outputs for Cases 1 and 2 of Example 2 Compared with the Nominal Case

	Worst-case Frequency [Hz]	Worst-case Input direction	Worst-case Output direction	Max. Singular Value [(mrad/s^2)/N]
Nominal	5.39	[0; 0.99; 0.16]	[1; 0; 0]	14.9
Case 1	10.79	[0; 0.99; 0.17]	[1; 0; 0]	7.6
Case 2	3.61	[0.36; 0.93; 0.02]	[0.90; 0.42; 0.13]	6.7

Table 4.5: Worst-case Frequencies, Input/Output Directions and Magnitudes of $\|\mathbf{G}_{z\infty w\infty}\|_\infty$ for the Optimized Systems from Cases 1 and 2 of Example 2, Compared with those of the Nominal Case

4.4.2. Isolator Placement for Minimization of Residual Vibration and Transmissibility

UPM machines often experience disturbances from ground motion in combination with those from inertial forces. As mentioned in Chapter 1, there is a well-known tradeoff between rejecting these two sources of disturbances [26,34]. The example presented in this section explores optimal isolator placement as a means to minimize the response of the isolated system to both sources of vibration, thus reducing the tradeoff.

Example 3: Mixed H2/H∞ Optimization of Isolator Locations

In this example, we consider again the two cases discussed in Example 2 above. However, we assume that the focus is to minimize vibration (accelerations) at the work surface of the isolated machine, located at $\mathbf{r}_w = \{0\ 0\ 300\}^T$ mm from the CG, stemming from the motion of the

machine's axes as well as from ground vibration; gravity is also factored in. The magnitude of ground excitations in the vertical direction is assumed to be twice of those in the horizontal directions, based on insights from practice [14,29]. Accordingly, for the H_2 objective,

$$\mathbf{T}_q = \begin{bmatrix} \text{diag}(\{1 \quad 1 \quad 2\}) \\ \mathbf{0} \end{bmatrix}. \tag{4.37}$$

The user-defined matrices: $\mathbf{C}_{z\infty} = \mathbf{C}_{z2}$, $\mathbf{D}_{zu\infty} = \mathbf{D}_{zu2}$ and $\mathbf{D}_{zw\infty}$ are the same as in Eq.(4.35), except that $\mathbf{T}_{out} = [\mathbf{I} \;\; L(\mathbf{r}_w)]$, while $\mathbf{D}_{zw2} = \mathbf{0}$. Note that $\mathbf{T}_{e=1}$, $\mathbf{T}_{e=2}$ and $\mathbf{T}_{e=3}$ retain their definitions given in Eq.(4.36).

MATLAB does not have a command for mixed H_2/H_∞ optimization of a structured feedback gain matrix. Therefore, the mixed H_2/H_∞ optimization algorithm detailed in [3,83-86] is implemented in MATLAB. Figure 4.8 shows the Pareto curves for Cases 1 and 2, describing the tradeoff between the obtained upper bound (γ_2) on $\|\mathbf{G}_{z2w2}\|_2$ and the imposed upper bound (γ_∞) on $\|\mathbf{G}_{z\infty w\infty}\|_\infty$, in comparison with the fixed γ_2 = 18.6 $\text{Hz}^{0.5}$ and γ_∞ = 6.1 (mm/s^2)/N of the nominal case. Notice the huge reductions in the level of tradeoff required in rejecting seismic and inertial force disturbances that have been facilitated by optimal placement of the isolators. For example, Case 1 achieves a minimum γ_2 value of 17.5 $\text{Hz}^{0.5}$ at a γ_∞ value of 4.8 (mm/s^2)/N (which are respectively 6% and 21% lower than the γ_2 and γ_∞ values of the nominal case); Case 2 achieves a minimum γ_2 value of 16.6 $\text{Hz}^{0.5}$ at a γ_∞ value of 3.9 (mm/s^2)/N (which are respectively 11% and 36% lower than the γ_2 and γ_∞ values of the nominal case).

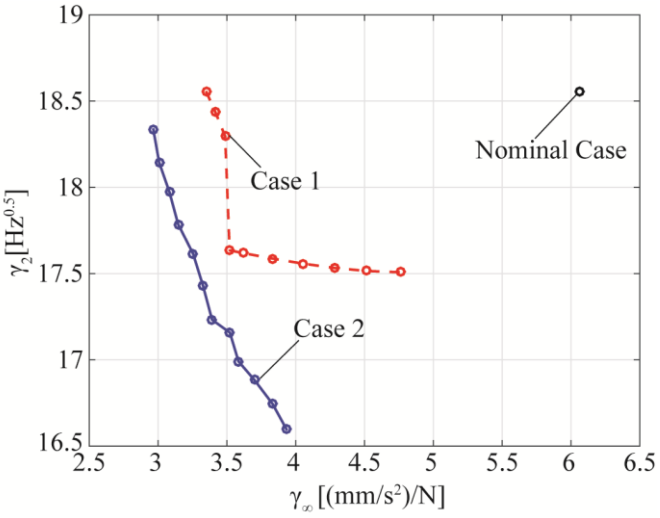

Figure 4.8: Pareto Curves of Cases 1 and 2 Compared with the Fixed γ_2 and γ_∞ Values of the Nominal Case

4.4.3. Gravitational Stability Analysis based on Control Framework

So far, nothing has been said about the gravitational stability of the optimal solutions presented in the preceding examples. Theoretically, all solutions to H_2 and H_∞ optimal control problems are guaranteed to be stable [86]. Therefore, the optimal results discussed in the preceding examples yield gravitationally stable isolation systems. However, one may wonder about relative stability – i.e., whether the optimal solutions compromise stability compared to the nominal case. Another concern may be the robustness of the optimal solutions in the presence of uncertain system parameters (e.g., the location, stiffness or damping of isolators). Two examples are presented in this section to demonstrate how LTI control theory, applied within the context of the proposed framework, can be used to gain deeper insights into questions such as the relative and robust stability of optimal solutions.

Example 4: Relative Stability

One measure of relative stability for a closed loop LTI system is its stability degree (α) defined as

$$\alpha = -\max_i \operatorname{Re} \lambda_i \left(\mathbf{A}_{\text{cl}} \right), \tag{4.38}$$

where $\lambda_i(\mathbf{A}_{\text{cl}})$ represents the eigenvalues of $\mathbf{A}_{\text{cl}}$, the state coefficient matrix of the closed loop system which, in the context of this chapter, is given by

$$\mathbf{A}_{\text{cl}} = \mathbf{A} + \mathbf{B}_{\text{u}} \bar{\mathbf{\Gamma}} \mathbf{C}_{\text{v}}. \tag{4.39}$$

Notice that α represents the slowest decay rate of all the poles of the closed loop system. Figure 4.9 (a) shows the pole maps of the optimal solutions to Cases 1 and 2 presented in Example 2 in comparison with that of the nominal case. Observe that while α = 4 rad/s for the nominal case, it is 3.2 rad/s and 2.7 rad/s for Cases 1 and 2, respectively, indicating losses in relative stability due to the optimal isolator placements.

If loss of relative stability is undesirable, α can be imposed as a constraint on the optimization using (for instance) the *MinDecay* functionality of the *hinfstruct* command in MATLAB. Figure 4.9 (b) shows the pole map obtained when the optimization of Cases 1 and 2 are re-run with *MinDecay* = α = 4 rad/s set as a constraint; Cases 1 and 2 are no longer less stable relative to the nominal case. Tables 4.6 and 4.7 show the changes in the results presented in

Tables 4.4 and 4.5, respectively, when the α = 4 rad/s stability constraint is added. Though $\|\mathbf{G}_{z\infty w\infty}\|_\infty$ increases a bit for Cases 1 and 2 due to the addition of the stability constraint, the $\|\mathbf{G}_{z\infty w\infty}\|_\infty$ values for Cases 1 and 2 are still 40% and 52% better, respectively, than the $\|\mathbf{G}_{z\infty w\infty}\|_\infty$ = 14.9 (mrad/s^2)/N value of the nominal case.

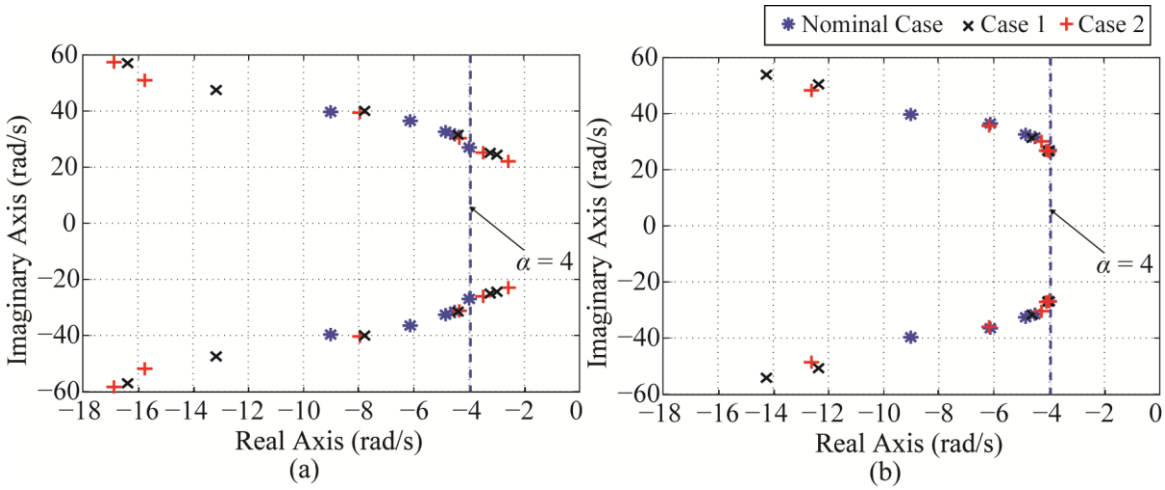

Figure 4.9: Pole Locations of Cases 1 and 2 for Optimal Solutions (of Example 2) and Nominal Case: (a) without Stability Constraints and (b) with α = 4 rad/s Constraint Imposed

Case 1	i =1	i =2	i =3	i =4
$a_{x,i}$ [mm]	578	578	−578	−578
$a_{y,i}$ [mm]	495	−495	−495	495
$a_{z,i}$ [mm]	−68	−68	−68	−68
Case 2	i =1	i =2	i =3	i =4
$a_{x,i}$ [mm]	376	700	−578	−700
$a_{y,i}$ [mm]	95	−495	−296	495
$a_{z,i}$ [mm]	−200	133	−200	200

Table 4.6: Optimal Isolator Locations for Cases 1 and 2 Studied in Example 2 (with α = 4 rad/s Constraint Imposed)

	Worst-case Frequency [Hz]	Worst-case Input direction	Worst-case Output direction	Max. Singular Value [(mrad/s^2)/N]
Case 1	9.7	[0; 0.98; 0.17]	[1; 0; 0]	8.9
Case 2	5.7	[0.25; 0.89; 0.39]	[0.84; 0.54; 0.06]	7.2

Table 4.7: Worst-Case Frequencies, Input/Output Directions and Magnitudes of $\|\mathbf{G}_{z\infty w\infty}\|_\infty$ for the Optimized Systems from Cases 1 and 2 in Example 2 (with α = 4 rad/s Constraint Imposed)

Example 5: Robust Stability

We have so far assumed that the isolation system parameters are known exactly, and that the isolators are placed precisely at their optimal locations. However, in reality, there is some uncertainty in system parameters (especially in the stiffness and damping coefficients of isolators) and it is difficult to position the isolators precisely. In this example, we demonstrate how LTI control theory can be used within the context of the proposed framework to account for uncertainty in isolator placement – the same approach can be used to analyze or design for uncertainties in stiffness and damping parameters.

In the context of Example 4, let us assume that, after placement, the actual locations of the isolators, $\hat{\mathbf{a}}_i$, are given by

$$\hat{\mathbf{a}}_i = \mathbf{a}_i(1 + p_i\delta_i). \tag{4.40}$$

For i = 1,…4, $\mathbf{a}_i$ represents the desired isolator locations, which for the nominal case is given in Table 4.3 and for Cases 1 and 2 are presented in Table 4.4 (without the α = 4 rad/s constraint) and in Table 4.6 (with the α = 4 rad/s constraint imposed); δ_i is a real-valued normalized perturbation variable such that $|\delta_i| \leq 1$, and p_i represents a scaling factor applied to δ_i to indicate the upper and lower limits of uncertainty in $\hat{\mathbf{a}}_i$. For example, p_i = 0.2 indicates an uncertainty of at most ±20% in $\hat{\mathbf{a}}_i$.

A powerful tool from LTI control theory, known as μ-analysis, can be used to determine p_{max}, the maximum value of p_i, beyond which the isolated system will become unstable due to the uncertainty in $\hat{\mathbf{a}}_i$. Details of μ-analysis can be found in any standard robust control text book (e.g., [86]). μ-analysis entails the determination of $\mathbf{M}$ and $\boldsymbol{\Delta}$ matrices for the uncertain system, where $\mathbf{M}$ is a portion of the closed loop dynamics of the isolation system associated with the uncertain parameters and $\boldsymbol{\Delta}$ is a structured matrix containing δ_i such that $\|\boldsymbol{\Delta}\|_\infty \leq 1$. With $\mathbf{M}$ and $\boldsymbol{\Delta}$ determined, a variable μ, given by the expression

$$\mu \triangleq \left[\min_{\boldsymbol{\Delta}} \left\{ \sigma_{\max}(\boldsymbol{\Delta}) \mid \det(\mathbf{I} - \mathbf{M}\boldsymbol{\Delta}) = 0 \text{ for all structured } \boldsymbol{\Delta} \right\} \right]^{-1}, \tag{4.41}$$

can be calculated, where $\sigma_{\max}(\boldsymbol{\Delta})$ represents the maximum singular value of $\boldsymbol{\Delta}$. Accordingly, $p_{max} = 1/\mu$ can be calculated.

μ-analysis is performed on the nominal case, as well as on Cases 1 and 2 (with and without the α = 4 rad/s constraint) as discussed in Example 4, using MATLAB's *lftdata* command to generate **M** and **Δ**, and its *mussv* command to calculate μ. The resulting $p_{max} = 1/\mu$ are reported in Table 4.8. For the scenario without the α = 4 rad/s constraint, the maximum allowable uncertainty in the isolator locations, to maintain a stable system, is 22% for the nominal case and 26% for Cases 1 and 2. With the α = 4 rad/s constraint added, the maximum allowable uncertainty for Cases 1 and 2 reduces by 1%. It is interesting that even though the relative stability, measured by α, is higher for the nominal case and Cases 1 and 2 with the α = 4 rad/s constraint imposed, Cases 1 and 2 without the α = 4 rad/s constraint are more forgiving with regard to correct placement of the isolators. The implication is that better relative stability does not necessarily mean better robustness to uncertainties. Nonetheless, the >20% uncertainty margins obtained for all the cases investigated are generous enough for many practical applications.

Scenario	p_{max} **Values**		
	Nominal Case	**Case 1**	**Case 2**
Without α = 4 rad/s Constraint	0.22	0.26	0.26
With α = 4 rad/s Constraint	0.22	0.25	0.25

Table 4.8: $p_{max} = 1/\mu$ Values for Nominal Case, Cases 1 and 2, with and without the α = 4 rad/s Relative Stability Constraint Imposed

4.5. Conclusion

This chapter has presented a linear time invariant (LTI) control framework for optimally locating passive vibration isolators with known stiffness and damping properties, to minimize unwanted vibration caused by exogenous disturbance forces. The key challenge in realizing an LTI control formulation for non-discrete isolator placement is that the isolator locations are nonlinearly related to system states. This chapter shows that the nonlinear isolator placement problem can be transformed into an equivalent LTI feedback control problem by linking the control forces to measured outputs using a non-zero feedforward term. Accordingly, the isolator locations show up within a static output feedback gain matrix, and can thus be optimized, using methods from optimal control theory, to minimize the H_2 and/or H_∞ norms of transfer functions representing unwanted vibration. The proposed framework also allows well-established LTI control theories to be applied to the analyses of the optimal isolator placement problem and its

results. It thus provides an avenue for optimally exploiting mode coupling in complex isolator placement problems.

Several examples involving single- and multi-variable isolator placement problems in ultra-precision manufacturing (UPM) machines are used to demonstrate the benefits of the proposed framework with regard to isolation system optimization and analyses. Significant reductions in unwanted vibration are demonstrated and insights regarding the gravitational stability and robustness of various isolator placements are gained. The proposed framework provides a powerful engineering tool that can be used for optimizing and analyzing the locations of isolators for any passively-isolated UPM machine.

CHAPTER 5
CONCLUSIONS AND FUTURE WORK

5.1. Conclusions

This doctoral dissertation has used theoretical analysis combined with numerical and experimental tests to question the modal decoupling rule of thumb that is widely recommended for designing passive isolation systems of UPM machines. It has shown that, more often than not, mode coupling is superior to decoupling with regard to reducing UPM machine vibration. Moreover, it has proffered design guidelines and tools that can be used by machine designers to properly place passive vibration isolators such that benefits of mode coupling are fully exploited.

In Chapter 2 of this dissertation, eigenvalue analyses were performed on a single-variable, proportionally (or modally) damped, planar isolation system. It was shown that the drastic reduction of vibration caused by mode coupling is primarily linked to so-called "critical configurations" induced by two well-known and related phenomena, namely, curve veering and mode localization. This result is significant because it clears the misconception purported in academic literature and industrial practice that the vibration-reduction effects of mode coupling on UPM machines are simply linked to damping. In same chapter, perturbation analyses were performed on norms of frequency response functions representing UPM machine residual vibration. The results showed that, if properly implemented, mode coupling is almost always better than decoupling with regard to reducing residual vibration in UPM machines. Design guidelines were provided to help designers to properly exploit mode coupling. For instance, it was shown that the benefits of mode coupling could sometimes be realized by raising the CG of the machine above the plane containing the isolators, while other times it was better to place the CG of the machine below the plane of the isolators.

Chapter 3 extended the analyses of Chapter 2 by investigating the effects of non-proportional (NP) damping on mode coupling. It also studied the effects of mode coupling on transmissibility, and addition to residual vibration. Similar perturbation analyses as in Chapter 2 were carried out in Chapter 3. The results showed that, while the addition of NP damping could significantly alter the behavior of the isolated system compared to the modally damped case, mode coupling still provided ample opportunities to (simultaneously) reduce residual vibration and transmissibility, relative to decoupling. Design guidelines for properly locating isolators to exploit the benefits of weak mode coupling for single-variable, planar, non-proportionally damped isolation systems were proposed.

Chapter 4 focused squarely on the engineering objective of this dissertation by proposing a framework for reformulating the generalized (multivariable, 3-D) UPM isolator placement problem into a linear feedback controller whose gains represent isolator locations. The main challenge in creating the framework was shown to be the nonlinearity of the isolator placement problem. This problem was handled by defining a non-zero feed forward term in the state-space formulation of the equivalent feedback controller representing the generalized passive isolation system. The framework proposed in Chapter 4 is very powerful because it allows linear control theory, in all its richness and elegance, to be used for the optimization and analyses of passive isolator placement, including issues like stability and robustness.

The theoretical work presented in this dissertation has been backed up by simulations and experiments conducted on prototypes of UPM machines; the outcomes have been published in journal ([1-3]) and conference ([78,79,89,90]) articles. The results demonstrate that, when properly exploited, mode coupling could bring about huge (e.g., 50%) reductions in UPM machine vibration compared to modal decoupling. Note that, even though this dissertation is presented in the context of UPM machines, its methods and findings are applicable to the placement of passive isolators/suspensions/dampers in automotive, aerospace, civil, and other applications; they are therefore very far-reaching in scope.

5.2. Future Work

In the control theoretic framework of Chapter 4, gravitational stability was considered. However, as discussed in Chapter 1, it is common for commercial UPM machine isolation systems to reduce gravitational stability issues by adding an automatic re-leveling system to

passive (pneumatic) isolators. The problem is that automatic re-levelers are feedback control systems that could potentially cause dynamic instability in isolated systems [36]. It would be very beneficial to study the interactions between mode coupling, gravitational stability and the dynamic stability caused by automatic re-levelling systems, perhaps by incorporating their feedback controllers into the proposed control theoretic framework. A key challenge that may need to be addressed is the transport delays that are introduced into the re-levelling system's feedback loop due to air flow through narrow tubes [91].

In the context of UPM machines, it made sense in this dissertation to focus on studying the effects of isolator locations on mode coupling, while treating stiffness, damping, etc., as fixed parameters. There are several other applications, like automotive suspension and engine mount design where it may help to optimize isolator locations/orientations along with their stiffness and damping. This combined optimization problem is highly nonlinear. Several researchers have resorted to evolutionary algorithms [43,45,92] to carry out the nonlinear optimization; but they thus lose a lot of useful insights into the problem and its solutions. It would be very helpful if somehow this problem could be made to fit a linear control framework like the one proposed in this dissertation.

While passive isolation systems have been the focus of this dissertation, there is no reason to believe that mode coupling would not be of benefit to active isolation systems. It would be interesting to understand the interactions among sensor/actuator locations, isolator locations, control system gains, etc., in active isolation systems subject to mode coupling. Again, the control theoretic framework of Chapter 4 may be a good starting point for such an investigation. The challenge may be in keeping the control framework linear.

Mode coupling, in of itself, is an extremely interesting and powerful concept. Even though it has been studied for several decades in the context of curve veering and mode localization, this dissertation shows that there are still application areas (even old ones like passive vibration isolation) where it could be exploited. For example, it has been pointed out that mode coupling could be very beneficial to broadband energy harvesting [93,94]. Feedback control is another general application area that could benefit from mode coupling, for example, by intentionally tuning gains exploit mode coupling. It is the author's hope that this dissertation will spark ideas on how else to utilize mode coupling for advancing engineering.

APPENDIX

Control Framework for a Simple Single-Variable Optimization Problem

The control theoretic framework presented in Chapter 4 is simplified here for a single-variable isolator placement problem to help the reader to clearly see the quadratic relationship between isolator locations and system states, and how it is fit into an LTI feedback control formulation.

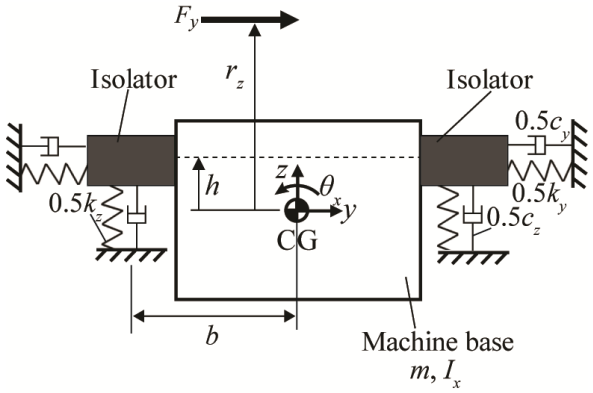

Figure A.1: Planar Model of Isolated Machine

Figure A.1 shows a single-variable isolator placement problem, similar to those studied in Chapters 2 and 3. The isolators lie in a single plane positioned at distance *h* from the CG. The equation of motion of the system can be written as

$$\mathbf{M}\ddot{\mathbf{q}} + \mathbf{C}\dot{\mathbf{q}} + \mathbf{K}\mathbf{q} = \mathbf{F}, \tag{A.1}$$

where

$$\begin{aligned} &\mathbf{q} = \begin{bmatrix} y & \theta_x \end{bmatrix}^{\mathrm{T}},\ \mathbf{F} = \begin{bmatrix} F_y & -r_z F_y \end{bmatrix}^{\mathrm{T}}, \\ &\mathbf{M} = \mathrm{diag}\left(\begin{bmatrix} m & I_x \end{bmatrix}\right), \\ &\mathbf{C} = \begin{bmatrix} c_y & -c_y h \\ -c_y h & c_{\theta x} + c_y h^2 \end{bmatrix},\ \mathbf{K} = \begin{bmatrix} k_y & -k_y h \\ -k_y h & k_{\theta x} + k_y h^2 \end{bmatrix}, \end{aligned} \tag{A.2}$$

where $k_{\theta x} = b^2 k_z$ and $c_{\theta x} = b^2 c_z$. Following Chapters 2 and 3, the dynamics in the z direction have been omitted because they are not affected by non-zero values of h.

As described in Section 4.2.2, Eq.(A.1) can be re-organized such that every term containing isolator locations is moved into a vector $\mathbf{F}_a$; i.e.,

$$\begin{bmatrix} m & 0 \\ 0 & I_x \end{bmatrix} \ddot{\mathbf{q}} + \begin{bmatrix} c_y & 0 \\ 0 & c_{\theta x} \end{bmatrix} \dot{\mathbf{q}} + \begin{bmatrix} k_y & 0 \\ 0 & k_{\theta x} \end{bmatrix} \mathbf{q} = \mathbf{F} + \mathbf{F}_a, \tag{A.3}$$

with $\mathbf{F}_a$ given by

$$\mathbf{F}_a = \begin{bmatrix} 0 & c_y h \\ c_y h & -c_y h^2 \end{bmatrix} \dot{\mathbf{q}} + \begin{bmatrix} 0 & k_y h \\ k_y h & -k_y h^2 \end{bmatrix} \mathbf{q}. \tag{A.4}$$

Factoring out h, $\mathbf{F}_a$ can be re-written as

$$\mathbf{F}_a = \begin{bmatrix} c_y & 0 \\ 0 & 1 \end{bmatrix} \underbrace{\begin{bmatrix} -h & 0 \\ 0 & -h \end{bmatrix}}_{\boldsymbol{\Gamma}_c} \mathbf{v}_c + \begin{bmatrix} k_y & 0 \\ 0 & 1 \end{bmatrix} \underbrace{\begin{bmatrix} -h & 0 \\ 0 & -h \end{bmatrix}}_{\boldsymbol{\Gamma}_k} \mathbf{v}_k, \tag{A.5}$$

based on measured outputs $\mathbf{v}_c$ and $\mathbf{v}_k$, defined as

$$\mathbf{v}_c = -\begin{bmatrix} 0 & 1 \\ c_y & 0 \end{bmatrix} \dot{\mathbf{q}} + \begin{bmatrix} 0 & 0 \\ c_y & 0 \end{bmatrix} \mathbf{u}_c, \; \mathbf{v}_k = -\begin{bmatrix} 0 & 1 \\ k_y & 0 \end{bmatrix} \mathbf{q} + \begin{bmatrix} 0 & 0 \\ k_y & 0 \end{bmatrix} \mathbf{u}_k. \tag{A.6}$$

The overall control input vector, measured output vector and control gain matrix for the isolators can be defined as

$$\mathbf{u} = \begin{Bmatrix} \mathbf{u}_k \\ \mathbf{u}_c \end{Bmatrix}, \; \mathbf{v} = \begin{Bmatrix} \mathbf{v}_k \\ \mathbf{v}_c \end{Bmatrix}, \; \boldsymbol{\Gamma} = \begin{bmatrix} \boldsymbol{\Gamma}_k & \mathbf{0} \\ \mathbf{0} & \boldsymbol{\Gamma}_c \end{bmatrix}. \tag{A.7}$$

The equation of motion of the single variable system given in Eq.(A.1) can now be re-written in state space form as

$$\dot{\mathbf{x}} = \mathbf{A}\mathbf{x} + \mathbf{B}_{\mathrm{w}}\mathbf{w} + \mathbf{B}_{\mathrm{u}}\mathbf{u}, \tag{A.8}$$

where

$$\mathbf{x} = \left\{\mathbf{q}^{\mathrm{T}} \quad \dot{\mathbf{q}}^{\mathrm{T}}\right\}^{\mathrm{T}}, \quad \mathbf{w} = F_y$$

$$\mathbf{A} = \begin{bmatrix} 0 & 0 & 1 & 0 \\ 0 & 0 & 0 & 1 \\ -\dfrac{k_y}{m} & 0 & -\dfrac{c_y}{m} & 0 \\ 0 & -\dfrac{k_{\theta x}}{I_x} & 0 & -\dfrac{c_{\theta x}}{I_x} \end{bmatrix}, \mathbf{B}_{\mathrm{w}} = \begin{bmatrix} 0 \\ 0 \\ \dfrac{1}{m} \\ -\dfrac{r_z}{I_x} \end{bmatrix}, \mathbf{B}_{\mathrm{u}} = \begin{bmatrix} 0 & 0 & 0 & 0 \\ 0 & 0 & 0 & 0 \\ -\dfrac{k_y}{m} & 0 & -\dfrac{c_y}{m} & 0 \\ 0 & -\dfrac{1}{I_x} & 0 & -\dfrac{1}{I_x} \end{bmatrix}. \tag{A.9}$$

The control input, **u**, can be expressed in feedback form as

$$\mathbf{u} = \mathrm{diag}\left(\left\{-h \quad -h \quad -h \quad -h\right\}\right)\mathbf{v}, \tag{A.10}$$

where **v** is the measured output vector of the isolated system which, according to Eq.(A.6), can be written as

$$\mathbf{v} = \mathbf{C}_{\mathrm{v}}\mathbf{x} + \mathbf{D}_{\mathrm{vw}}\mathbf{w} + \mathbf{D}_{\mathrm{vu}}\mathbf{u}, \tag{A.11}$$

with $\mathbf{C}_{\mathrm{v}}$, $\mathbf{D}_{\mathrm{vw}}$, and $\mathbf{D}_{\mathrm{vu}}$ given by

$$\mathbf{C}_{\mathrm{v}} = \begin{bmatrix} 0 & 1 & 0 & 0 \\ k_y & 0 & 0 & 0 \\ 0 & 0 & 0 & 1 \\ 0 & 0 & c_y & 0 \end{bmatrix}, \ \mathbf{D}_{\mathrm{vw}} = \mathbf{0}, \ \mathbf{D}_{\mathrm{vu}} = \begin{bmatrix} 0 & 0 & 0 & 0 \\ k_y & 0 & 0 & 0 \\ 0 & 0 & 0 & 0 \\ 0 & 0 & c_y & 0 \end{bmatrix}. \tag{A.12}$$

BIBLIOGRAPHY

[1] Okwudire CE, Lee J. Minimization of the residual vibrations of ultra-precision manufacturing machines via optimal placement of vibration isolators. Precision Engineering. 2013 Apr 30;37(2):425-32.

[2] Lee J, Okwudire CE. Reduction of vibrations of passively-isolated ultra-precision manufacturing machines using mode coupling. Precision Engineering. 2016 Jan 31;43:164-77.

[3] Lee J, Ghasemi AH, Okwudire CE, Scruggs JT. A linear feedback control framework for optimally locating passive vibration isolators with known stiffness and damping parameters. Journal of Vibration and Acoustics. 2016 – Under Review

[4] Hrovat D. Applications of optimal control to advanced automotive suspension design. Journal of Dynamic Systems, Measurement, and Control. 1993 Jun 1;115(2B):328-42.

[5] Yu Y, Naganathan NG, Dukkipati RV. A literature review of automotive vehicle engine mounting systems. Mechanism and Machine Theory. 2001 Jan 1;36(1):123-42.

[6] Verros G, Natsiavas S, Papadimitriou C. Design optimization of quarter-car models with passive and semi-active suspensions under random road excitation. Journal of Vibration and Control. 2005 May 1;11(5):581-606.

[7] Swanson DA, Wu HT, Ashrafiuon H. Optimization of aircraft engine suspension systems. Journal of Aircraft. 1993 Nov;30(6):979-84.

[8] Ahn YK, Song JD, Yang BS. Optimal design of engine mount using an artificial life algorithm. Journal of Sound and Vibration. 2003 Mar 20;261(2):309-28.

[9] Preumont A, Horodinca MI, Romanescu I, De Marneffe B, Avraam M, Deraemaeker A, Bossens F, Hanieh AA. A six-axis single-stage active vibration isolator based on Stewart platform. Journal of Sound and Vibration. 2007 Mar 6;300(3):644-61.

[10] Kelly JM. Aseismic base isolation: review and bibliography. Soil Dynamics and Earthquake Engineering. 1986 Oct 31;5(4):202-16.

[11] Buckle IG, Mayes RL. Seismic isolation: history, application, and performance-a world view. Earthquake Spectra. 1990 May;6(2):161-201.

[12] Lee-Glauser GJ, Ahmadi G, Horta LG. Integrated passive/active vibration absorber for multistory buildings. Journal of Structural Engineering. 1997 Apr;123(4):499-504.

[13] DeBra DB. Vibration isolation of precision machine tools and instruments. CIRP Annals-Manufacturing Technology. 1992 Dec 31;41(2):711-8.

[14] Rivin EI. Vibration isolation of precision equipment. Precision Engineering. 1995 Jan 31;17(1):41-56.

[15] Schellekens P, Rosielle N, Vermeulen H, Vermeulen MM, Wetzels SF, Pril W. Design for precision: current status and trends. CIRP Annals-Manufacturing Technology. 1998 Dec 31;47(2):557-86.

[16] Alting L, Kimura F, Hansen HN, Bissacco G. Micro engineering. CIRP Annals-Manufacturing Technology. 2003 Dec 31;52(2):635-57.

[17] Masuzawa T. State of the art of micromachining. CIRP Annals-Manufacturing Technology. 2000 Dec 31;49(2):473-88.

[18] Rajurkar KP, Levy G, Malshe A, Sundaram MM, McGeough J, Hu X, Resnick R, DeSilva A. Micro and nano machining by electro-physical and chemical processes. CIRP Annals-Manufacturing Technology. 2006 Dec 31;55(2):643-66.

[19] Williams RE, Huang Y, Melkote S, Kinsey B, Sun W, Yao D. Recent advances in micro/meso-scale manufacturing processes. In ASME 2005 International Mechanical Engineering Congress and Exposition 2005 Jan 1 (pp. 863-884). American Society of Mechanical Engineers.

[20] Hansen HN, Carneiro K, Haitjema H, De Chiffre L. Dimensional micro and nano metrology. CIRP Annals-Manufacturing Technology. 2006 Dec 31;55(2):721-43.

[21] Corbett J, McKeown PA, Peggs GN, Whatmore R. Nanotechnology: international developments and emerging products. CIRP Annals-Manufacturing Technology. 2000 Dec 31;49(2):523-45.

[22] Chyan HC, Ehmann KF. Development of curved helical micro-drill point technology for micro-hole drilling. Mechatronics. 1998 Jun 30;8(4):337-58.

[23] Lu Z, Yoneyama T. Micro cutting in the micro lathe turning system. International Journal of Machine Tools and Manufacture. 1999 Jul 31;39(7):1171-83.

[24] Zhang B, Liu X, Brown CA, Bergstrom TS. Microgrinding of nanostructured material coatings. CIRP Annals-Manufacturing Technology. 2002 Dec 31;51(1):251-4.

[25] Bang YB, Lee KM, Oh S. 5-axis micro milling machine for machining micro parts. The International Journal of Advanced Manufacturing Technology. 2005 May 1;25(9-10):888-94.

[26] Subrahmanyan PK, Trumper DL. Synthesis of passive vibration isolation mounts for machine tools a control systems paradigm. In American Control Conference, 2000. Proceedings of the 2000 2000 (Vol. 4, pp. 2886-2891). IEEE.

[27] Vermeulen MM, Rosielle PC, Schellekens PH. Design of a high-precision 3D-coordinate measuring machine. CIRP Annals-Manufacturing Technology. 1998 Dec 31;47(1):447-50.

[28] Ehmann KF. A synopsis of US micro-manufacturing research and development activities and trends. Borovets, Bulgaria. 2007:7-13.

[29] Rivin EI. Vibration isolation of precision objects. Sound and Vibration. 2006 Jul 1;40(7):12-20.

[30] Kim CJ, Oh JS, Park CH. Modelling vibration transmission in the mechanical and control system of a precision machine. CIRP Annals-Manufacturing Technology. 2014 Dec 31;63(1):349-52.

[31] Technical Manufacturing Corporation. Precision vibration isolation systems: Technical background. http://www.techmfg.com/techbkgd/intro.htm. Accessed on 01/12/2015

[32] Singhose WE, Searing WP, Singer NC. Improving repeatability of coordinate measuring machines with shaped command signals. Precision Engineering. 1996 May 31;18(2):138-46.

[33] Jones SD, Ulsoy AG. An approach to control input shaping with application to coordinate measuring machines. Journal of Dynamic systems, Measurement, and Control. 1999 Jun 1;121(2):242-7.

[34] Karnopp D. Active and semi-active vibration isolation. Journal of Vibration and Acoustics. 1995 Jun 1;117(B):177-85.

[35] Liu Y, Waters TP, Brennan MJ. A comparison of semi-active damping control strategies for vibration isolation of harmonic disturbances. Journal of Sound and Vibration. 2005 Feb 7;280(1):21-39.

[36] Ryaboy VM. Static and dynamic stability of pneumatic vibration isolators and systems of isolators. Journal of Sound and Vibration. 2014 Jan 6;333(1):31-51.

[37] Okwudire C. A study on the effects of isolator, motor and work surface heights on the vibrations of ultra-precision machine tools. Proc ICOMM, Evanston, Illinois, March. 2012 Mar 12:31-6.

[38] Shin YH, Kim KJ, Chang PH, Han DK. Three degrees of freedom active control of pneumatic vibration isolation table by pneumatic and time delay control technique. Journal of Vibration and Acoustics. 2010 Oct 1;132(5):051013.

[39] Kato T, Kawashima K, Sawamoto K, Kagawa T. Active control of a pneumatic isolation table using model following control and a pressure differentiator. Precision Engineering. 2007 Jul 31;31(3):269-75.

[40] Erin C, Wilson B, Zapfe J. An improved model of a pneumatic vibration isolator: theory and experiment. Journal of Sound and Vibration. 1998 Nov 19;218(1):81-101.

[41] Franchek MA, Ryan MW, Bernhard RJ. Adaptive passive vibration control. Journal of Sound and Vibration. 1996 Feb 8;189(5):565-85.

[42] Leo DJ, Inman DJ. A quadratic programming approach to the design of active–passive vibration isolation systems. Journal of Sound and Vibration. 1999 Mar 11;220(5):807-25.

[43] Li TH, Kuo YP. Evolutionary algorithms for passive suspension systems. JSME International Journal Series C Mechanical Systems, Machine Elements and Manufacturing. 2000;43(3):537-44.

[44] Singh MP, Moreschi LM. Optimal placement of dampers for passive response control. Earthquake Engineering & Structural Dynamics. 2002 Apr 1;31(4):955-76.

[45] Ahn YK, Kim YC, Yang BS, Ahmadian M, Ahn KK, Morishita S. Optimal design of an engine mount using an enhanced genetic algorithm with simplex method. Vehicle System Dynamics. 2005 Jan 1;43(1):57-81.

[46] Lin Y, Zhang Y. Suspension optimization by a frequency domain equivalent optimal control algorithm. Journal of Sound and Vibration. 1989 Sep 8;133(2):239-49.

[47] Lin Y, Luo W, Zhang YM. A new method for the optimization of a vibration isolation system. Journal of Vibration and Acoustics. 1990 Jul 1;112(3):413-6.

[48] Gluck N, Reinhorn AM, Gluck J, Levy R. Design of supplemental dampers for control of structures. Journal of Structural Engineering. 1996 Dec;122(12):1394-9.

[49] Yang JN, Lin S, Kim JH, Agrawal AK. Optimal design of passive energy dissipation systems based on H_∞ and H_2 performances. Earthquake Engineering & Structural Dynamics. 2002 Apr 1;31(4):921-36.

[50] Lopez Garcia D, Soong TT. Efficiency of a simple approach to damper allocation in MDOF structures. Journal of Structural Control. 2002 Apr 1;9(1):19-30.

[51] Zuo L, Nayfeh SA. Structured H_2 optimization of vehicle suspensions based on multi-wheel models. Vehicle System Dynamics. 2003 Nov 1;40(5):351-71.

[52] Bağdatlı SM, Okwudire CE, Ulsoy AG. Linear quadratic design of passive vibration isolators. In ASME 2014 Dynamic Systems and Control Conference 2014 Oct 22 (pp. V003T50A003-V003T50A003). American Society of Mechanical Engineers.

[53] Zuo L, Nayfeh SA. The two-degree-of-freedom tuned-mass damper for suppression of single-mode vibration under random and harmonic excitation. Journal of Vibration and Acoustics. 2006 Feb 1;128(1):56-65.

[54] Braun SG, Ewins DJ, Rao SS. Encyclopedia of vibration. Elsevier. 2002:1490-1491.

[55] Piersol A, Paez T. Harris' shock and vibration handbook 6th edition. McGraw-Hill. 2010: 39.13-39.14.

[56] Racca R. How to select power-train isolators for good performance and long service life. SAE Technical Paper; 1982 Feb 1.

[57] Andrews F. Items which can compromise vibration isolation. http://adopt.arcetri.astro.it/html/sec-LBT/datasheets/vibration_isolators/Fabreeka/practical_considerations.pdf. Accessed on 01/12/2015

[58] DeBra DB, Warner RE. Pneumatic isolation systems with linear passive damping. Lawrence Livermore National Lab., CA (USA); 1982 Jan 19.

[59] Lee JH, Kim KJ. A method of transmissibility design for dual-chamber pneumatic vibration isolator. Journal of Sound and Vibration. 2009 Jun 5;323(1):67-92.

[60] Ewins DJ. Modal Testing: Theory, Practice, and Application. Research Studies Press, 2000: 62-63.

[61] Pierre C. Mode localization and eigenvalue loci veering phenomena in disordered structures. Journal of Sound and Vibration. 1988 Nov 8;126(3):485-502.

[62] Du Bois JL, Adhikari S, Lieven NA. On the quantification of eigenvalue curve veering: a veering index. Journal of Applied Mechanics. 2011 Jul 1;78(4):041007.

[63] Igusa T. Critical configurations of systems subjected to wide-band input. Journal of Sound and Vibration. 1993 Dec 22;168(3):525-41.

[64] Perkins NC, Mote CD. Comments on curve veering in eigenvalue problems. Journal of Sound and Vibration. 1986 May 8;106(3):451-63.

[65] Leissa AW. On a curve veering aberration. Zeitschrift für angewandte Mathematik und Physik ZAMP. 1974 Jan 1;25(1):99-111.

[66] Anderson PW. Absence of diffusion in certain random lattices. Physical Review. 1958 Mar 1;109(5):1492.

[67] Thiruvenkatanathan P, Woodhouse J, Yan J, Seshia AA. Manipulating vibration energy confinement in electrically coupled microelectromechanical resonator arrays. Microelectromechanical Systems, Journal of. 2011 Feb;20(1):157-64.

[68] Pierre C, Dowell EH. Localization of vibrations by structural irregularity. Journal of Sound and Vibration. 1987 May 8;114(3):549-64.

[69] Wang YZ, Cheng SH. The optimal design of dynamic absorber in the time domain and the frequency domain. Applied Acoustics. 1989 Dec 31;28(1):67-78.

[70] Asami T, Nishihara O, Baz AM. Analytical solutions to H_∞ and H_2 optimization of dynamic vibration absorbers attached to damped linear systems. Journal of Vibration and Acoustics. 2002 Apr 1;124(2):284-95.

[71] Bartel DL, Krauter AI. Time domain optimization of a vibration absorber. Journal of Engineering for Industry. 1971 Aug 1;93(3):799-803.

[72] Kim CJ, Padden T, Kim J. Ultra-precision machine tool. US patent # 7,845,257 B2 2010.

[73] Hodges CH. Confinement of vibration by structural irregularity. Journal of Sound and Vibration. 1982 Jun 8;82(3):411-24.

[74] Pierre C. Weak and strong vibration localization in disordered structures: a statistical investigation. Journal of Sound and Vibration. 1990 May 22;139(1):111-32.

[75] Rajagopal G. Optimal mode localization in disordered, periodic structures (Doctoral dissertation, Massachusetts Institute of Technology and Woods Hole Oceanographic Institution).

[76] Balmes E. High modal density, curve veering, localization: a different perspective on the structural response. Journal of Sound and Vibration. 1993 Feb 22;161(2):358-63.

[77] Vijayan K, Woodhouse J. Shock amplification, curve veering and the role of damping. Journal of Sound and Vibration. 2014 Feb 28;333(5):1379-89.

[78] Lee J, Okwudire CE. Optimal damping for the reduction of residual vibrations in ultra-precision manufacturing machines. In ASPE 2013 annual meeting 2013.

[79] Lee J, Okwudire C. Effects of non-proportional damping on the residual vibrations of mode-coupled ultra-precision manufacturing machines. In ASME 2014 Dynamic Systems and Control Conference 2014 Oct 22 (pp. V003T50A001-V003T50A001). American Society of Mechanical Engineers.

[80] Kozak K, Singhose W, Ebert-Uphoff I. Performance measures for input shaping and command generation. Journal of Dynamic Systems, Measurement, and Control. 2006 Sep 1;128(3):731-6.

[81] Pierre C, Cha PD. Strong mode localization in nearly periodic disordered structures. AIAA Journal. 1989 Feb;27(2):227-41.

[82] Morris K, Yang S. Comparison of actuator placement criteria for control of structures. Journal of Sound and Vibration. 2015 Sep 29;353:1-8.

[83] Scruggs JT. Multi-objective optimization of regenerative damping systems in vibrating structures. In American Control Conference, 2007. ACC'07 2007 Jul 9 (pp. 2672-2677). IEEE.

[84] Warner EC, Scruggs JT. Control of vibratory networks with passive and regenerative systems. In American Control Conference (ACC), 2015 2015 Jul 1 (pp. 5502-5508). IEEE.

[85] Warner EC, Scruggs JT. Regeneratively-constrained LQG control of vibration networks with polytopic model uncertainty. In Control Applications (CCA), 2015 IEEE Conference on 2015 Sep 21 (pp. 1498-1504). IEEE.

[86] Skogestad S, Postlethwaite I. Multivariable feedback control: analysis and design. New York: Wiley; 2007 Feb.

[87] Dullerud GE, Paganini F. A course in robust control theory: a convex approach. Springer Science & Business Media; 2013 Mar 14.

[88] Chen X, Kareem A. Curve veering of eigenvalue loci of bridges with aeroelastic effects. Journal of engineering mechanics. 2003 Feb;129(2):146-59.

[89] Ghasemi AH, Lee J, Okwudire CE. A control theoretic framework for optimally locating passive vibration isolators to minimize residual vibration. In ASME 2015 Dynamic Systems and Control Conference 2015 Oct 28 (pp. V003T53A003-V003T53A003). American Society of Mechanical Engineers.

[90] Okwudire CE, Lee J. Optimal motor location for the reduction of residual vibrations in mode-coupled ultra-precision manufacturing machines. In ASME 2013 International Manufacturing Science and Engineering Conference collocated with the 41st North American Manufacturing Research Conference 2013 Jun 10 (pp. V002T02A018-V002T02A018). American Society of Mechanical Engineers.

[91] Newport. Instability & Oscillation of High CG Table Systems. http://www.newport.com/Seminar-Notes-Instability-Oscillation-of-High-CG-/154651/1033/content.aspx. Accessed on 03/07/2017

[92] Akanda A, Adulla C. Application of evolutionary computation in automotive powertrain mount tuning. Shock and Vibration. 2006;13(2):85-102.

[93] Vijayan K, Friswell MI, Khodaparast HH, Adhikari S. Non-linear energy harvesting from coupled impacting beams. International Journal of Mechanical Sciences. 2015 Jun 30;96:101-9.

[94] Petropoulos T, Yeatman EM, Mitcheson PD. MEMS coupled resonators for power generation and sensing. Proc. Micromech. Europe, Leuven, Belgium. 2004 Sep:5-7.